

# **Electrochemical Unit Operations in Industrial Wastewater Treatment: The Development of Electrocoagulation and Photo Electrochemical Oxidation Reactors Based on Novel Nanocomposite Electrode**

Report to the  
**Water Research Commission**

by

**L.D. Makgae, E.H. Umukoro, M.G. Peleyeju, N. Mabuba,  
O.S. Oluwafemi & O.A. Arotiba**

Department of Applied Chemistry, University of Johannesburg, South Africa

**WRC Report No. 2567/1/19**

**ISBN 978-0-6392-0099-6**

**January 2020**



**Obtainable from**

Water Research Commission

Private Bag X03

Gezina, 0031

[orders@wrc.org.za](mailto:orders@wrc.org.za) or download from [www.wrc.org.za](http://www.wrc.org.za)

**DISCLAIMER**

This report has been reviewed by the Water Research Commission (WRC) and approved for publication. Approval does not signify that the contents necessarily reflect the views and policies of the WRC, nor does mention of trade names or commercial products constitute endorsement or recommendation for use.

## EXECUTIVE SUMMARY

---

Wastewater treatment by conventional methods is becoming inefficient owing to the increase in the quantity and complexity of the pollutants present in wastewater (especially industrial wastewater). The presence of pollutants has been reported in treated waters owing to their recalcitrant nature. The burden of pollution by surface water and water bodies used as feed water stock in wastewater treatment plants are on the increase owing to the discharge of untreated industrial effluents. Thus, there is need to seek alternative and/or complementary methods that will effectively remove recalcitrant pollutants from wastewater. These methods should be environmentally benign, relatively low cost with the capacity to harness solar energy (sustainability) either directly on the electrode (the reactor) or as a source of generating potential or white light. These envisaged methods will add to the water treatment mix of South Africa which is still about 80% conventional treatment approach based.

This project explored the possibilities of applying electrochemical technologies to industrial wastewater treatment. Photoelectrochemical oxidation (or photoelectrocatalysis) is a subset of advanced oxidation processes (AOP). Photoelectrochemical oxidation or photoelectrocatalytic oxidation (PEC), just like the more known photocatalysis, involves the use of *in situ* generated hydroxyl radical for the breaking down of complex organic molecules to non-toxic molecules with water and carbon dioxide envisaged as final products. It, however, has the added advantage (over photocatalysis) of improved efficiency owing to the reduction in the rate of recombination of electron-hole pairs on the semiconductor surface. Electrocoagulation (EC), on the other hand, is an electrochemical technology that generates coagulating ions *in situ* from a sacrificial anode. This technique has been shown to be cheaper and more environmentally friendly than the conventional chemical coagulation.

Literature survey on photoelectrochemical and electrocoagulation technologies for wastewater treatment were carried out. The survey showed the global need and relevance of this research to our water-stressed world, especially South Africa. Currently, research in electrochemical technologies for water treatment is at its infancy in South Africa (SA) with our research team arguably leading the way. The advantages of PEC and EC which include low cost, reduced environmental burden, improved efficiency towards the removal of recalcitrant pollutants and so on can be harnessed and introduced into South African wastewater treatment mix. Furthermore, the understanding of the individual PEC and EC systems can lead to the design of hybrid reactors which can be used on industrials sites and this will markedly reduce the pollution load discharged into SA's stressed water bodies.

In the PEC studies, different types of materials such as exfoliated graphite (EG), reduced graphene oxide, carbon nanoparticle, titanium dioxide (TiO<sub>2</sub>), zinc oxide (ZnO), tungsten trioxide (WO<sub>3</sub>), bismuth vanadate (BiVO<sub>4</sub>), molybdenum disulphide (MoS<sub>2</sub>), etc. were prepared and applied. EG was prepared by the exfoliation of intercalated natural graphite using temperature shock. The semiconductors were prepared primarily by hydrothermal techniques. The photoanodes were fabricated by compositing the carbon support with the semiconductors. Dopants such as silver and palladium were added in some cases to improve the photoactivity of the anode. The different composites were compresses at high pressure into

sheets which were fabricated into electrodes by using a conducting copper wire. The materials before after fabrication into anodes were characterised by different techniques such as electron microscopy, Raman spectroscopy, UV/VIS spectroscopy, X-ray diffractometry, thermogravimetry, voltammetry, impedimetry, chronoamperometry, etc. Photoelectrochemical degradation experiments were conducted in the presence of a solar simulator, which mimics radiation from sunlight. The photoanodes were used in the treatment of water containing dyes and pharmaceuticals organic molecules in water. Techniques such as visible spectroscopy, chemical oxygen demand, total organic carbon, and chromatography were used to determine the extent of pollutant removal or degradation/treatment.

It has been shown that photoanodes based on exfoliated graphite support can be used for PEC for the first time. The enhanced performances of the various photoanode in combination with selected semiconductors have been demonstrated. This work further showed that the alignment of semiconductors as heterojunctions can have better photoelectrocatalytic responses and thus improved the rate of pollutant degradation. The kinetics of degradation were studied and attempts to qualitatively analyse degradation products were made. This work has produced novel semiconductor photoanodes which can be used for the solar-photoelectrochemical treatment of industrial wastewater.

Electrocoagulation (EC) studies involved the use materials such as iron, aluminium and other metals as sacrificial anodes in order to generate coagulants *in situ* for the removal of colloids in polluted water. In the EC studies, a comparison between chemical coagulation (CC) and EC was carried out. The performances of aluminium and iron as electrodes were compared for the removal of metal and dye. Furthermore, two different types of steels and a hybrid electrode was used for EC experiments.

Electrocoagulation studies showed the better performance of EC over chemical coagulation (CC) using conventional Al and Fe anodes for the treatment of a dye and Pb ion. Furthermore, the work revealed that the performance of EC depends on the nature of the anode. It was shown that two different types of stainless steel gave different EC performance profiles. This is an interesting result for optimisation of an EC process.

The overarching concept of this research is the design of a flow-through reactor that will be used for the pre-treatment of industrial wastewater. In this regard, we have acquired preliminary data for the design of a prototype reactor for the fabrication of a hybrid process of PEC and EC. Research on this prototype and its optimisation is ongoing.



## ACKNOWLEDGEMENTS

---

Firstly, the project team would like to acknowledge the **Water Research Commission** as an institution for the kind funding.

Sincere thanks to the WRC manager, Dr John Zvimba, for his patience, guidance and understanding throughout this project.

Gratitude to Mr Bennie Mokgonyana for bearing the WRC administrative burden.

Many thanks to our industrial collaborator Mr Philip Nel of Radical Waters. We still have a lot to do in the future.

This work will not have gone this far if not for the hardworking students (PhD, MSc, BTech and in-service trainees) who gave their commitment and intellectual energy.

Of course, to the academic team, Dr N Mabuba, Prof SO Oluwafemi, Dr D Nkosi, we say thank you.

Our gratitude goes to the Centre for Nanomaterials Science Research, University of Johannesburg (UJ), the Department of Applied Chemistry (now Chemical Sciences) UJ and the Faculty of Science UJ for their support.

We thank the following Reference Group members for their invaluable contributions/suggestions/comments – your comments truly added value to this work.

| Reference Group | Affiliation                             |
|-----------------|---|
| Dr JN Zvimba    | Water Research Commission               |
| Dr G Gericke    | ESKOM                                   |
| Dr S Malinga    | University of Johannesburg              |
| Dr J Nathoo     | ESKOM                                   |
| Prof RF Ajayi   | University of the Western Cape          |
| Prof M Matoetoe | Cape Peninsula University of Technology |

This page was intentionally left blank

## CONTENTS

---

|  |           |
|--|-----------|
| <b>CONTENTS</b>  | <b>v</b>  |
| <b>CHAPTER 1: BACKGROUND</b>   | <b>1</b>  |
| 1.1 INTRODUCTION   | 1         |
| 1.2 PROJECT AIMS   | 2         |
| <b>CHAPTER 2: LITERATURE REVIEW: ELECTROCOAGULATION AND ELECTROCHEMICAL ADVANCED OXIDATION PROCESSES IN WATER TREATMENT</b>          | <b>4</b>  |
| 2.1 INTRODUCTION   | 4         |
| 2.2 CHALLENGES WITH CONVENTIONAL TREATMENT METHODS   | 5         |
| 2.3 ELECTROCOAGULATION   | 5         |
| 2.3.1 Coagulation and Electrocoagulation   | 5         |
| 2.3.2 Electrocoagulation   | 6         |
| 2.3.3 Anodic and cathodic materials in EC  | 6         |
| 2.4 ELECTROCHEMICAL ADVANCED OXIDATION PROCESSES (EAOPS)   | 7         |
| 2.5 COMBINATION OF EC AND EAOP   | 8         |
| <b>CHAPTER 3: SYNTHESIS, CHARACTERISATION AND PHOTOELECTROCHEMICAL DEGRADATION STUDIES OF CARBON BASED SEMICONDUCTOR PHOTOANODES</b> | <b>10</b> |
| 3.1 INTRODUCTION   | 10        |
| 3.2 METHODOLOGY  | 12        |
| 3.2.1 Materials and Instrumentation  | 12        |
| 3.2.2 Preparation of exfoliated graphite   | 12        |
| 3.2.3 Preparation of reduced graphene oxide (rGO)  | 13        |
| 3.2.4 Preparation of EG-ZnO nanocomposite  | 13        |
| 3.2.5 Preparation of Ag-ZnO nanoparticles  | 13        |
| 3.2.6 Preparation of Ag-ZnO-rGO composite photoanode   | 13        |
| 3.2.7 Preparation of WO <sub>3</sub> nanoparticles   | 14        |
| 3.2.8 Preparation of WO <sub>3</sub> -EG composite   | 14        |
| 3.2.9 Fabrication of WO <sub>3</sub> -EG composite electrode   | 14        |
| 3.2.10 Electrochemical and photoelectrochemical experiments  | 15        |
| 3.3 RESULT AND DISCUSSION  | 15        |
| 3.3.1 Spectroscopic characterisation for EG-ZnO  | 15        |
| 3.3.2 Spectroscopic characterisation for Ag-ZnO-rGO  | 16        |
| 3.3.3 Electron Microscopy characterisation for Ag-ZnO-rGO  | 18        |
| 3.3.4 Pore size and surface area analyses  | 20        |
| 3.3.5 Spectroscopic Characterisation of EG-WO <sub>3</sub>   | 20        |
| 3.3.6 Morphological studies of EG, WO <sub>3</sub> and WO <sub>3</sub> -EG   | 22        |
| 3.3.7 Electrochemical and photoelectrochemical characterisation of rGO and Ag-ZnO-rGO  | 23        |
| 3.3.8 Electrochemical and photoelectrochemical studies of EG and WO <sub>3</sub> -EG   | 24        |
| 3.3.9 Electrochemical and Photoelectrochemical degradation of organic pollutants   | 25        |
| <b>CHAPTER 4: ELECTROCOAGULATION FOR THE TREATMENT OF ORANGE II DYE COMBINED WITH HEAVY METALS IN WASTEWATER</b>                     | <b>50</b> |
| 4.1 INTRODUCTION   | 50        |
| 4.2 METHODOLOGY ON CC VS EC  | 52        |
| 4.2.1 Materials, analytical measurements and experimental equipment  | 52        |

|       |  |    |
|-------|--|----|
| 4.2.2 | Preparation of the synthetic effluent .....  | 54 |
| 4.2.3 | Chemical coagulation optimization .....  | 55 |
| 4.3   | RESULT AND DISCUSSION.....   | 55 |
| 4.3.1 | Simulated wastewater characterisation .....  | 55 |
| 4.3.2 | Chemical coagulation using alum as a coagulant .....   | 56 |
| 4.3.3 | Electrocoagulation experiments.....  | 59 |
| 4.4   | THE APPLICATION OF SS 316L AND SS 304 ELECTRODES IN ELECTROCOAGULATION FOR THE TREATMENT OF SIMULATED WASTEWATER: A COMPARATIVE STUDY..... | 60 |
| 4.5   | METHODOLOGY: COMPARATIVE STUDY .....   | 60 |
| 4.5.1 | Materials.....   | 60 |
| 4.5.2 | Analytical measurements.....   | 60 |
| 4.5.3 | Experimental .....   | 61 |
| 4.6   | RESULTS AND DISCUSSION .....   | 62 |
| 4.6.1 | Effect of initial conductivity on pollutant removal and corresponding operational costs.....   | 62 |
| 4.6.2 | Effect of current density on pollutant removal.....  | 64 |
| 4.6.3 | Electrocoagulation time studies ( $t_{EC}$ ) .....   | 67 |
| 4.6.4 | Sub Conclusion .....   | 68 |

**CHAPTER 5: PHOTOELECTROCHEMICAL SYSTEMS ON TITANIUM SHEET BASED PHOTOANODES FOR THE DEGRADATION OF DYE IN WASTEWATER.....70**

|       |   |    |
|-------|---|----|
| 5.1   | MOTIVATION.....   | 70 |
| 5.2   | INTRODUCTION .....  | 70 |
| 5.3   | METHODOLOGY .....   | 72 |
| 5.3.1 | Materials and Equipment .....   | 72 |
| 5.3.2 | Electrochemical Reactor design and measurements: .....                  | 72 |
| 5.3.3 | Synthesis of $WO_3$ nanorods.....                                       | 73 |
| 5.3.4 | Preparation of carbon nanoparticles, $BiVO_4$ and CNP/B- $BiVO_4$ ..... | 73 |
| 5.3.5 | Fabrication of the photoanode .....                                     | 74 |
| 5.4   | RESULT AND DISCUSSION.....  | 74 |
| 5.4.1 | Morphology investigation, EDS analysis and elemental mapping .....      | 74 |
| 5.4.2 | Diffuse reflectance spectroscopy .....                                  | 76 |
| 5.4.3 | Linear sweep voltammetry and photo-current response .....               | 77 |
| 5.4.4 | Photoelectrocatalytic degradation experiments .....                     | 78 |

**CHAPTER 6: FLOW-THROUGH REACTOR DESIGN.....80**

|       |                                       |    |
|-------|---------------------------------------|----|
| 6.1   | INTRODUCTION .....                    | 80 |
| 6.1.1 | About Radical Waters .....            | 80 |
| 6.1.2 | The flow-through reactor design ..... | 80 |

**CHAPTER 7: CONCLUSIONS & RECOMMENDATIONS .....82**

|       |   |    |
|-------|---|----|
| 7.1   | CONCLUSIONS.....  | 82 |
| 7.1.1 | Photoelectrochemical catalytic degradation .....  | 82 |
| 7.1.2 | Electrocoagulation .....  | 83 |
| 7.2   | RECOMMENDATIONS .....   | 84 |
| 7.2.1 | Photoelectrochemical catalytic degradation .....  | 84 |
| 7.2.2 | Electrocoagulation .....  | 84 |
| 7.2.3 | Combination of Photoelectrochemical catalytic degradation (PEC) with Electrocoagulation (EC)..... | 84 |

## LIST OF FIGURES

|  |    |
|--|----|
| Figure 3.1. XRD patterns of (a) EG, (b) ZnO, and (c) EG-ZnO. (d) TGA thermograms of EG, ZnO and EG-SiO <sub>x</sub> -ZnO nanocomposites .....  | 16 |
| Figure 3.2. (a) Raman spectra of the prepared (i) GO and (ii) rGO; (b) XRD patterns of (i) GO, (ii) ZnO, (iii) ZnO-rGO, (iv) Ag-ZnO and (v) Ag-ZnO-rGO; (c) UV-vis diffuse reflectance spectra of (i) ZnO, (ii) Ag-ZnO, and (iii) Ag-ZnO-rGO; (d) FTIR spectra of (i) rGO and (ii) Ag-ZnO-rGO .....  | 18 |
| Figure 3.3. SEM images of (a) exfoliated graphite; (b) ZnO nanoparticles; (c) reduced graphene oxide (rGO); (d) the as-synthesised Ag-ZnO-rGO material. (e) EDX spectrum of the as-prepared composite. TEM images of the as-synthesised (f) rGO; (g) ZnO-rGO and (h) Ag-ZnO-rGO material. ....   | 19 |
| Figure 3.4. (a) Raman result of WO <sub>3</sub> -EG and EG (inset); (b) X-ray diffraction patterns of EG, (I) WO <sub>3</sub> , (II) WO <sub>3</sub> -EG and (III) EG; (c) FTIR results of (I) EG and (II) WO <sub>3</sub> -EG composite; and (d) UV-Visible diffuse reflectance spectra of (I) EG and (II) WO <sub>3</sub> -EG .....  | 22 |
| Figure 3.5. (a) WO <sub>3</sub> , (b) EG and (c) WO <sub>3</sub> -EG composite images of SEM. (d) EDS spectrum of WO <sub>3</sub> -EG composite .....  | 23 |
| Figure 3.6. Cyclic voltammograms of (a)(i) rGO and (ii) Ag-ZnO-rGO electrodes in 5mM [Fe(CN) <sub>6</sub> ] <sup>3-/4-</sup> in 0.1 M KCl at 50 mVs <sup>-1</sup> ; (b) Photoelectrochemical response of Ag-ZnO-rGO electrode in 0.1 M Na <sub>2</sub> SO <sub>4</sub> in the dark (off) and under illumination (on) at 0.3 V. ....  | 24 |
| Figure 3.7. (a) CVs of (I) EG and (II) WO <sub>3</sub> -EG composite electrodes using 5mM [Fe(CN) <sub>6</sub> ] <sup>3-/4-</sup> in 0.1 M KCl solution at a scan rate of 20 mVs <sup>-1</sup> ; (b) CVs of WO <sub>3</sub> -EG composite electrodes at different scan rate and the plot of peak currents vs square root of scan rates. (c) Linear sweep voltammograms of EG and WO <sub>3</sub> -EG composite electrodes with (light) and without (dark) xenon lamp; and (d) responses from photocurrent of EG ((I) black) and WO <sub>3</sub> -EG ((II) red) composite electrodes in the dark (off) and under irradiation (on) ..... | 25 |
| Figure 3.8. (a) UV-Vis spectra for the degradation of orange II dye at Ag-ZnO-rGO electrode using photoelectrochemical oxidation; Normalised decay plots of the photoelectrochemical degradation of orange II dye (b) at rGO, ZnO-rGO and Ag-ZnO-rGO electrodes; (c) using photoelectrochemical oxidation, electrochemical oxidation and photocatalysis at Ag-ZnO-rGO electrode; and effects of (d) pH and (e) current density on the photoelectrochemical degradation of orange II dye .....  | 28 |
| Figure 3.9. (a) Kinetic plots of photoelectrochemical degradation of orange II dye at pH 5 and 15 mAcm <sup>-2</sup> using rGO, ZnO-rGO and Ag-ZnO-rGO electrodes; (b) photoelectrochemical set-up for the degradation of orange II dye (c) a proposed mechanism for the photoelectrochemical activity of the as-prepared Ag-ZnO-rGO for the degradation of orange II dye.....   | 30 |
| Figure 3.10. Normalised concentration decay versus time plots of the photo-assisted electrochemical degradation of 2-nitrophenol (a) at EG and WO <sub>3</sub> -EG composite electrodes, (b) under electrochemical and photo-assisted electrochemical degradation processes.....   | 31 |
| Figure 3.11. a) UV-Vis spectra of oxidised SMX solution and normalised plots of concentration abatement for b) electrochemical and photoelectrocatalytic degradation of SMX at TiO <sub>2</sub> -EG photoelectrode c) electrochemical degradation of SMX at EG and TiO <sub>2</sub> -EG anodes (experiments carried out at pH 6.3, $j = 10$ mAcm <sup>-2</sup> , [SMX] <sub>0</sub> = 25 mgL <sup>-1</sup> , supporting electrolyte = Na <sub>2</sub> SO <sub>4</sub> ) d) current-dependence of SMX degradation e) effect of bulk solution pH on SMX degradation. ....  | 34 |
| Figure 3.12. A) Chromatogram of SMX solution B) Mass spectrum of SMX solution C) Chromatogram of degraded SMX solution D) Proposed degradation route of SMX by photoelectrochemical process .....  | 36 |

|   |    |
|---|----|
| Figure 3.13. Kinetics curves of (a) electrochemical and photoelectrocatalytic removal of 4-nitrophenol at Pd-ZnO-EG electrode. (b) Photoelectrocatalytic removal of 4-nitrophenol at EG, ZnO-EG and Pd-ZnO-EG electrodes. ....  | 38 |
| Figure 3.14. Degradation kinetics curves of ciprofloxacin of (a) Electrocatalytic and photo-electrocatalytic on MoS <sub>2</sub> -SnO <sub>2</sub> /EG electrode, and (b) photo-electrocatalytic removal on EG, SnO <sub>2</sub> -EG, MoS <sub>2</sub> -EG and MoS <sub>2</sub> -SnO <sub>2</sub> /EG electrodes. c) Proposed plausible charge transfer mechanism.....  | 41 |
| Figure 3.15. (a) CVs of EG, EG-BiVO <sub>4</sub> , EG-ZnO, EG-BiVO <sub>4</sub> /ZnO composite electrodes using 5 mM [Fe(CN) <sub>6</sub> ] <sup>3-/4</sup> in 0.1 M KCl solution at a scan rate of 20 mVs <sup>-1</sup> ; (b) LSV and (c) Photocurrent responses of EG, EG-BiVO <sub>4</sub> , EG-ZnO and EG-BiVO <sub>4</sub> /ZnO in 0.1 M Na <sub>2</sub> SO <sub>4</sub> .....   | 43 |
| Figure 3.16. (a) UV-Vis spectra of PEC degradation of rhodamine B. (b) Normalised concentration decay versus time plot for photocatalytic, electrocatalytic and photoelectrocatalytic degradation of rhodamine B dye on EG-BiVO <sub>4</sub> /ZnO electrode and (c) corresponding kinetics plots. (d) Normalised concentration decay versus time plot for PEC degradation of rhodamine B dye on EG-ZnO, EG-BiVO <sub>4</sub> , EG-BiVO <sub>4</sub> /ZnO electrodes. (e) Effects of current density and (f) pH on degradation of rhodamine B dye. (g) Cycle experiments for the degradation of rhodamine B dye on EG-BiVO <sub>4</sub> /ZnO electrode. .... | 46 |
| Figure 3.17. (a) Scavenger studies of the PEC degradation of rhodamine B dye on EG-BiVO <sub>4</sub> /ZnO. (b) Band alignment between ZnO and BiVO <sub>4</sub> .....   | 48 |
| Figure 4.1. Jar test apparatus.....   | 53 |
| Figure 4.2. EC experimental setup .....   | 54 |
| Figure 4.3. Bulk sample characterisation over time .....  | 56 |
| Figure 4.4. a) Optimum coagulant dosage and settling time determination. b) Pb removal at different settling times and coagulant dosage.....  | 57 |
| Figure 4.5. a) COD removal at different settling times and coagulant dosages. b) Turbidity removal at different settling times and coagulant dosage. c) Effect of initial pH of the bulk sample (Experimental conditions: Dye [] = 38.4 ppm, Pb [] = 25.51 ppm, COD [] = 103 ppm, turbidity of 207 NTU and settling time = 1 h).....  | 58 |
| Figure 4.6. a) EC using Al-Al electrodes (Experimental conditions: Voltage 30 V. Current density = 0.65 mA/cm <sup>2</sup> , inter-electrode spacing = 3.3 cm, t <sub>EC</sub> = 30 min). b) Visual change of colour before and after treatment (EC using Al-Al electrodes).....  | 59 |
| Figure 4.7. At operating parameters: i = 0.65 mA/cm <sup>2</sup> , t <sub>EC</sub> = 30min, inter-electrode spacing = 3.3 cm: a) Removal of orange II dye as function of initial conductivity of sample. b) Removal of Pb as function of initial conductivity of sample. c) Removal of COD as function of initial conductivity of sample. ....  | 63 |
| Figure 4.8. Voltage variation at different initial conductivities and Operational costs in (R/m <sup>3</sup> ) .....  | 64 |
| Figure 4.9. Effect of current density on decolorisation yield (Operating parameters: t <sub>EC</sub> = 30 min, k = 3.8 mS/cm). Graph 2 is an expansion from 95%.....  | 65 |
| Figure 4.10. Effect of current density on Pb removal (Operational parameters: t <sub>EC</sub> = 30 min, k = 3.8 mS/cm) .....  | 65 |
| Figure 4.11. Effect of current density on COD removal (Operational parameters: t <sub>EC</sub> = 30 min, k = 3.8 mS/cm) .....   | 66 |
| Figure 4.12. a) Voltage variation at different current densities and Operational costs in (R/m <sup>3</sup> ). b) Effect of current density on electrode consumption (Operational parameters: t <sub>EC</sub> = 30 min, k = 3.8 mS/cm).....   | 67 |
| Figure 4.13. a) Effect of electrolysis time on the decolourisation yield. b) Effect of electrolysis time on the removal of Pb (operating parameters: i = 8 mA/cm <sup>2</sup> , k = 3.8 mS/cm).....   | 68 |
| Figure 5.1. a) A schematic diagram of a single cell reactor for photoelectrochemical degradation. b) Picture of the actual photoelectrochemical reactor.....  | 73 |

|  |    |
|--|----|
| Figure 5.2. SEM images of a) BiVO <sub>4</sub> and b) CNP/B-BiVO <sub>4</sub> , c) EDS spectrum of CNP/B-BiVO <sub>4</sub> , Elemental maps for d) Boron and e) Carbon, TEM images of f) WO <sub>3</sub> at 1 μm scale, g) WO <sub>3</sub> at 50 nm scale, h) CNP...   | 76 |
| Figure 5.3. UV-Vis absorption spectra of BiVO <sub>4</sub> , WO <sub>3</sub> and CNP/B-BiVO <sub>4</sub> .....   | 76 |
| Figure 5.4. a) Linear sweep voltammograms of photoanodes measured in 0.1 M Na <sub>2</sub> SO <sub>4</sub> , b) Photocurrent response of CNP/B-BiVO <sub>4</sub> and CNP/B-BiVO <sub>4</sub> /WO <sub>3</sub> obtained in 5 mgL <sup>-1</sup> orange II dye (prepared in 0.1 M Na <sub>2</sub> SO <sub>4</sub> ) at a potential of 1.2 V ..... | 77 |
| Figure 5.5. a) Degradation profiles of orange II sodium salt a) at different photoanodes, b) by different oxidation processes. ....  | 79 |
| Figure 6.1. Part of the process design for the flow-through photoelectrochemical reactor.....  | 81 |
| Figure 7.1. Photocurrent responses of photoanodes in the dark and in the presence of solar light (a) Pd-ZnO-EG (b) WO <sub>3</sub> -EG and (c) EG-BiVO <sub>4</sub> /ZnO .....   | 83 |

## LIST OF TABLES

---

|  |    |
|--|----|
| Table 3-1. BET data of EG, ZnO and EG-SiO <sub>x</sub> -ZnO.....   | 20 |
| Table 3-2. Summary of photoanodes and pollutants degraded in this project.....                                     | 26 |
| Table 3-3. Summary of results for degradation studies with WO <sub>3</sub> -EG photoanode.....                     | 32 |
| Table 3-4. Summary of results for degradation studies with TiO <sub>2</sub> -EG photoanode .....                   | 37 |
| Table 3-5. Summary of results for Degradation studies of orange II dye on Pd g-ZnO-rGO photoanode.....             | 39 |
| Table 3-6. Summary of results for degradation studies with MoS <sub>2</sub> -SnO <sub>2</sub> /EG photoanode ..... | 41 |
| Table 3-7. Summary of results for degradation studies with EG-BiVO <sub>4</sub> /ZnO photoanode.....               | 48 |
| Table 4-1. Orange II dye characteristics (de Deus Rodrigues, 2013).....  | 52 |
| Table 4-2. Coagulant dosages .....   | 55 |
| Table 4-3. pH variations .....   | 55 |
| Table 4-4. Bulk sample characteristics (no dilution).....  | 56 |
| Table 7-1. Summary of photoanodes and pollutants degraded in this project.....                                     | 82 |



## ACRONYMS & ABBREVIATIONS

---

|      |  |
|------|--|
| AOP  | Advanced Oxidation Processes               |
| CC   | Chemical coagulation                       |
| COD  | Chemical oxygen demand                     |
| DC   | Direct current                             |
| EAOP | Electrochemical Advanced Oxidation Process |
| EC   | Electrocoagulation                         |
| EG   | Exfoliated Graphite                        |
| EO   | Electrochemical Oxidation                  |
| PEC  | Photoelectrocatalysis                      |
| PEC  | Photoelectrochemical oxidation             |
| rGO  | Reduced graphene oxide                     |
| TOC  | Total organic carbon                       |

This page was intentionally left blank

## CHAPTER 1: BACKGROUND

---

### 1.1 INTRODUCTION

South Africa is classified as a semi-arid country with an annual average rainfall of 490 mm, which is far less than the world average of 860 mm per annum. The country is ranked the 30th driest country in the world with a highly seasonal and variable rainfall. The recent drought (especially in Cape Town) attests to the vulnerability of SA to water crises and may be a pointer to the challenges ahead. While rainfall is a natural phenomenon which may be out of our control, the water management issues in South Africa is also not as impressive.

The water quality of most South African rivers and dams has significantly deteriorated over the past 20 years. These deteriorations, according to a report by World Wide Fund-SA in 2016 (WWF-SA, 2016), have been traced to the following leading causes of fresh water pollution:

1. Poorly treated sewage effluent from failing sewage treatment works;
2. Poor sanitation in informal settlements and rural areas;
3. Mining and ore processing activities, particularly acid mine drainage (AMD);
4. Industrial effluents containing pharmaceutical endocrine-disrupting chemicals in the manufacturing of products such as shampoo, pesticides, dyes and plastics; and
5. Agricultural runoff including fertilisers, sediment and pesticides.

It is not a surprise that industrial effluents and mining activities are leading contributors to the pollution of SA's water pollution. Industrial and mining activities introduce a wide range of pollutants into SA's water bodies. The polluted water is a huge burden to the water treatment processes in many ways. Firstly, the pollution load demands higher need of chemicals especially coagulants and this increases the cost of water treatment. Secondly, the use of higher dosage of coagulants generates more sludge which is a menace to the environment. Thirdly, the efficiency of the treatment reduces because of the recalcitrant nature of some of the organic pollutants in the water. The current or conventional methods were not developed with these newer and stubborn compounds in mind. The poor efficiency is further heightened by the fact that over 35% of SA's wastewater treatment plants are ageing (WWF-SA, 2016)!

There is need to look into complementary and alternative treatment methods for industrial water. There is a need to further diversify the wastewater treatment methods in SA by introducing newer, cheaper, more efficient, more environmentally friendly technologies into SA's water treatment mix. These newer methods do not need to replace the conventional methods but they can be tailored to industrial applications, industrial pretreatment before discharge, industrial water re-use, community or low volume treatment and so on.

This project explored the possibilities of applying electrochemical technologies – photoelectrochemical oxidation and electrocoagulation – to industrial wastewater treatment. Photoelectrochemical oxidation (or photoelectrocatalysis) is a subset of advanced oxidation processes (AOP). Photoelectrochemical oxidation (PEC), just like the more known photocatalysis, involves the use of *in situ* generated hydroxyl radical for the breaking down of complex organic molecules to non-toxic molecules with water and carbon dioxide envisaged as final products. In addition to the excitation of semiconductor by light, PEC uses electrical energy (potential) to drive the electron generated to minimise the recombination of electron-hole pairs on the semiconductor

surface. Electrocoagulation (EC), on the other hand, is an electrochemical technology that generates coagulating ions *in situ* from a sacrificial anode. This technique has been shown to be cheaper and more environmentally friendly than the conventional chemical coagulation.

The major challenges in AOP include the recombination of the electron-hole pair of the semiconductor and the recovery of the catalyst. These challenges are mitigated in PEC because the addition of potential to the photocatalysts further drives away the electron from the valance band holes. This allows more time and catalytic sites for the generation of hydroxyl radical and the degradation of the pollutant. The challenge of catalyst recovery is absent in PEC because the catalyst has already been immobilised on a solid support – the electrode. PEC is thus potentially a better approach than photocatalysis.

In order to improve the performance of PEC, the use of solar light in the place of uv light needs to be sought after. Furthermore, percentage removal of the pollutants should be increased. The aforementioned need are largely dependent on the materials used in PEC. Thus, there is need to quest for newer materials or tune the existing materials towards white (solar) light excitation and improved performance.

Electrocoagulation is generally based on the use of two types of anodes – iron and aluminium. There is need to explore other types of materials and also hybrid materials so as to make the EC process more robust. Traditionally, EC is used for metal removal but it can also be used for the removal of organic pollutants. There is also a possibility of assisting EC process with light.

It is believed that the introduction of newer technologies for wastewater treatment will alleviate the challenge of water pollution in South Africa–this work is a step in this direction.

## 1.2 PROJECT AIMS

The general aim of this proposal is to develop and integrate electrocoagulation and photoelectrochemical oxidation unit operations based on novel mixed nanomaterials into a reactor system for the treatment of industrial wastewater.

Specific objectives were as follows:

1. To incorporate electrocoagulation as a unit operation into water treatment in a jar test experiment.
2. To evaluate the performance (metal removal, COD removal, turbidity removal, etc.) of electrocoagulation over coagulation using simple electrode configuration and novel carbon cathode.
3. To understand the morphology, chemical and electrochemical behaviours of novel nano carbon materials and composites for photoelectrochemical oxidation.
4. To understand the applicability of these materials as photoanodes and cathodes under various conditions as it relates to wastewater treatment.
5. To evaluate the performance of photoelectrochemical oxidation unit operation in a jar test experiment for wastewater treatment.
6. To evaluate the efficiency of (solar) photoelectrochemical reactors developed from these materials in the presence of selected standard dye/organic polluted water and real sample wastewater.

7. To interrogate the kinetics, degradation products and mechanism of the degradation processes.
8. To generate data that can explain the performance of a pre-pilot (prototype) reactor consisting of both electrocoagulation and photoelectrochemical unit operations towards different types of wastewater.
9. To study the effect of different reactor configurations based on different material combinations

## **CHAPTER 2: LITERATURE REVIEW: ELECTROCOAGULATION AND ELECTROCHEMICAL ADVANCED OXIDATION PROCESSES IN WATER TREATMENT**

---

### **2.1 INTRODUCTION**

Water is a necessity for life and therefore the need to effectively manage the limited water resources cannot be overemphasised. Water management involves a lot of activities or processes such as water use, water harvesting, water distribution, wastewater release, water treatment and a lot more. Conventional water treatment unit operations consist mainly of coagulation, sedimentation, filtration, disinfection and storage. The efficiency and cost of conventional treatment method are being challenged by the chemical complexity arising from the feed water (influent) which consists of a cocktail of organic, inorganic and pathogenic pollutants from different sources. One of such feed water are industrial effluents, which can consist of a heavy dose of pollutants of which some are resistant to normal wastewater treatment. These pollutants have negative impacts on water quality and the safety of the plants and animals in the environment. Industrial effluents are sometimes released into water bodies untreated and unfortunately, these heavily polluted water bodies do not only endanger lives; but they also create extra burden to the municipal wastewater treatment plants. For example, dye effluents and some other organic pollutants have been shown to be resistant to the current treatment methodologies (Vogelpohl & Kim, 2004). Furthermore, the cost of water treatment increases owing to the pollutant load which fouls membrane/filters and necessitates for more frequent replacements and higher dosage of chemicals. In coagulation unit operation for example, a heavily polluted water will require a higher amount of coagulant, which leads to the production of more sludge. Sludge is becoming a menace to our environment.

To avert or minimise the challenges posed by industrial wastewater, pre-treatment before discharge is very important. There is a need to develop new or improved methods that can be used to pre-treat and/or treat industrial wastewater before discharge. Such methods can be developed and applied on-site by industries before discharge and/or incorporated into the process operations of water treatment plant. These methods must i) use less chemicals (coagulants and disinfectants); ii) lead to less sludge formation; iii) be able to remove recalcitrant pollutants and metals iv) be environmental friendly; v) be easy to design and used at industrial or power plant locations; vi) be easy to design and incorporated into the treatment process. One set of methods that fits into these listed conditions are electrochemical methods and in general, electrochemical advanced oxidation processes. The two electrochemical unit operation of interests are electrocoagulation (Khandegar & Saroha, 2013) and photoelectrochemical oxidation (Brillas & Martínez-Huitle, 2015; M. G. Peleyeju & Arotiba, 2018; Shannon et al., 2008).

## **2.2 CHALLENGES WITH CONVENTIONAL TREATMENT METHODS**

The increase in the chemical complexities and pollution load of feed water or wastewater has become a huge challenge to conventional water treatment methods. Thus, these methods are becoming more chemically, more operationally, and more energy intensive (Vogelpohl & Kim, 2004). Conventional system tend to form toxic secondary by-product resulting from the pre-concentration and phase changes of some pollutants leading to difficulties in disposal (Shannon et al., 2008). In addition to these shortcomings, some pollutants are resistant to these conventional treatments and continue to persist in the environment.

Organic pollutants form a major category of water pollutants and typical examples include detergents, insecticides and herbicides, pharmaceutical wastes, dyes, petroleum residues and so on. Some of these organic pollutants are very difficult to remove from wastewater and they have been shown to persist in the environment – hence the name persistent organic pollutants (POPs). Organic pollutants present many health hazards such as endocrine disruption, cardiovascular disease, cancer and a lot more. The removal of metals such as arsenic, lead, selenium, etc. from industrial wastewater is also very necessary to reduce the inorganic load of the feed water into the treatment plant.

## **2.3 ELECTROCOAGULATION**

### **2.3.1 Coagulation and Electrocoagulation**

Generally, a water treatment plant consists of the following unit operations: coagulation/flocculation, sedimentation, filtration and disinfection. Chemical coagulation is the use of chemicals to destabilise the electrical forces that stabilises colloidal particles in an aqueous phase. Coagulation is a very important unit operation in water treatment (either drinking water or wastewater). Coagulation (which is usually followed by flocculation) is used mainly for the removal of turbidity (sedimentation of suspended and colloidal particles) from water. Furthermore, coagulation helps in the decolourisation of water and in the removal bacteria. Coagulants (the chemicals used in coagulation) are usually based on Al or Fe and other polymers such as polyaluminium chloride.

The use of chemical coagulants in the traditional coagulation system is impeded by a) the high cost of chemicals especially when the pollution load is high, b) its sensitivity to important water parameters such as pH, alkalinity, zeta potential, c) its sensitivity to temperature (winter and summer present different challenges) and d) its generation of high amount of sludge. A heavily polluted wastewater influent will require a higher dosage of coagulants, which increases cost and sludge formation. Furthermore, if coagulation is impeded, turbidity will be a problem. A water with a high turbidity is an indication of pollution and such water is difficult to disinfect and pose problems downstream. These challenges can be mitigated by electrocoagulation (Khandegar & Saroha, 2013) which has the following advantages over coagulation: a) simple configuration, b) more reduced turbidity, c) lower sludge amount, d) sludge formed are easier to handle and de-water, e) removes smaller and wider range of particles, d) requires less maintenance and a lot more, e) better metal, organic and pathogen removal.

### 2.3.2 Electrocoagulation

Electrocoagulation (EC) is the process of destabilising suspended, emulsified, or dissolved contaminants in an aqueous medium by introducing an electric current into the medium (Emamjomeh & Sivakumar, 2009) (Emamjomeh and Sivakumar, 2009). Electrocoagulation is the electrochemical production of destabilising agents or ions such as Fe and Al that results in the neutralisation of the electric charges for pollutant removal. A search in ISI web of knowledge database using the keywords 'electrocoagulation' and 'wastewater' returned the following publications: 13 (1990-2000); 331 (2001-2010); 551 (2011-April 2016). The upsurge of research in electrocoagulation suggests the potential of this method for water treatment. Detailed information on electrocoagulation process and its application to textile effluents, natural organic matter, metals (chromium, arsenic, selenium), and its advantages over coagulation have been reported (Demirbas & Kobya, 2017; Emamjomeh & Sivakumar, 2009; Khandegar & Saroha, 2013; Mohora et al., 2014; Ulu, Barışçı, Kobya & Sillanpää, 2015). Electrocoagulation has the potential of improving the coagulation and flocculation of colloids and suspended solids in wastewater. The fact that colloid stability is electrical in nature suggests that electrochemical system may be more appropriate than chemical process.

Electrocoagulation has the following advantages over coagulation (Khandegar & Saroha, 2013; Kruthika, Karthika, Raju & Prabhakar, 2013): a) simple configuration, b) more reduced turbidity, c) lower sludge amount, d) sludge formed are easier to handle and de-water, e) removes smaller and wider range of particles, d) requires less maintenance and a lot more, e) better metal, organic and pathogen removal.

### 2.3.3 Anodic and cathodic materials in EC

Electrocoagulation (EC) usually consists of a sacrificial anode and the same or different metallic cathode. The two most commonly used anodes are Al (Chellam & Sari, 2016; Harif, Khai & Adin, 2012) and Fe (Kobya, Ozyonar, Demirbas, Si & Oncel, 2015; Patel, Ruparelia & Patel, 2011). More recently new anodes such as Zn (Fajardo, Rodrigues, Martins, Castro & Quinta-Ferreira, 2015; Y. Wang et al., 2016) and Cu (Prajapati, Chaudhari, Pal, Chandrakar & Choudhary, 2016) have been introduced. Wang et al. attempted to use zinc anode in the electrocoagulation of perfluorooctanoate. In their work, they results obtained suggested that Zn can be a suitable anodic material in electrocoagulation (Y. Wang et al., 2016). The most commonly used cathodic materials are Al and Fe. However, the use of other cathodes such as stainless steel (Harif et al., 2012) and carbon (Y. Tian et al., 2016) have been reported. Tian et al. (Y. Tian et al., 2016) used air breathing carbon cathode (with Al anode) to remove nutrients from wastewater. An exhaustive list of publications (over 50) where the anode-cathode materials are listed can be consulted in the excellent review article on EC by Khandegar and Saroha (Khandegar & Saroha, 2013).

Recent developments in EC focus on the use of other types of anodic and cathodic materials, cell configuration and mechanistic studies. Aoudj et al. (Aoudj, Khelifa, Drouiche, Belkada & Miroud, 2015) used a combination of Al and Fe in the anode compartment of an electrocoagulation cell for the removal of Cr(VI) and F<sup>-</sup>. Other reports on hybrid electrodes are now emerging though very scanty (Ozyonar, 2016; Ulu et al., 2015). EC has been used in the removal of a myriad of pollutants from different sources or industries. The application of EC for the removal of metal, natural organic matters, nutrient and a wide range of organic pollutants in water or



wastewater has been reported. Recent reviews (An, Huang, Yao & Zhao, 2017; Garcia-Segura, Eiband, de Melo & Martínez-Huitle, 2017; Hakizimana et al., 2017; Moussa, El-Naas, Nasser & Al-Marri, 2017) on EC have highlighted these applications.

## 2.4 ELECTROCHEMICAL ADVANCED OXIDATION PROCESSES (EAOPS)

One of the upcoming water treatment methodologies is a group of methods called advanced oxidation processes (AOPs). Advanced oxidation processes (AOPs) have been widely recognised as highly efficient treatments for wastewaters. AOPs are known to degrade organic pollutants which are resistant to traditional technologies (Hai, Yamamoto & Fukushi, 2007). A subset of AOP that involves electrochemical oxidation is now referred to as electrochemical advanced oxidation processes EAOPs (Moreira, Boaventura, Brillas & Vilar, 2015). Advanced oxidation processes are environmentally friendly chemical, photochemical, photocatalytic, electrochemical and photoelectrochemical technologies based on the production of hydroxyl radical ( $OH^\bullet$ ) (Moreira, Boaventura, Brillas & Vilar, 2017). After fluorine, hydroxyl radical is the strongest known oxidant. These radicals are able to oxidise almost any organic molecule yielding  $CO_2$  and inorganic ions at rate constants in the range  $10^6$ - $10^9$   $Ms^{-1}$  for most reactions in aqueous solutions (Garza-Campos et al., 2014).

Electrochemical oxidation is one of the widely used EAOPs. The process is generally accompanied by side reactions such as oxygen or chlorine evolution, which reduce its efficiency. Also, heterogeneous photocatalysis, which involves the use of a semiconducting photocatalyst (e.g.  $TiO_2$ ), suffers from low photo efficiency resulting from slow rate of electron transport and high rate of recombination between photo-generated electron/hole pairs. These shortcomings can be improved by the combination of electrochemical oxidation systems with photocatalysis. The combination of these processes can alleviate the problems associated with electron/hole recombination by driving away the photoelectrons from the semiconductor/electrolyte interface, leading to more efficient degradation of organics upon application of electrical energy (Brillas & Martínez-Huitle, 2015). The combination of these processes, generally termed photoelectrochemical processes, is fast becoming a plausible route to organic waste degradation in water treatment (Brillas & Martínez-Huitle, 2015). In recent times, the application of electrochemical advanced oxidation processes such as photoelectrochemical oxidation and photoelectro-Fenton (PEF) for an effective, efficient and fast mineralisation of toxic organic pollutants in wastewater treatment have been the focus of many researchers (C.-F. Liu, Huang, Hu, Juang & Huang, 2016; Neumann-Spallart, Shinde, Mahadik & Bhosale, 2013; M. G. Peleyeju et al., 2017; Salazar, Garcia-Segura, Ureta-Zañartu & Brillas, 2011; Umukoro, Peleyeju, Ngila & Arotiba, 2017).

A typical photoelectrochemical oxidation process involves the immobilisation of  $TiO_2$  powder (a photoactive material) on a conductive material upon which a bias anodic potential is applied (Butterfield et al., 1997). The main advantages of the immobilisation of the catalyst are the avoidance of losses in the recovery process and enhanced photocatalytic efficiency through the use of an external electric field (Moreira, Garcia-Segura, Vilar, Boaventura & Brillas, 2013). We have used EAOP in our laboratory for the degradation of organic pollutants such as nitrophenol (B Ntsendwana, Sampath, Mamba & Arotiba, 2013), trichloroethylene (B. Ntsendwana, Mamba, Sampath & Arotiba, 2013), and industrial dye (Ama, Mabuba & Arotiba, 2015). Our studies revealed

that degradation efficiency increases when electrochemical oxidation is photochemically enhanced. We have also demonstrated the effect of materials such as  $\text{TiO}_2$ ,  $\text{ZnO}$  and diamond (B. Ntsemdwana, Peleyeju & Arotiba, 2016; B. Ntsemdwana, Sampath, Mamba, Oluwafemi & Arotiba, 2016).

The nature of electrodes significantly influences electrochemical processes. A suitable electrode material for electrochemical oxidation should exhibit properties such as high physical and chemical stability, resistance to corrosion, high electrical conductivity, catalytic activity and selectivity, and low cost/life ratio. Carbon-based electrodes represent an attractive electrode material for electrochemical and photoelectrochemical oxidation. They exhibit superior electrochemical properties to those of noble metals towards oxidation and reduction of organic and biological molecules in both aqueous and non-aqueous media (Neumann-Spallart et al., 2013). The choice of semiconductors for photoelectrochemical systems are equally important. Such semiconductors should be photoactive, biologically and chemically inert, stable toward photo-corrosion and suitable towards visible or near UV light. Such semiconductors should also be inexpensive and non-toxic. Various semiconductors such as metal oxides, sulphides, nitrides and selenides have been investigated in this regard.  $\text{TiO}_2$  and  $\text{ZnO}$  photocatalysts have been extensively studied and applied for the removal of organic compounds from contaminated air and water and for microbial disinfection. In particular,  $\text{ZnO}$  is known to be an efficient photocatalyst material compared to other metal oxides (Kansal, Singh & Sud, 2007). More recently, semiconductors such as  $\text{WO}_3$ ,  $\text{BiVO}_4$  are being investigated as anodic component in photoelectrochemical degradation (M. G. Peleyeju & Arotiba, 2018).

As seen from the discussions above, photoelectrochemical methods (which includes solar and electro-fenton) have great potentials in wastewater treatment. This method is still at its infancy and there a lot that can be done. Since this technology depends heavily on the nature of the electrode, new or improved cathodic and anodic materials can be prepared. Such material should exhibit better performance in terms of robustness, stability, over-potential, photocatalysis, solar light harvesting, more efficient radical generation, cost and so on. The preparation, characterisation and application of novel carbon materials such as carbon nanodots (Katherine Lawrence et al., 2014), carbon nanoparticle (Tshwenya & Arotiba, 2017), various carbon mix (nanodots, diamond) and new carbon semiconductor composites in the design of solar photoelectrochemical reactors for wastewater treatment can be plausible approaches in the design of photoelectrochemical reactors. Furthermore, the design of photoanodes based on nanocomposites of  $\text{ZnO}$ ,  $\text{WO}_3$  and other quantum dot doped semiconductors are areas that can be explored for photoanode performance improvements.

## 2.5 COMBINATION OF EC AND EAOP

A recent trend in the application of EC is its combination with other advanced oxidation processes. The most common is the combination of EC with electrochemical oxidation (Bhagawan, Poodari, Golla, Himabindu & Vidyavathi, 2016; El-Ashtoukhy, Amin, El-Latif, Bassyouni & Hamad, 2017; Esfandyari et al., 2015; García-García et al., 2015; Rubí-Juárez, Barrera-Díaz, Linares-Hernández, Fall & Bilyeu, 2015; Thiam, Zhou, Brillas & Sirés, 2014; Unal, Dizge, Karagunduz & Keskinler, 2019). Garcia-Garcia et al. (García-García et al., 2015) combined EC with EO to treat industrial wastewater. In their report, they used solar cell as the source of current

and used a copper anode for electrocoagulation. Suarez-Escobar (Suárez-Escobar, Pataquiva-Mateus & López-Vasquez, 2016) combined EC with photocatalysis using a monopolar arrangement of iron electrodes for EC and  $\text{TiO}_2$  semiconductor and uv light for photocatalysis. A combination of EO and peroxi-electrocoagulation was enhanced by the addition of  $\text{H}_2\text{O}_2$  in a report by Esfandyari et al. (Esfandyari et al., 2015). Investigations and reports on the combination of EC with other methods are bound to continue as researchers look into different ways of combining these very important techniques.

## **CHAPTER 3: SYNTHESIS, CHARACTERISATION AND PHOTOELECTROCHEMICAL DEGRADATION STUDIES OF CARBON BASED SEMICONDUCTOR PHOTOANODES**

---

### **3.1 INTRODUCTION**

The availability of clean water for industrial and domestic use is a well-known global challenge owing to increase in dosage and complexity of water pollutants. The discharge of organic waste into water bodies is on the increase and these organic wastes pose a lot of health and environmental risk to living organism (Davey & Schäfer, 2009; Schwarzenbach et al., 2006). Dyes are a typical group of organic pollutants, which can originate from industrial effluents generated by paints, textiles, leathers, and printing industries. The presence of dye in water or wastewater is hazardous to human and aquatic lives and because dyes are recalcitrant during treatment by the conventional water treatment methods, they may persist even in treated water. The toxic and recalcitrant characteristics of dyes necessitate the need to develop other treatment methods as alternatives and complements to the existing conventional techniques. Largely, the development of these alternative water treatment approaches depends on the nature of the material used in the design. The quest for new material or the improvement of currently existing materials has been the focus of many researchers in their bid to provide alternative methods for water treatment. Some of these materials include carbon, metal oxide semiconductors, polymers and a lot more. Carbon has been a material of interest in the fabrication of electrodes owing to their unique properties and wide applicability. Examples of such carbon include graphite, carbon nanotubes, graphene and others that are not well known such as exfoliated graphite, carbon nanoparticle, etc.

Exfoliated graphite (EG), a carbonaceous material that possesses low density, large surface area, compressibility, high temperature resistance, and high electrical conductivity. Its porous nature enhances the trapping of photocatalyst, and thus, reduces the loss of the photocatalyst (B. Ntsewana et al., 2013; B Ntsewana et al., 2013; M. Peleyeju, Umukoro, Babalola & Arotiba, 2016). It is very stable and can be prepared in large scale (J.-h. Li, Liu & Da, 2007). In addition, EG has been reported for its electrocatalytic property which made it viable for the electrochemical sensing and the electrochemical oxidation of pollutants (Ndlovu, Arotiba, Sampath, Krause & Mamba, 2011; B. Ntsewana et al., 2013). Furthermore, its application in vibration damping, thermal insulation, shielding of electrochemical interference and gaskets have been reviewed (Q. Zhao, Cheng, Wu & Yu, 2014).

Graphene/graphene oxide/reduced graphene oxide, made by exfoliating graphite, is a form of exfoliated graphite which comprises of  $sp^2$ -bonded carbon atoms packed tightly into 2-D planar honeycomb lattices with special properties like high surface area, high mechanical stability, high thermal and electrical conductivities, and very good electron mobility (Umukoro, Peleyeju, Ngila & Arotiba, 2016b).

Carbon nanoparticles (CNPs), another form of carbon, are slowly attracting attention owing to their ease of synthesis, fluorescent nature, relatively low/non-toxicity, high surface area and functionalisability (Watkins

et al., 2010). These materials are referred to as carbon nanoparticles (CNPs) because they consist primarily of carbon in the form of nearly spherical particles that are between 10 and 100 nm in size (K. Lawrence et al., 2014). Additionally, they usually contain oxygen and hydrogen which makes them hydrophilic, and soluble in aqueous solutions (K. Lawrence et al., 2014).

The modification of CNPs (and other nanocarbons) either by physical or chemical treatments, is known to induce new properties or enhance some already existing properties (Q. Li, Yu, Qiu, Zhou & Wu, 2008). Surface modification is best needed to break the strong cohesive forces that cause aggregation, thus promoting dispersibility and stability of the particles (Trostová, Stibor, Karpíšková, Kolská & Švorčík, 2013). Functionalisation of amide-amine type is considered as one of the best methods to introduce these desirable properties (K. Lawrence et al., 2014), making CNPs ideal for various applications including catalysis, medicine, and water purification (Tshwenya & Arotiba, 2017). Thus, studies on alternative synthesis routes (especially low cost and high yield) and functionalisation of CNPs will be plausible so as to widen the applicability of this relatively new nanocarbon.

While carbon are versatile conducting support, the fabrication of a photoanode necessitates the use of photocatalytic semiconductors. These semiconductors possess band gaps that can be activated by uv or visible light resulting in electron-hole pair needed for radical generation. Titania ( $\text{TiO}_2$ ) is the most applied semiconductor in photocatalysis. However, zinc oxide has also been found as an alternative semiconductor to  $\text{TiO}_2$  as a result of its low cost, non-toxicity, chemical inertness, good optoelectronic and catalytic properties (Di Paola, García-López, Marci & Palmisano, 2012; Ma, Xue, Zhou & Zhang, 2014); but its wide band gap (3.37 eV) limits its utilisation of visible light. The absorption of light in the visible spectrum by ZnO can be improved by the introduction of Ag due to its surface plasmon resonance effect (Feitai Chen, Liu, Liu, Fang & Dai, 2013; S. Liu et al., 2015). Moreover, Ag can be incorporated as an electron sink for the generated electrons. Hence, it enhances the generation of more hydroxyl radicals by the electrons and holes, and therefore, improves the degradation process of the pollutants (Qin et al., 2015; Umukoro, Peleyeju, Ngila & Arotiba, 2016a). Furthermore, the mobility of both holes and electrons can be enhanced by the Dirac cone of the band structure of a carbon material such as EG or its other form like graphene oxide/reduced graphene oxide. Hence the photogenerated electrons and holes from the ZnO can be transported to the EG or the graphene material (Fenghua Chen et al., 2014; Umukoro, Peleyeju et al., 2018). Consequently, the rate of recombination of the electron-hole pairs would be minimised and the efficiency of ZnO in the composite electrode would be enhanced.

It can be hypothesised that the combined properties of ZnO and EG will yield an improved material with good excitation and enhanced photocatalysis. In addition, a nanocomposite of Ag, ZnO and reduced graphene (rGO) called Ag-ZnO-rGO, can result in improved photoelectrochemical performance. It was earlier reported that n-ZnO/p- $\text{Cu}_2\text{O}$ /n- $\text{TiO}_2$  nanotube arrays was prepared and applied as electrode for the photoelectrocatalytic degradation of tetracycline. The results showed an excellent photoelectrocatalytic activity due to the ternary heterojunction of the material (J. Li et al., 2013). Photoelectrochemical oxidation of salicylic acid and salicylaldehyde has been carried out on titanium dioxide nanotube arrays, giving over 83% removal of both organics (M. Tian, Adams, Wen, Asmussen & Chen, 2009). The use of Zn-Co-layered double hydroxides nanowalls has been reported as electrocatalyst for the electrochemical oxidation of water (Y. Li, Zhang, Xiang,

Yan & Li, 2014). Few studies have been carried out on Ag/ZnO/rGO and some of these involve the use of Ag/ZnO/rGO as gas sensor (Uddin, Phan & Chung, 2015) and as a photocatalysts for dyes removal (Meng, Shao, Fan, Wang & Li, 2014; Qin et al., 2015). However, to the best of our knowledge, Ag-ZnO-rGO composite electrode has not been employed as a photoanode for the photoelectrochemical degradation of dyes. This project has produced water treatment data based on ZnO anodes modified with graphene, palladium and silver (Umukoro, Madyibi et al., 2017; Umukoro, Peleyeju et al., 2018; Umukoro et al., 2016a, 2016b). This chapter discusses the synthesis and characterisation of the different anodic components used in PEC degradation. Such materials include exfoliated graphite (EG), reduced graphene oxide (rGO), EG-ZnO, Ag-ZnO composite, Ag-ZnO-rGO composite, WO<sub>3</sub> nanoparticles, WO<sub>3</sub>-EG composite, TiO<sub>2</sub>-EG electrode, Pd-ZnO-EG, EG, SnO<sub>2</sub>-EG, MoS<sub>2</sub>-EG, etc. Discussions on the phototelectrochemical degradation profiles of the photoanodes prepared from these materials are presented. The results around each of the photoanodes systems are summarised and presented as sub-conclusions and tables.

## 3.2 METHODOLOGY

### 3.2.1 Materials and Instrumentation

Potassium hydroxide, silver nitrate, ascorbic acid, natural graphite flakes, sulphuric acid (98%), sodium nitrate, potassium permanganate, hydrogen peroxide, zinc nitrate hexahydrate, absolute ethanol (99.9%) and orange II dye. All reagents were purchased from Sigma Aldrich, Germany, and were of analytical grade and they were used without further purifications. Reduced graphene oxide (rGO), ZnO and the composites were characterised using x-ray diffractometer (Rigaku Ultima IV, Japan) at 40 kV and 30 mA with Cu K $\alpha$  radiation ( $\lambda=0.15406$ ) with K-beta filter. This was carried out using scintillation counter ranging from 5-90° at a speed of a 2°/min. The studies of surface morphology of the as-synthesized materials were done using transmission electron microscopy (JEOL 2100 HRTEM 200V, Japan), scanning electron microscopy (SEM) (TESCAN, Vega 3 XMU, Czech Republic). The surface elemental composition was obtained using energy-disperse x-ray spectrometer (EDS) (TESCAN, Czech Republic) which was attached to the SEM. Spectroscopic studies were carried out using Perkin Elmer FTIR spectrometer (Spectrum 100, USA) and Perkin Elmer Raman microscope (Raman micro 200, USA) to obtain the FTIR and Raman spectra, respectively. Decolourisation of the dye was investigated using UV-Visible spectrophotometer (Cary 60, Agilent technologies, Australia). New Port 9600 Full Spectrum Solar Simulator equipped with 150 W ozone free xenon lamp which produces a collimated beam of 33 mm diameter (equivalent to 1.3 sun) was used as the light source. All characterisation experiments were performed at the University of Johannesburg.

### 3.2.2 Preparation of exfoliated graphite

Exfoliated graphite (EG) was prepared from natural graphite as follows: Intercalation of natural graphite particles (300-400  $\mu\text{m}$ ) were carried out by immersing the particles in a mixture of concentrated H<sub>2</sub>SO<sub>4</sub>/HNO<sub>3</sub> (3:1 v/v) for 24 hrs at ambient conditions. The graphite intercalated material was then washed with water and air-dried. Exfoliation was then carried out by subjecting the graphite intercalated material to a temperature shock at 800°C in a furnace for a minute in air resulting in puffed-up EG material.

### 3.2.3 Preparation of reduced graphene oxide (rGO)

Graphene oxide was prepared by exfoliating graphite using a modified Hummer's method (Poh et al., 2012), and then reduced using ascorbic acid by a method described by Zhang et al. (Jiali Zhang et al., 2010). In brief, 5 g of graphite flakes were added to 2.5 g of sodium nitrate and 115 mL of sulphuric acid. The mixture was mixed and stirred vigorously. The mixture was allowed to cool in an ice-bath and 15 g of potassium permanganate was added to the mixture over a period of 2 h. The mixture was allowed to cool in an ice-bath to room temperature and then heated to 35°C for 30 min. Then, it was poured into 250 mL of de-ionised water in a flask and heated to 70°C. The mixture was poured into 1 L of de-ionized water after keeping the temperature constant for about 15 min. A 30 mL volume of 3% hydrogen peroxide was added to remove any unreacted  $\text{KMnO}_4$  and manganese dioxide in the mixture. Then, it was washed several times by centrifugation and filtration using de-ionised water until a pH of 6 was obtained. The resulting graphite oxide was then ultrasonicated for 2 h to obtain graphene oxide and then dried in an oven at 60°C for 48 h. Furthermore, 5 g of ascorbic acid was added to an aqueous suspension which contained 0.1 g of the prepared graphene oxide in 50 mL of deionised water and sonicated for 30 min. The resultant suspension was stirred at 90°C for 48 h. Then, the product – reduced graphene oxide – was filtered and dried at 60°C overnight before use.

### 3.2.4 Preparation of EG-ZnO nanocomposite

For the preparation of the EG-ZnO nanocomposite, methanol (about 10 mL), ZnO (80 mg), and methyltrimethoxysilane (MTMOS) (100 mg) were mixed in a vial (20 mL) and sonicated for 15 min to ensure uniform dispersion of ZnO. EG (100 mg) was subsequently added and the mixture shaken for 5 min. After the addition of 1 M HCl (0.1 mL), the mixture was allowed to hydrolyse for 3 h in a closed vessel and poured in a Petri dish to dry. The contents of the Petri dish were constantly mixed for uniform distribution of ZnO on the EG. After drying for 24 h at room temperature, the floating catalyst was incubated at 90°C for 24 h to remove residual methanol (B. Ntsendwana, Sampath et al., 2016).

### 3.2.5 Preparation of Ag-ZnO nanoparticles

The Ag-ZnO composite was synthesised using a modified co-precipitation method (Umukoro et al., 2016b). In brief, a solution containing 14.87 g of zinc nitrate hexahydrate and 0.149 g of silver nitrate dissolved in 100 mL of de-ionised water was prepared. A 3 M KOH solution was added drop-wise while stirring vigorous until the pH of the solution reached 10. Then, it was further stirred for 2 h at a very high speed. It was observed that the viscosity of the mixture increased with increase in the amount of KOH solution added. The product obtained was centrifuged, and washed with de-ionised water and ethanol several times. Subsequently, it was dried in an oven at 60°C for 12 h and calcined at 400°C for 2 h. The ZnO was prepared in a similar way without the addition of silver nitrate.

### 3.2.6 Preparation of Ag-ZnO-rGO composite photoanode

A sample of 100 mg of the as-prepared Ag-ZnO was dispersed in about 10 mL methanol and sonicated for 20 min to obtain a uniform dispersion. A 100 mg mass of rGO was added to the dispersion and stirred vigorously

for another 10 min. Then, the mixture was poured into a dish and dried in the oven at 90°C for about 48 h for the complete removal of the methanol to obtain the Ag-ZnO-rGO composite. The as-prepared Ag-ZnO-rGO composite was compressed into pellet of 1.3 cm in diameter using a press machine at a very high pressure. Then the pellet was used to fabricate a photoanode with the aid of a glass rod, conduction silver paint, copper wire and epoxy resin. One end of the copper wire in the glass tube was coiled to form a flat surface. The pellet was placed on the surface using the conductive silver paint which enabled the conduction between the copper wire and the composite (B Ntsendwana et al., 2013). It was allowed to dry in the air for about 1 h. The edge of the pellet was covered with epoxy resin so that electron flow is mainly from the basal plane.

### **3.2.7 Preparation of WO<sub>3</sub> nanoparticles**

WO<sub>3</sub> nanoparticles were prepared by a precipitation method in the presence of citric acid (Sánchez-Martínez, Martínez-De La Cruz & López-Cuellar, 2013). Precisely, 6.9079 g of ammonium metatungstate hydrate was dissolved in 30% v/v, nitric acid solution (50ml) at 70°C while stirring. The temperature was maintained while the solution was being stirred until a yellow precipitate was formed. Heating was continued at that temperature until the water was completely evaporated. The solid obtained was subjected to thermal treatment at 600°C for 3 h to produce the WO<sub>3</sub> nanoparticles.

### **3.2.8 Preparation of WO<sub>3</sub>-EG composite**

Natural graphite was sieved using a 300 µm sieve mesh and intercalated by being soaked in concentrated nitric acid and sulphuric acid mixture in a ratio of 1:3 by volume for 48 hours at room temperature. The intercalated material was then washed to pH 7 and air-dried. It was further exfoliated by subjecting it to temperature of 800°C for about a minute to obtain a puffed up exfoliated graphite material.

For the preparation of the WO<sub>3</sub>-EG composite, a known amount of the as-prepared WO<sub>3</sub> was dispersed in absolute ethanol and sonicated for 30 min to obtain uniformity of suspension of the nanoparticles. Then, an equal amount of EG was added and further sonicated for 10 min after which the mixture was put in an oven to dry at 100°C overnight to achieve complete evaporation of the ethanol.

### **3.2.9 Fabrication of WO<sub>3</sub>-EG composite electrode**

The as-prepared WO<sub>3</sub>-EG composite was compacted into a pellet that is 1.3 cm in diameter by a hydraulic press at a high pressure of 10000 psi. The pellet was employed for the construction of an electrode with the use of a copper wire, non-conductive epoxy resin and conductive silver paint. The WO<sub>3</sub>-EG composite pellet was placed on the coiled part of the copper wire with the assistance of the conductive silver paint and allowed to dry. The edge of the composite pellet was sealed with the resin to allow the flow of electricity from only the basal plane. Furthermore, it was put in a glass rod before being used for the experiment.



### 3.2.10 Electrochemical and photoelectrochemical experiments

Electrochemical and photoelectrochemical studies were conducted using  $[\text{Fe}(\text{CN})_6]^{3-/4-}$  in 0.1 M KCl solution as the redox probe and 0.1 M  $\text{Na}_2\text{SO}_4$  as the supporting electrolyte on an Autolab (302N) potentiostat/galvanostat electrochemical station with a three-electrode system having Ag-ZnO-rGO (1.3 cm) as working electrode, Ag/AgCl (3.0 M KCl) as the reference electrode and platinum foil as the counter electrode. The degradation experiments were conducted in a 100 mL quartz cell photoreactor which contained the orange II dye solution and the electrodes. The working electrode was positioned to receive the light coming from the source of light. The potentiostat/galvanostatic was utilised as the source of power for the electrochemical degradation of the dye in a 0.1 M sodium sulphate solution as a supporting electrolyte. The source of light was a New Port 9600. The distance between the simulator and the reactor is 10 cm so as to produce a beam power equivalent to 1 sun. In the case of electrochemical oxidation of the dye, only potential was applied. For photocatalytic degradation, only light was utilised, while both potential and light were applied for the photoelectrochemical degradation of the dye. At intervals of 30 min, an aliquot (5 mL) of solution was withdrawn from the cell using a disposable syringe and filtered using a 0.4  $\mu\text{m}$  PVDF membrane filter for a period of 210 min. The degradation was measured using a UV-Vis spectrophotometer (Cary 60, Agilent) at an absorption band of  $\lambda = 483 \text{ nm}$ , and with the aid of TOC analyzer (Teledyne Tekmar TOC fusion).

## 3.3 RESULT AND DISCUSSION

### 3.3.1 Spectroscopic characterisation for EG-ZnO

**X-ray diffractometry for EG-ZnO.** The X-ray diffraction pattern of the EG exhibits characteristic peak at  $2\theta = 26.7^\circ$  assigned to 200 diffraction plane of hexagonal phase graphitic structure which confirms complete exfoliation of graphite as shown in Fig. 3.1a. The X-ray diffraction pattern of ZnO nanostructures (Fig. 3.1b) shows diffraction peak at  $2\theta$  values of  $31.78^\circ$ ,  $34.44^\circ$ ,  $36.33^\circ$ ,  $47.56^\circ$ ,  $56.61^\circ$ ,  $62.88^\circ$ ,  $67.97^\circ$ , and  $69.11^\circ$  and  $89.86^\circ$  corresponding respectively to 100, 002, 101, 102, 110, 103, 112, 201 and 203 crystalline planes of hexagonal wurtzite ZnO (space group: P6<sub>3</sub>mc) with lattice constants  $a = b = 0.324 \text{ nm}$  and  $c = 0.521 \text{ nm}$  (JPCDS card number: 36-1451) (J. Zhou, Zhao, Wang, Zhang & Yang, 2007). The XRD pattern of the EG-ZnO nanocomposite material exhibits characteristic peaks of the individual materials with decrease in the ZnO diffraction peaks (Fig. 3.1c). This decrease has been attributed to the interaction between the EG and ZnO to produce EG-ZnO nanocomposite (B Ntsewanya et al., 2013).

**Thermogravimetric analysis.** A photoanode is expected to display good thermal stability throughout the reaction process and cycles hence, the thermal stability of the composite was studied. The TG curve of the exfoliated graphite (Fig. 3.1d) shows that about 86% of the total weight was lost. The decomposition of EG above  $800^\circ\text{C}$  is characteristic of all carbon materials. On the other hand, about 2.9% of the total weight of the bare ZnO nanopowder was lost. The weight loss of bare ZnO nanopowder may be due to the evaporation of adsorbed water on the surface of ZnO nanoparticles. The TG curve of EG-ZnO composite material reveals that about 77% of the total weight of EG-SiO<sub>x</sub>-ZnO material is reserved in comparison with EG alone. This increase in thermal stability is attributed to the presence of ZnO nanostructures in the composite.

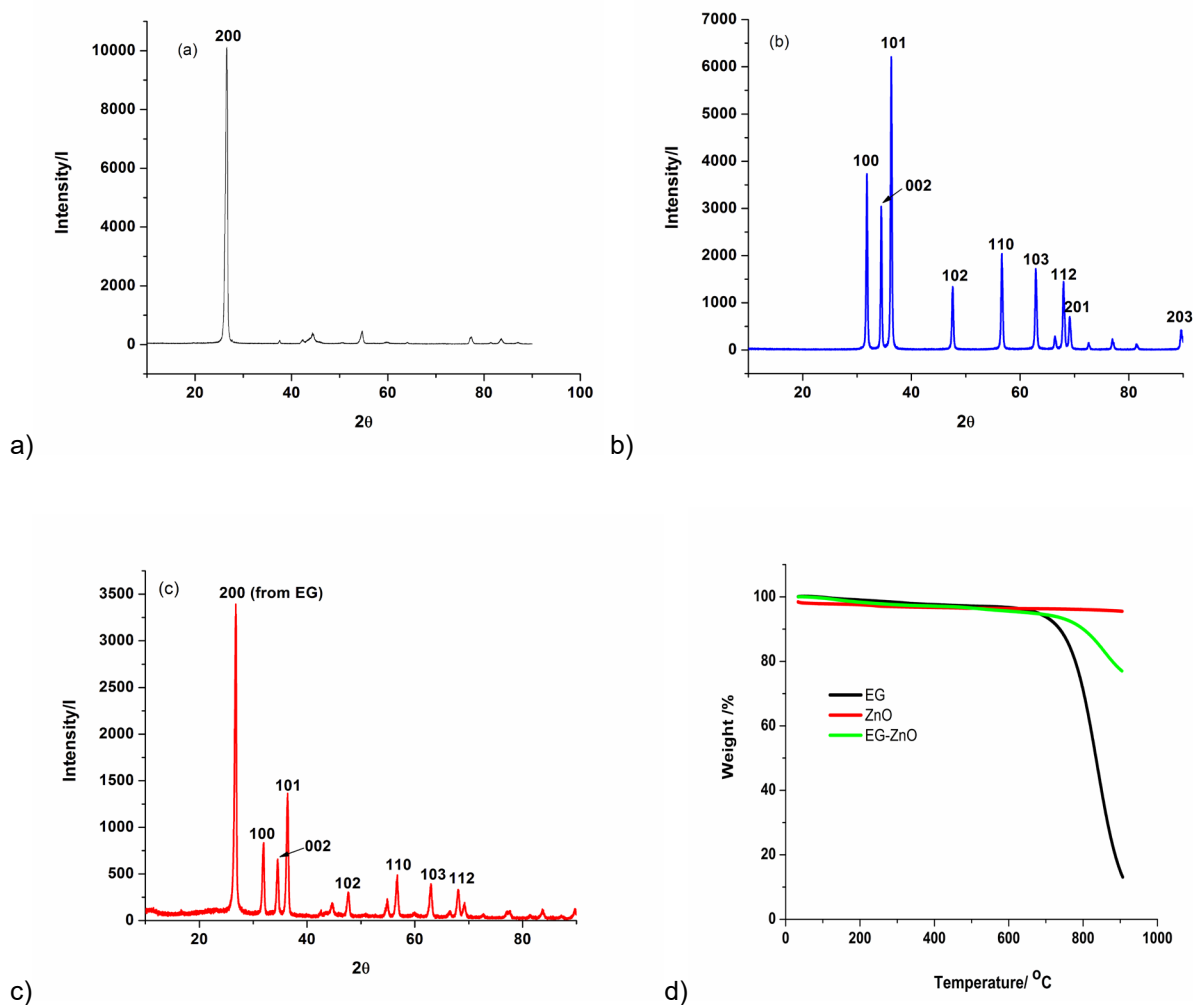


Figure 3.1. XRD patterns of (a) EG, (b) ZnO, and (c) EG-ZnO. (d) TGA thermograms of EG, ZnO and EG-SiO<sub>x</sub>-ZnO nanocomposites

### 3.3.2 Spectroscopic characterisation for Ag-ZnO-rGO

**Raman spectroscopy.** Raman spectroscopic study was carried out to determine the formation of rGO from GO. Fig 3.2a shows the Raman spectra of (i) GO and (ii) rGO. The Raman spectra display two peaks at  $\sim 1600\text{ cm}^{-1}$  and  $\sim 1350\text{ cm}^{-1}$  which correspond to the G and D bands respectively. The G band is due to the in-plane phonon vibration mode of the  $\text{sp}^2$ -bonded carbon atoms in graphene while the D band is due to defects or disorder in the hexagonal graphitic sheets resulting from the intercalation of oxygen-containing functional groups or presence of  $\text{sp}^3$  bonding (Penghua Wang, Tang, Dong, Chen & Lim, 2013). The higher intensity of the D band in relation to the G band in the rGO would give a higher D/G intensity ratio compare to the lower D/G intensity ratio in the GO. This indicates the extent of the defects in the graphitic layers (Das et al., 2014). Thus, it can be inferred that the graphene oxide was successfully reduced by the ascorbic acid, leaving few oxygen-containing functional groups that resulted in the defects in the GO.

**X-ray diffractometry.** XRD analyses were conducted on the as-synthesised rGO, ZnO and Ag-ZnO-rGO and the XRD patterns of the different materials are shown in Fig. 3.2b. In Fig. 3.2b(i), the observed diffraction peak

at  $2\theta = 26.4^\circ$  is attributed to the 002 crystal plane of rGO (JCPDS Card no. 75-1621). The diffraction peaks of hexagonal wurzite structure of ZnO (JCPDS Card no. 36-1451) were observed at  $31.8^\circ$  (100),  $34.6^\circ$  (002),  $36.4^\circ$  (101),  $47.7^\circ$  (102),  $56.7^\circ$  (110),  $63.0^\circ$  (103),  $66.5^\circ$  (200),  $68.1^\circ$  (112),  $69.2^\circ$  (201) and  $72.6^\circ$  (004). However, there are very low intensity peaks observed in Fig. 3.2b(iv) at  $38.1^\circ$  (111) and  $44.2^\circ$  (200) which indicated the presence of Ag in the as-synthesized Ag-ZnO-rGO composite (JCPDS Card no. 04-0783). Furthermore, the rGO peak at  $2\theta = 26.4^\circ$  (002) appeared broadened and lower in intensity in the as-synthesised Ag-ZnO-rGO composite. This could be due to little destruction of the crystalline structure of rGO resulting from the presence of Ag-ZnO nanostructures (Qin et al., 2015).

The crystallite size of the as-prepared sample was determined using the Debye-Scherrer's equation-  $D = K\lambda / \beta \cos\theta$ , where D is the crystal size, K is a constant (0.9),  $\lambda$  is the x-ray wavelength,  $\beta$  is the full width of half maximum (FWHM) (radian) and  $\theta$  is the diffraction angle at the maximum. The average calculated crystalline size of the ZnO was ca 21.8 nm.

**UV-Vis diffuse reflectance spectroscopy.** UV-Vis diffuse reflectance study was carried out on the samples to determine the effects of Ag and rGO on the optical properties of the as-prepared ZnO nanoparticles (Fig. 3.2c). It can be observed from the UV-Vis spectra that Ag-ZnO displayed a slightly stronger visible light absorption in comparison to ZnO. This is due to the surface plasmon resonance effects of Ag nanoparticles (Peng Wang et al., 2010; P. Wang et al., 2013). Figure 3.2c shows that there is an intense visible light absorption from  $\lambda = 430$ -800 nm for the Ag-ZnO-rGO composite resulting from the presence of rGO which serves as a photosensitizer for the visible light absorption. This enhanced visible light harvesting ability of the Ag-ZnO-rGO material can be ascribed to the synergistic effects of the SPR effect of Ag nanoparticles and enhanced visible light absorption of rGO (Qin et al., 2015). Thus, the visible light absorption capacity of the composite is a necessity for its enhanced photoelectrochemical degradation efficiency using solar energy

**Fourier transform infrared spectroscopy.** FTIR analyses were performed to investigate the functional groups present in the as-synthesised materials. The FTIR spectra of rGO and Ag-ZnO-rGO are presented in Fig. 2d. In Fig. 3.2d(i), the absorption band at  $3400\text{ cm}^{-1}$  can be attributed to O-H stretching vibration from the hydroxyl groups in rGO and the absorbed water on the surface of the rGO. The bands at  $1620\text{ cm}^{-1}$  and  $1720\text{ cm}^{-1}$  can be attributed to C=C bond stretching vibration and the stretching vibration of C=O bond of carboxyl group in rGO respectively. The broad absorption peak at  $1150\text{ cm}^{-1}$  is attributed to C-O stretching vibration which usually occurs around  $1260$ - $1000\text{ cm}^{-1}$ . In the spectra of Ag-ZnO-rGO (Fig. 3.2d(ii)), the broad peak at  $510\text{ cm}^{-1}$  accounts for Zn-O bond stretching vibration. Also, the weak peak at  $1224\text{ cm}^{-1}$  can be associated to C-O-H bending vibration ( $1440$ - $1220\text{ cm}^{-1}$ ) (Tang et al., 2014). The broad band observed at  $3400\text{ cm}^{-1}$  can be assigned to O-H stretching vibration of rGO which probably overlaps with the stretching vibration of hydroxyl groups from the absorbed water on the ZnO surface (Uddin et al., 2015). These characteristics peaks were used as indications of a successful preparation of the Ag-ZnO-rGO composite.

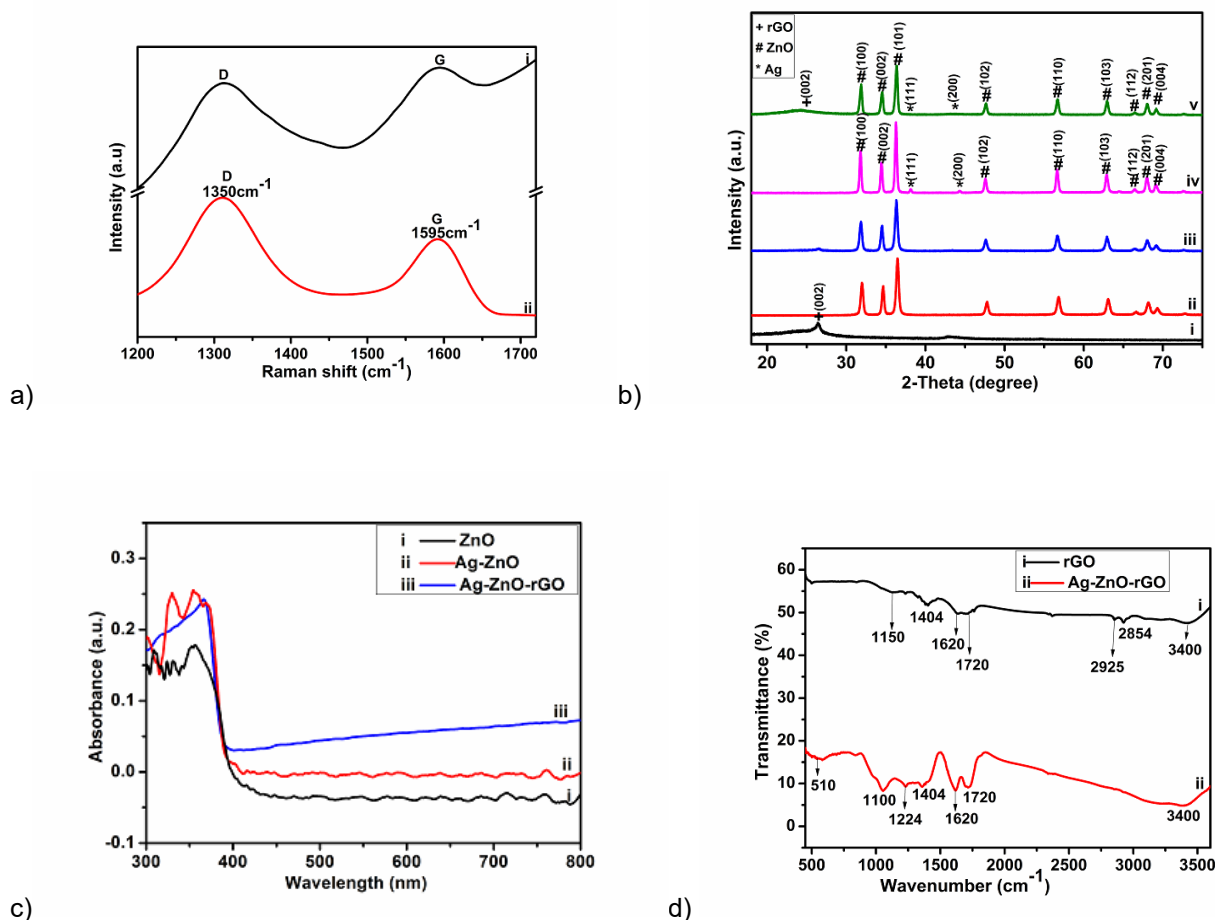


Figure 3.2. (a) Raman spectra of the prepared (i) GO and (ii) rGO; (b) XRD patterns of (i) GO, (ii) ZnO, (iii) ZnO-rGO, (iv) Ag-ZnO and (v) Ag-ZnO-rGO; (c) UV-vis diffuse reflectance spectra of (i) ZnO, (ii) Ag-ZnO, and (iii) Ag-ZnO-rGO; (d) FTIR spectra of (i) rGO and (ii) Ag-ZnO-rGO

### 3.3.3 Electron Microscopy characterisation for Ag-ZnO-rGO

The surface morphology of the as-synthesised materials was studied using scanning electron microscopy coupled with energy dispersed x-ray spectroscopy and transmission electron microscopy (Fig 3.3). Figure 3.3a displays the graphitic layers of the exfoliated graphite. The as-prepared ZnO nanoparticles are presented in Fig. 3.3b having a uniform flower-like structures. Figure 3.3c reveals the graphitic sheets of the rGO, while the presence of Ag-ZnO dispersed within and on the layers of the rGO sheets is seen in Fig 3.3d. The presence of silver in the dispersed Ag-ZnO was confirmed by EDS which also shows the presence of Zn, O and C (Fig 3.3e). The very low intensity of Ag confirmed the presence of a very minute percentage of Ag in comparison with ZnO and rGO in the Ag-ZnO-rGO nanocomposite. The TEM image (Fig 3.3(f-h)) shows the irregular sizes of the as-prepared nanocomposite ranging from 36.86 nm to 42.65 nm.

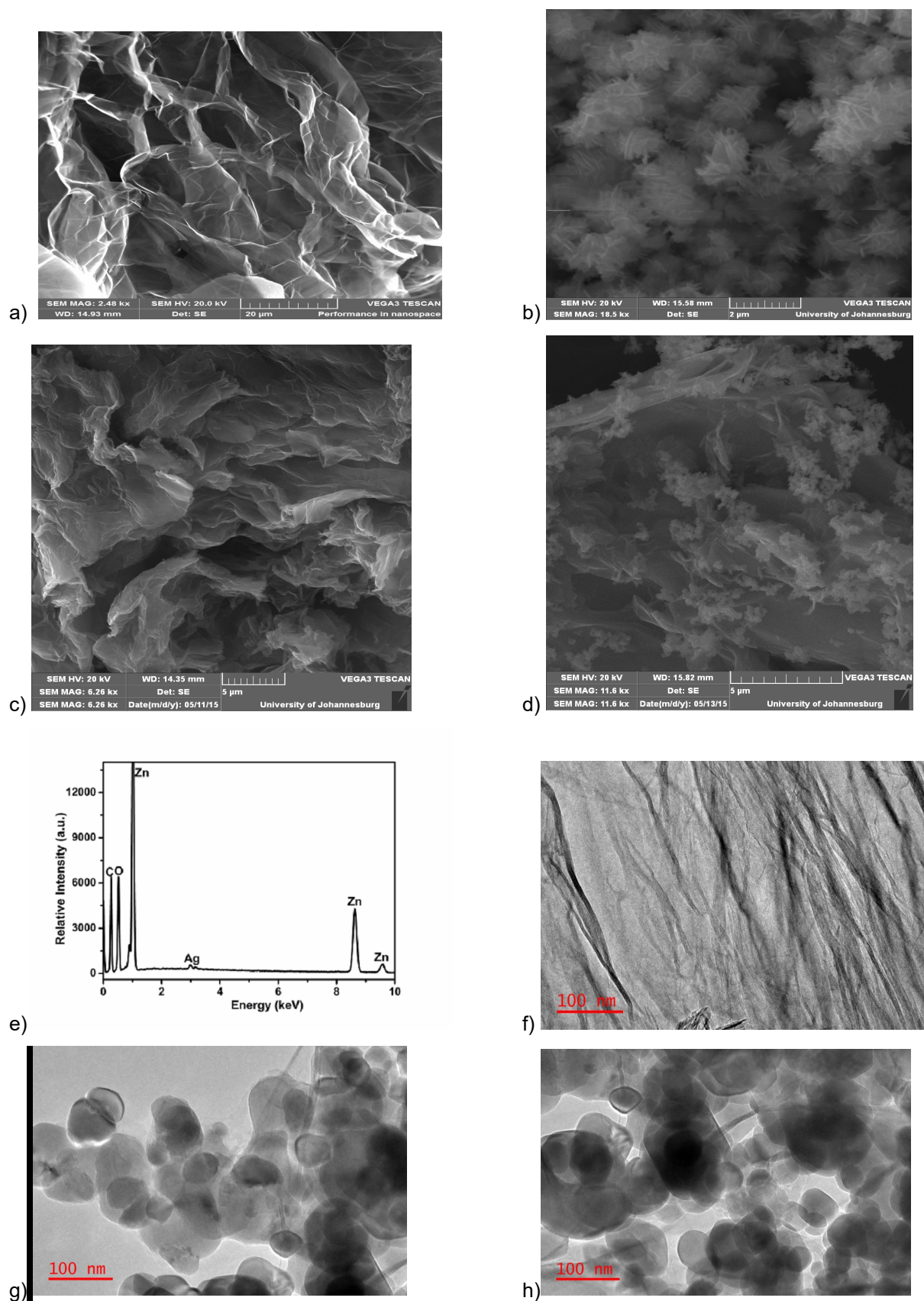


Figure 3.3. SEM images of (a) exfoliated graphite; (b) ZnO nanoparticles; (c) reduced graphene oxide (rGO); (d) the as-synthesised Ag-ZnO-rGO material. (e) EDX spectrum of the as-prepared composite. TEM images of the as-synthesised (f) rGO; (g) ZnO-rGO and (h) Ag-ZnO-rGO material.

### 3.3.4 Pore size and surface area analyses

The pore volumes and BET specific surface areas of EG, ZnO, and EG-SiOx-ZnO samples are represented in Table 3.1. The EG material exhibits a higher pore volume than ZnO nanostructure; and this allows ease of penetration of the ZnO into the EG porous matrix. The interpenetration was confirmed by the decrease in the pore volume of the EG-ZnO composite.

Table 3-1 BET data of EG, ZnO and EG-SiOx-ZnO

| Sample              | BET surface area / $m^2 g^{-1}$ | Pore volume / $cm^3 g^{-1}$ |
|---------------------|---------------------------------|-----------------------------|
| EG                  | 14.66                           | 0.06584                     |
| ZnO                 | 12.31                           | 0.05010                     |
| EG-SiOx-ZnO (MTMOS) | 9.174                           | 0.02595                     |

### 3.3.5 Spectroscopic Characterisation of EG-WO<sub>3</sub>

**Raman spectroscopy.** Raman spectroscopic technique was employed for the structural investigation of the prepared WO<sub>3</sub>-EG sample. Figure 3.4a shows the spectrum of EG before the addition of the WO<sub>3</sub> having a peak around 1598 cm<sup>-1</sup> which corresponds to the G band of graphite (inset). The G band results from the in-plane mode of vibration of the sp<sup>2</sup> bonded carbon of the prepared EG. The D band which normally results from defects was not absent, confirming the production of a highly crystalline EG. Upon the addition of the WO<sub>3</sub> to the EG, an additional peak with low intensity appeared at 1354 cm<sup>-1</sup> corresponding to the D band of EG (Kumar, Nidhi & Srivastava, 2015). This is as a result of disorder in the graphitic sheets because of the presence of sp<sup>3</sup> bonding caused by the presence of WO<sub>3</sub> (Fig. 3.4a). Additional characteristic peaks of WO<sub>3</sub> with different intensities are displayed at 806.7, 716.7, 326.8, 269.3, 131.8 and 74.3 cm<sup>-1</sup>. This indicates the interaction between the EG and the WO<sub>3</sub>. The peaks at 326.8 and 269.3 could be attributed to the bending vibrations of WO<sub>3</sub> monoclinic structure while the peaks at 131.8 and 74.3 cm<sup>-1</sup> can be allotted to the lattice modes (Grbić et al., 2014; Hunge et al., 2016). The high intensity peaks at 806.7 and 716.7 cm<sup>-1</sup> result from the stretching of O-W-O of a monoclinic structure of WO<sub>3</sub>, respectively.

**X-ray diffractometry EG-WO<sub>3</sub>.** Figure 3.4b displays the X-ray diffraction patterns of EG, WO<sub>3</sub> and WO<sub>3</sub>-EG. In Fig. 3.4b(III), the characteristic diffraction peak of EG is observed at 2 $\theta$  = 26.6° (002) crystal plane (B. Ntsemdwana et al., 2013), however, the observed feature around 37.5° is as a result of cosmic rays. The diffraction peaks of a typical monoclinic polymorph of WO<sub>3</sub> (JPCDS Card number 01-083-0950) were observed at 23.2° (002), 23.7 (020), and 24.4 (200) with high intensities. Additional peaks were obtained at 26.7 (120), 29.1 (112), 33.4 (202), 34.2 (202) and 42.1 (220) as shown in Fig. 3.4b(I). Furthermore, the increase in intensity observed at 26.7° in Fig. 3.4b(II) is due to the presence of EG in the WO<sub>3</sub> material. This indicates the co-existence of EG and WO<sub>3</sub> in the as-prepared WO<sub>3</sub>-EG material. The estimated crystallite size of the prepared material has an average value of 24.69 nm. This was estimated by employing the Debye-Scherrer's equation:

$D = K\lambda / \beta \cos\theta$ ;  $K$  is a constant (0.9),  $\lambda$  is x-ray wavelength (nm),  $\beta$  is the full width of half maximum of the diffraction peak (radian), and  $\theta$  is the angle of diffraction (radian).

**FTIR analysis EG-WO<sub>3</sub>.** The presence of functional groups and chemical interactions between the prepared WO<sub>3</sub> and EG materials were investigated using FTIR analysis. The FTIR spectra of EG and WO<sub>3</sub>-EG are presented in Fig. 3.4c(I and II). The peak at 3420-3550 cm<sup>-1</sup> could be assigned to O-H vibrations of the chemisorbed water on the EG surface. Weak bands at 2850 and 2920 cm<sup>-1</sup> could be due to C-H mode. The aromatic C=C vibration of the EG are observed at 1628 cm<sup>-1</sup> (strong) and 1468 cm<sup>-1</sup> (weak). The absorption band at 1100 cm<sup>-1</sup> could be allocated to C-O mode. Moreover, the observed small band at 1378 cm<sup>-1</sup> is linked to C-O-H bending mode which occurs around 1440-1220 cm<sup>-1</sup> (Tang et al., 2014). The additional peak at 750 and 830 cm<sup>-1</sup> (Fig. 3.4c(II)) can be assigned to W-O-W out of plane deformation mode and W-O-W bridging mode respectively (Khan, Khan & Cho, 2016). This is an indication of the presence of the WO<sub>3</sub> in the WO<sub>3</sub>-EG material.

**UV-Visible spectroscopy EG-WO<sub>3</sub>.** Optical studies were carried out on the WO<sub>3</sub> and WO<sub>3</sub>-EG samples using UV-Vis diffuse reflectance (Fig. 3.4d). It is clear that the WO<sub>3</sub>-EG portrayed a stronger photoabsorbance in the visible region relatively to WO<sub>3</sub> from  $\lambda = 430$ -800 nm. This results from the addition of the photosensitizing EG. The solar light harvesting could probably be ascribed to the formation of W-O-C bonds between the WO<sub>3</sub> and EG interfaces. Consequently, the capability of the WO<sub>3</sub>-EG to absorb visible light is of importance for its improved photoelectrochemical degradation efficiency in the presence of solar energy.

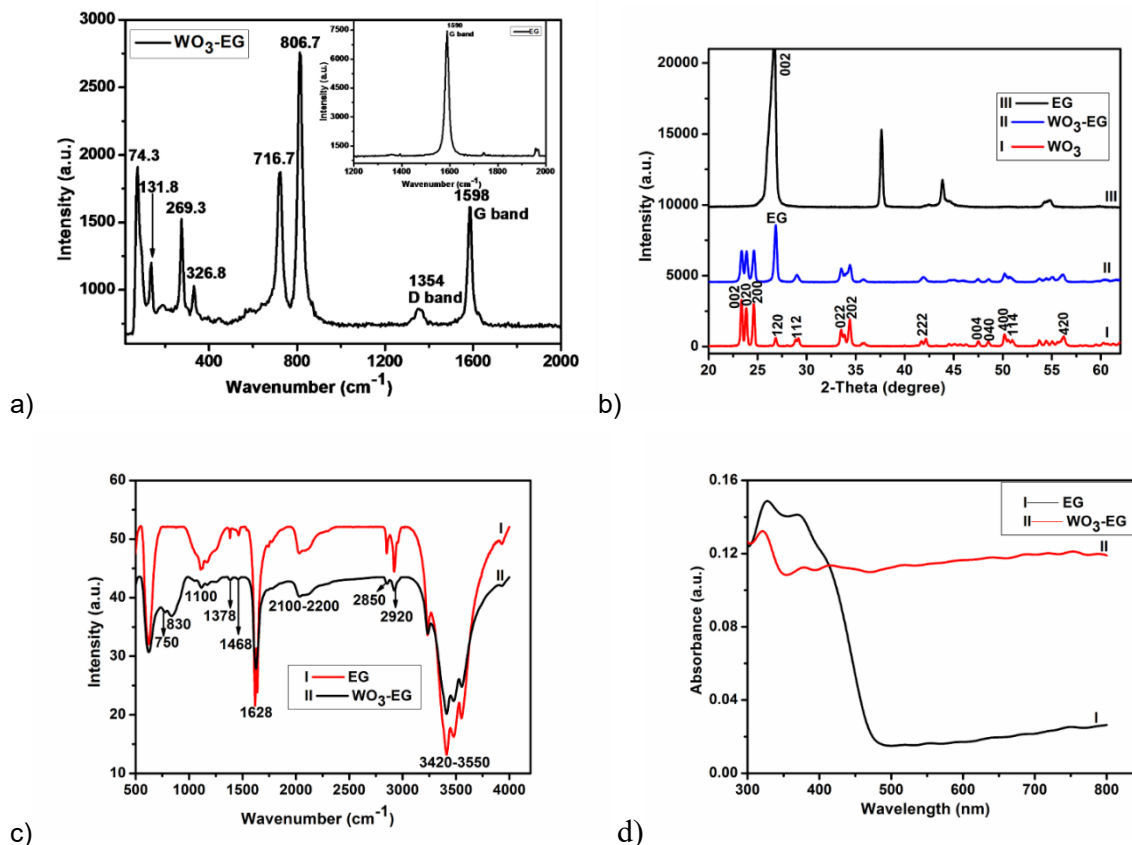


Figure 3.4. (a) Raman result of WO<sub>3</sub>-EG and EG (inset); (b) X-ray diffraction patterns of EG, (I) WO<sub>3</sub>, (II) WO<sub>3</sub>-EG and (III) EG; (c) FTIR results of (I) EG and (II) WO<sub>3</sub>-EG composite; and (d) UV-Visible diffuse reflectance spectra of (I) EG and (II) WO<sub>3</sub>-EG

### 3.3.6 Morphological studies of EG, WO<sub>3</sub> and WO<sub>3</sub>-EG

The surface morphology of EG, WO<sub>3</sub> and WO<sub>3</sub>-EG samples was investigated by SEM joined to EDX spectroscopy. Figure 3.5a depicted the WO<sub>3</sub> nanoparticles with irregular rhombic structures. The graphitic sheets of the EG can be observed with open pore-like cavities for the entrapment of the WO<sub>3</sub> nanostructures (Fig. 3.5b). In Fig. 3.5c, it can be observed that the WO<sub>3</sub> nanoparticles are well distributed in the interlayers and edges of the graphitic sheets, thus, minimising aggregation of the WO<sub>3</sub> particles. This indicated that WO<sub>3</sub> nanoparticles were uniformly dispersed in the WO<sub>3</sub>-EG composite material. The presence of W and O in the synthesised material was confirmed by EDS spectrum, indicating the presence of WO<sub>3</sub> in the EG (Fig. 3.5d).



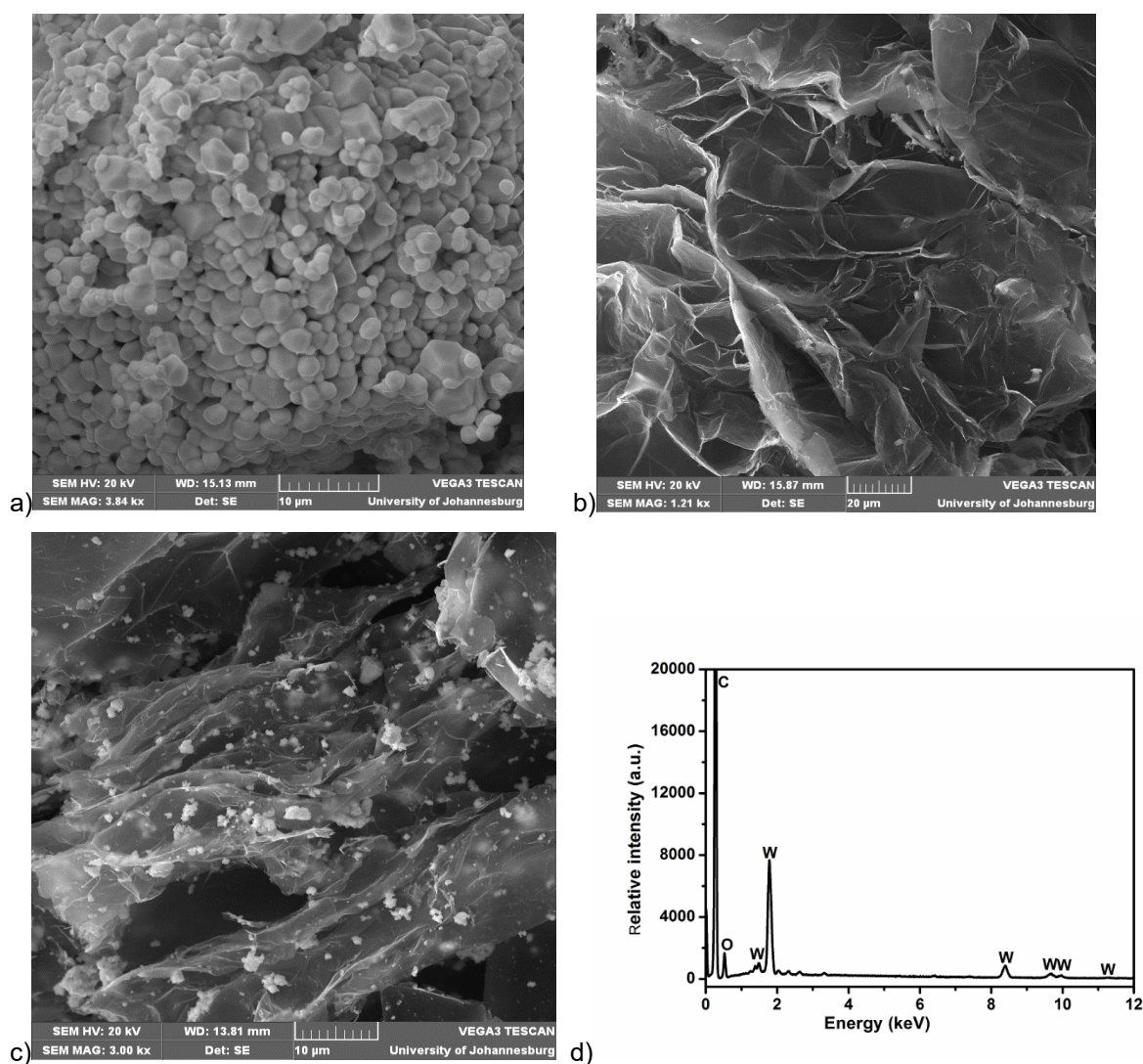


Figure 3.5. (a)  $\text{WO}_3$ , (b) EG and (c)  $\text{WO}_3$ -EG composite images of SEM. (d) EDS spectrum of  $\text{WO}_3$ -EG composite

### 3.3.7 Electrochemical and photoelectrochemical characterisation of rGO and Ag-ZnO-rGO

The electrochemical properties of rGO and Ag-ZnO-rGO electrodes were investigated in  $[\text{Fe}(\text{CN})_6]^{3-/4-}$  redox probe (Fig. 3.6a). It was observed that Ag-ZnO-rGO electrode exhibited an increase in current in relation to rGO. The faradaic current expected from the redox probe must have been impeded by the oxygen functional groups around the graphene backbone of the rGO. The enhanced current in the Ag-ZnO-rGO resulted from the Ag dopant which increased the conductivity of the electrode. For this electrode to be applicable in photoelectrochemical oxidation, the production of photocurrent when irradiated with light is expected. This property was investigated and presented in Fig 3.6b. The increase in the photocurrent response of the electrode after illumination suggests that the Ag-ZnO-rGO is photoactive and can thus be used as a photoanode (Fig 3.6b). This photoelectrochemical activity is expected to aid in the production of more hydroxyl radicals responsible for the degradation of organic pollutants in water.

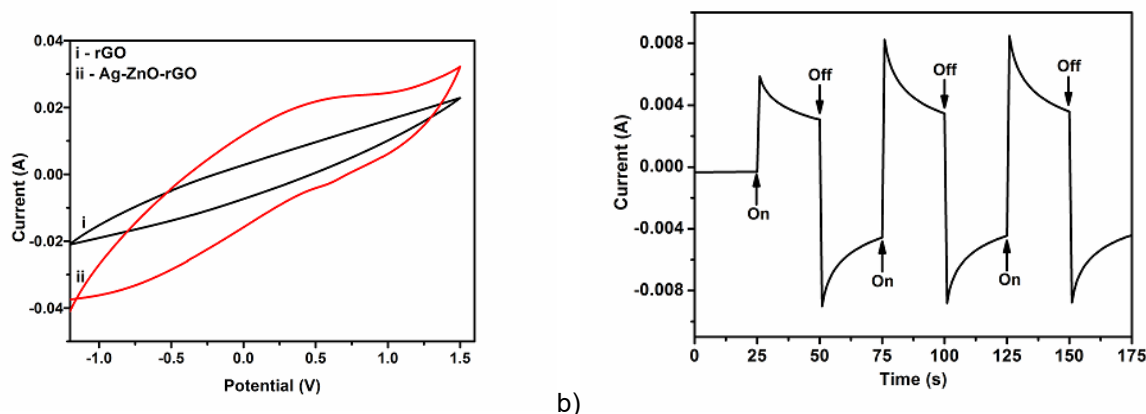


Figure 3.6. Cyclic voltammograms of (a)(i) rGO and (ii) Ag-ZnO-rGO electrodes in 5mM  $[\text{Fe}(\text{CN})_6]^{3-/4-}$  in 0.1 M KCl at 50  $\text{mVs}^{-1}$ ; (b) Photoelectrochemical response of Ag-ZnO-rGO electrode in 0.1 M  $\text{Na}_2\text{SO}_4$  in the dark (off) and under illumination (on) at 0.3 V.

### 3.3.8 Electrochemical and photoelectrochemical studies of EG and $\text{WO}_3$ -EG

Electrochemical studies were carried on the EG and  $\text{WO}_3$ -EG electrodes in a redox probe which contains a solution of 0.5 mM  $[\text{Fe}(\text{CN})_6]^{3-/4-}$  in 0.1 M KCl, and the cyclic voltammograms were recorded at a scan rate of 20  $\text{mVs}^{-1}$  (Fig. 3.7a). It was noted that the  $\text{WO}_3$ -EG electrode displayed an increment in peak current when compared to that of the EG electrode. The increased faradaic current observed from the redox probe showed that the electrode reaction rate is higher (Kusmieriek & Chrzescijanska, 2015). This is due to increase in the electrode active surface area which enhanced the conductivity of the  $\text{WO}_3$ -EG electrode due to the presence of  $\text{WO}_3$  in the EG. The electroactive surface area was calculated using the Randles-Sevcik equation,  $i_p = kn^{3/2}AD^{1/2}v^{1/2}C$ ; where  $k$  is a constant,  $2.69 \times 10^5$ ,  $n$  is the number of exchanged electrons,  $D$  is the diffusion co-efficient ( $7.6 \times 10^{-6}$  for ferrocyanide),  $C$  is the solution concentration,  $v$  is the scan rate and  $A$  is the electrode active surface area. The electrode active surface area was calculated to be 0.035 and 0.085  $\text{mm}^2$  for the EG and  $\text{WO}_3$ -EG electrodes respectively. This indicates an increment in the electrochemical active sites in the  $\text{WO}_3$ -EG electrode compared to the EG electrode (Ndlovu, Mamba, Sampath, Krause & Arotiba, 2014). A kinetic study on ferrocyanide was conducted using different scan rates. It was observed that the plot of the peak currents versus the square root of the scan rates was linear (Fig. 3b), suggesting that the process of the electrochemical kinetics of the ferrocyanide was diffusion controlled (Ndlovu et al., 2014).

Linear sweep voltammetry in the presence and absence of light, was used to test the photoelectrochemical behaviour of the electrodes in the presence of 30 ppm of orange II dye in 0.1 M  $\text{Na}_2\text{SO}_4$ . Figure 3c showed the linear voltammograms of the EG and  $\text{WO}_3$ -EG electrodes with and without irradiation. The anodic photocurrent was seen to start around 0.23 V, and the photocurrent response increased. It was observed that the intensity of the current generated by the  $\text{WO}_3$ -EG electrode under the xenon lamp irradiation was higher than that of EG electrode without the xenon lamp irradiation. This implied that there was a flow of photogenerated electrons in the  $\text{WO}_3$  under irradiation, and the electron transport was enhanced by the conductivity of the EG, indicating the photoactivity of the electrode (Monfort, Sfaelou et al., 2017b). The photocurrent response of EG and  $\text{WO}_3$ -EG was studied (Fig. 3d). The magnitude of the photogenerated current

by an electrode under irradiation is an indication of the charge separation efficiency of the photogenerated holes and electrons (N. Yang, Zhai, Wang, Chen & Jiang, 2010; Yu, Zhang & Cheng, 2014). The sharp increment in the photocurrent response of the WO<sub>3</sub>-EG electrode during irradiation suggested that the electrode is photoelectrochemically active. The photogenerated electrons from the WO<sub>3</sub> can be accepted and transported by the EG to the external circuit (Yu et al., 2014). This observation is corroborated by the results obtained from the linear sweep voltammetry. Consequently, the WO<sub>3</sub>-EG can be employed as a photoanode due to its higher photoelectrocatalytic activity for the degradation of organics in water treatment process.

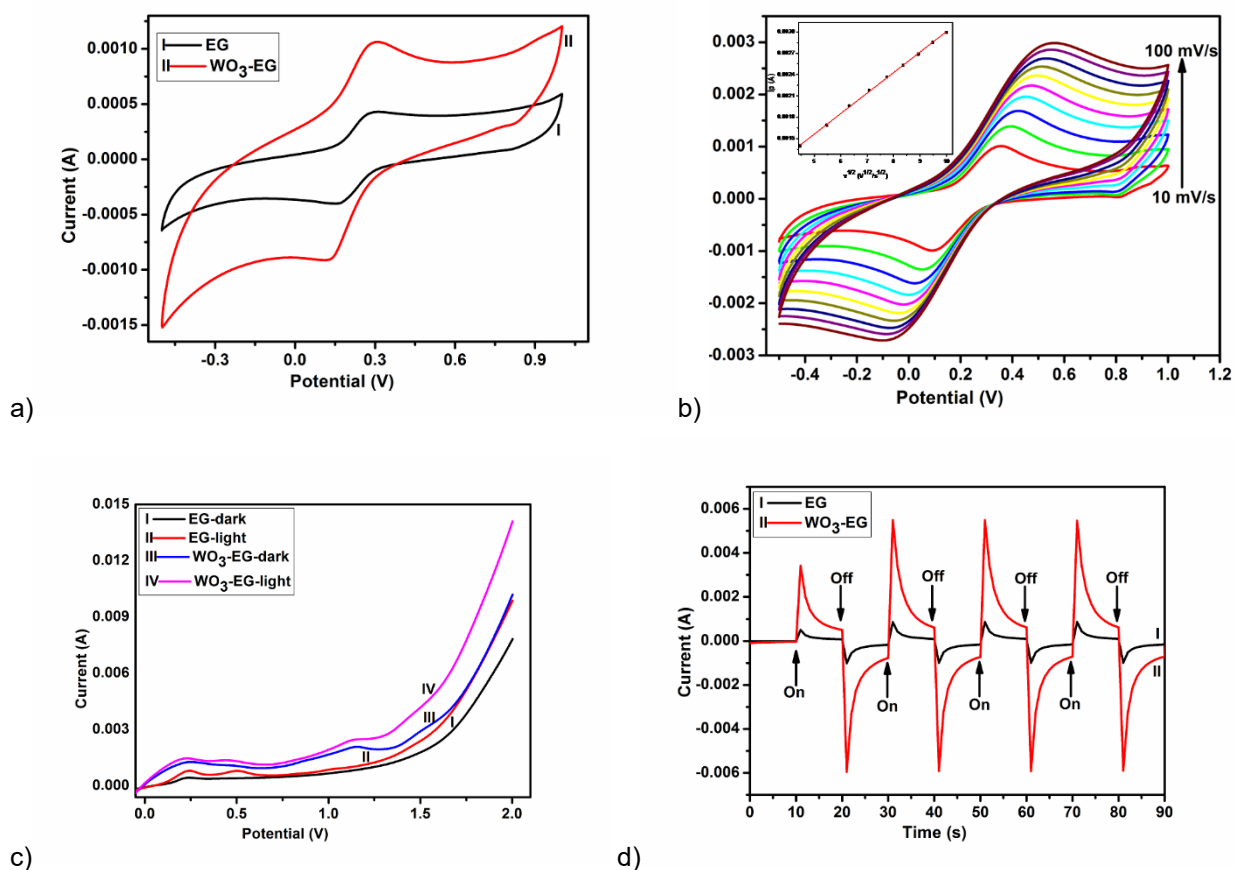


Figure 3.7. (a) CVs of (I) EG and (II) WO<sub>3</sub>-EG composite electrodes using 5mM [Fe(CN)<sub>6</sub>]<sup>3-/4-</sup> in 0.1 M KCl solution at a scan rate of 20 mVs<sup>-1</sup>; (b) CVs of WO<sub>3</sub>-EG composite electrodes at different scan rate and the plot of peak currents vs square root of scan rates. (c) Linear sweep voltammograms of EG and WO<sub>3</sub>-EG composite electrodes with (light) and without (dark) xenon lamp; and (d) responses from photocurrent of EG ((I) black) and WO<sub>3</sub>-EG ((II) red) composite electrodes in the dark (off) and under irradiation (on)

### 3.3.9 Electrochemical and Photoelectrochemical degradation of organic pollutants

In this project, different types of electrodes were prepared and used for the degradation of organic dyes, phenolics and pharmaceutical. Table 3-2 shows the different types of electrodes prepared and the pollutants degraded.

Table 3-2. Summary of photoanodes and pollutants degraded in this project

| S/N | Photoanode                                   | Organic pollutants degraded  | Reference                               |
|-----|--|------------------------------|---|
| 1   | Ag-ZnO-rGO                                   | Orange II dye                | (Umukoro et al., 2016a, 2016b)          |
| 2   | EG-WO <sub>3</sub>                           | Orange II dye, 2-nitrophenol | (Umukoro, Peleyeju et al., 2017)        |
| 3   | EG-TiO <sub>2</sub>                          | sulfamethoxazole             | (M. G. Peleyeju et al., 2017)           |
| 4   | Pd-ZnO-EG                                    | 4-nitrophenol                | (Umukoro, Madyibi et al., 2017)         |
| 5   | MoS <sub>2</sub> -SnO <sub>2</sub> /EG       | ciprofloxacin                | (Umukoro, Kumar, Ngila & Arotiba, 2018) |
| 6   | EG-BiVO <sub>4</sub> /ZnO                    | Rhodamine B dye              | (Orimolade et al., 2019)                |
| 7   | CNP/B-BiVO <sub>4</sub> /WO <sub>3</sub> /Ti | Orange II dye                | Manuscript in preparation               |

Detailed results on these photoanodes can be found in the published papers referenced. The experimental protocols for the photodegradation or photoelectrocatalytic studies are very similar in all cases. The following sections show some of the results obtained.

#### 3.3.9.1 Degradation studies of orange II dye on Ag-ZnO-rGO photoanode

**Abstract of the full study** (Umukoro et al., 2016b). In the search for novel and efficient electrochemical materials as electrodes for photoelectrochemical degradation and mineralisation of organic pollutants in water treatment, a photoanode consisting of a composite of silver (Ag), zinc oxide (ZnO) and reduced graphene oxide (rGO) was synthesized, characterised and photoelectrochemically applied in the degradation and possible mineralisation of organic pollutants in water treatment process. The ZnO and Ag-ZnO nanoparticles were synthesised by a facile one-step co-precipitation method followed by calcination at 400°C. The nanoparticles were further used to dope reduced graphene oxide by dispersion in methanol, sonicated and dried. The prepared materials were characterised using Fourier transformed infrared spectroscopy (FTIR), Raman spectroscopy, X-ray diffraction (XRD), UV-visible spectroscopy (UV-Vis), transmission electron microscopy (TEM), scanning electron microscopy (SEM) and energy dispersive X-ray spectrometry (EDX). The obtained Ag-ZnO-rGO nanocomposite was compressed and fabricated into an electrode. The photoelectrochemical applicability of the Ag-ZnO-rGO as a photoanode material was tested by the photoelectrochemical degradation of orange II dye as target organic pollutant in 0.1 M Na<sub>2</sub>SO<sub>4</sub> solution at a current density of 15 mAcm<sup>-2</sup>. The results revealed that the photoelectrochemical process was pH and current density dependent and that Ag-ZnO-rGO electrode has a higher photoelectrochemical performance (93% removal efficiency) compared to ZnO-rGO electrode (87% removal efficiency) and rGO (73% removal efficiency) respectively. The degree of mineralisation of the dye was determined using total organic carbon (TOC) which gave better removal efficiency for Ag-ZnO-rGO electrode (67.9%) in relation to ZnO-rGO (58.7%) and rGO (45.3%) electrodes, respectively.

**Photoelectrochemical degradation.** The degradation of orange II dye as a model of organic pollutant was conducted using different electrodes as photoanodes and under different degradation processes such as electrochemical oxidation, photocatalytic degradation and photoelectrochemical oxidation in which a 0.1 M Na<sub>2</sub>SO<sub>4</sub> solution was used as the supporting electrolyte (Fig. 3.8). A decline in absorbance at the  $\lambda_{\max}$  of 483 nm of the dye was used as the extent of degradation (or decolourisation) in the electrochemical cell (Fig 3.8a).

The photoelectrochemical studies of the rGO, ZnO-rGO and Ag-ZnO-rGO electrodes were carried out for the degradation of orange II dye. The percentage removal for the as-prepared rGO electrode after 210 min was 73%. The introduction of ZnO and Ag-ZnO increased the photoelectrochemical oxidation efficiency to a percentage removal of 87% (ZnO-rGO) and 93% (Ag-ZnO-rGO) respectively. This is due to the photoactive ability of ZnO and its enhancement of visible light absorption by the surface plasmon resonance effect of Ag. In addition, Ag can act as an electron sink, reducing the recombination rate of the electron-hole pairs. Consequently, there is an increase in the production of hydroxyl radicals for the degradation process.

Furthermore, Ag-ZnO-rGO electrode was investigated for the degradation of the orange II dye under electrochemical oxidation, photocatalytic degradation and photoelectrochemical oxidation processes. Electrochemical oxidation displayed lower removal efficiency when compared to the photoelectrochemical oxidation. In electrochemical oxidation, the absorbed hydroxyl groups on the electrode surface combine to form hydroxyl radicals for the oxidation of the organic pollutants and they could also combine to give oxygen molecules. Thus, evolution of oxygen can occur at the electrode as a result of the combination of these hydroxyl groups (B Ntsendwana et al., 2013). This leads to competition between the oxygen molecules and the production of hydroxyl radicals, and consequently, could results in low oxidation efficiency. However, the photogenerated electrons in photocatalytic process can be utilised in the reduction of the oxygen molecules to produce superoxide radicals and then generate more hydroxyl radicals in addition to the production of hydroxyl radicals by ZnO when irradiated with light. An enhanced performance was achieved in the photoelectrochemical process giving a removal efficiency of 93% in comparison to electrochemical oxidation (87%) and photocatalysis (47%) after 210 min. Hence, it suggests a synergistic combination of photocatalytic and electrochemical oxidation processes. Fig. 3.8(b-c) outline the plots of the normalised concentration with time using rGO, ZnO-rGO and Ag-ZnO-rGO electrodes for photoelectrochemical oxidation (Fig 3.8b); and Ag-ZnO-rGO electrode for electrochemical oxidation, photocatalysis and photoelectrochemical oxidation (Fig 3.8c).

The dependence of decolourisation on pH and current density was investigated and presented in Fig. 3.8(d-e). The removal efficiency decreased as the pH of the solution was increased from pH 5 to 10 as shown in Fig.3.8d. The high percentage removal at pH 5 is due to the electrostatic interactions between the negatively-charged orange II dye (pH 2-9.6) (Abramian & El-Rassy, 2009) and the positively-charged surface of the electrode containing ZnO ( $\text{pH} < \text{pH}_{\text{pzc}} = 6.9-9.8$ ) (Chamjangali & Boroumand, 2013). Studies at extreme acidic pH of 1-3 and basic pH of 11-14 were not carried out because of the application at a higher scale where it may not be cost effective and realistic to do pH adjustment. The effect of current density is shown in Fig. 3.8d. The removal efficiency increased as the current density was increased. This is as a result of the production of more hydroxyl radicals as the current was increasing. However, it was observed that the electrode began to leach at current densities higher than  $15 \text{ mAcm}^{-2}$ . Hence, a current density of  $15 \text{ mAcm}^{-2}$  was chosen as the optimal current density. The ability of the Ag-ZnO-rGO photoanode to withstand a current density of  $15 \text{ mAcm}^{-2}$  is an indication that the electrode possesses high stability to an extent and hence could be utilised in practical applications.

The degree of mineralisation of the dye was determined using total organic carbon (TOC) which gave a better removal for Ag-ZnO-rGO electrode (67.9%) in relation to ZnO-rGO (58.7%) and rGO (45.3%) electrodes respectively.

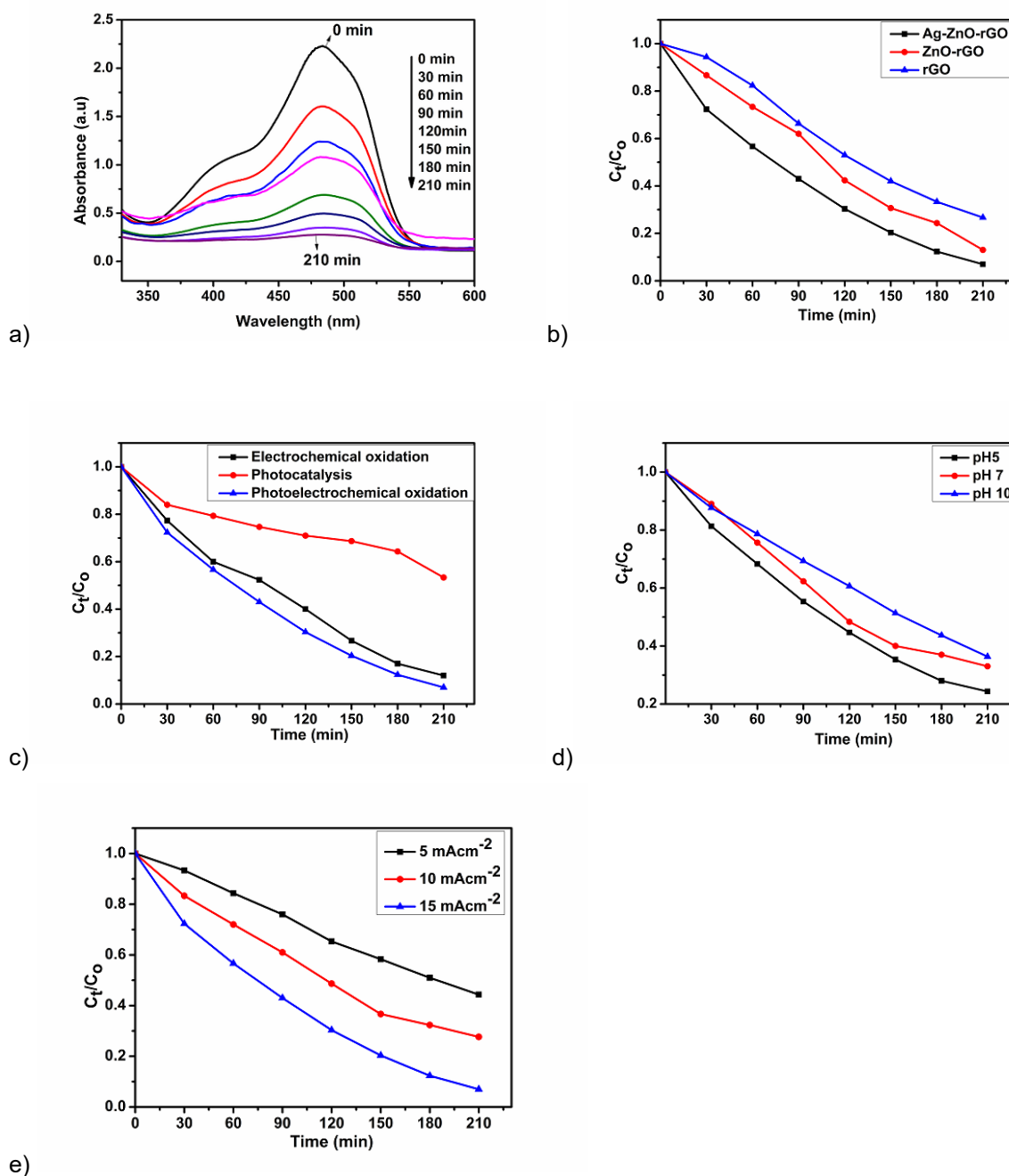
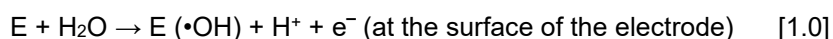


Figure 3.8. (a) UV-Vis spectra for the degradation of orange II dye at Ag-ZnO-rGO electrode using photoelectrochemical oxidation; Normalised decay plots of the photoelectrochemical degradation of orange II dye (b) at rGO, ZnO-rGO and Ag-ZnO-rGO electrodes; (c) using photoelectrochemical oxidation, electrochemical oxidation and photocatalysis at Ag-ZnO-rGO electrode; and effects of (d) pH and (e) current density on the photoelectrochemical degradation of orange II dye.

**Degradation kinetics.** The kinetics of the degradation of the orange II dye was studied using the pseudo-first order kinetics equation  $\ln C_0/C_t = k_{app}t$ , where  $C_0$  is the initial concentration of the dye and  $C_t$  is the concentration at time,  $t$ ,  $t$  is the reaction time, and  $k$  is the apparent reaction rate constant. This equation is usually applied

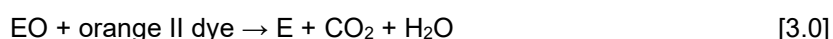
for the kinetics of electrochemical degradation of organics (B Ntsendwana et al., 2013; Jing Zhang, Li, Feng, Chen & Li, 2006). The data obtained for the photoelectrochemical degradation processes using the as-prepared electrodes were fitted into the pseudo-first order kinetics and linear plots of  $\ln C_0 / C_t$  against  $t$  were obtained which suggested that the degradation kinetics is pseudo-first order kinetics. The  $k_{app}$  values for the as-prepared electrodes are;  $12.26 \times 10^{-3} \text{ min}^{-1}$  (Ag-ZnO-rGO)  $> 9.38 \times 10^{-3} \text{ min}^{-1}$  (ZnO-rGO)  $> 6.63 \times 10^{-3} \text{ min}^{-1}$  (rGO) with correlation coefficients ( $R^2$ ) of 0.9750, 0.9479 and 0.9787 respectively. Fig. 3.9a shows the kinetics of the photoelectrochemical degradation of orange II dye in 0.1 M  $\text{Na}_2\text{SO}_4$  at pH 5 and  $15 \text{ mAcm}^{-2}$ .

A plausible mechanism (Fig 3.9b) and the necessary reactions involved in the production of the  $\bullet\text{OH}$  radicals for the dye degradation are shown in Eqns [1.0]-[13.0].

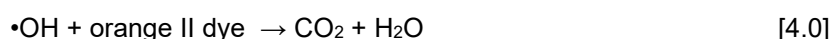


Where E is the electrode

The nature of material used for the fabrication of the electrode determines whether the activity of the electrode. An active electrode will interact strongly with the generated hydroxyl radical to produce a higher oxide referred to as EO which then oxidises the pollutant, orange II dye.



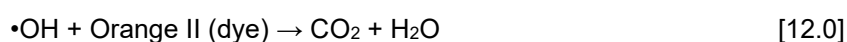
Or



In addition, the evolution of oxygen as a result of the decomposition of the higher oxide may compete with the oxidation of the organic pollutant, thereby, leading to incomplete oxidation of the organic pollutant (B Ntsendwana et al., 2013; Umukoro et al., 2016b).



Upon the absorption of light;



The photogenerated electrons can be driven from the conduction band of ZnO to the Ag and rGO by the application of a bias potential or electrical energy, and thereby reducing the recombination of the charges within the ZnO (A. Zhu, Zhao, Li & Shi, 2013). The holes react with water molecules to form a proton and hydroxyl radical ( $\bullet\text{OH}$ ) while the oxygen molecules released in the wastewater react with the photogenerated electrons to form a superoxide oxygen radical ( $\bullet\text{O}_2^-$ ). The  $\bullet\text{O}_2^-$  reacts with a proton to form hydroperoxide radical ( $\text{H}_2\text{O}_2\bullet$ ) which can react with water to give hydrogen peroxide which in turn generates hydroxyl radicals.



Consequently, these radicals and the holes are involved in reactions with the orange II dye molecules repeatedly to degrade and possibly mineralised them into less toxic substances such as  $\text{CO}_2$  and  $\text{H}_2\text{O}$  (Hua et al., 2013).

The improved photoelectrochemical performance of the Ag-ZnO-rGO can be attributed to: (i) the surface plasmon resonance of Ag (P. Wang et al., 2013), (ii) reduced electron-hole pair recombination by enhanced interfacial electron transport between Ag and ZnO (Ma et al., 2014; Sarkar, Ghosh, Mukherjee & Chattopadhyay, 2012), (iii) the outstanding electron mobility/conductivity of reduced graphene oxide which enhanced the transfer of photogenerated electrons and holes from ZnO to the graphene, thus, minimizing the rate of recombination of the electron-hole pairs (Fenghua Chen et al., 2014).

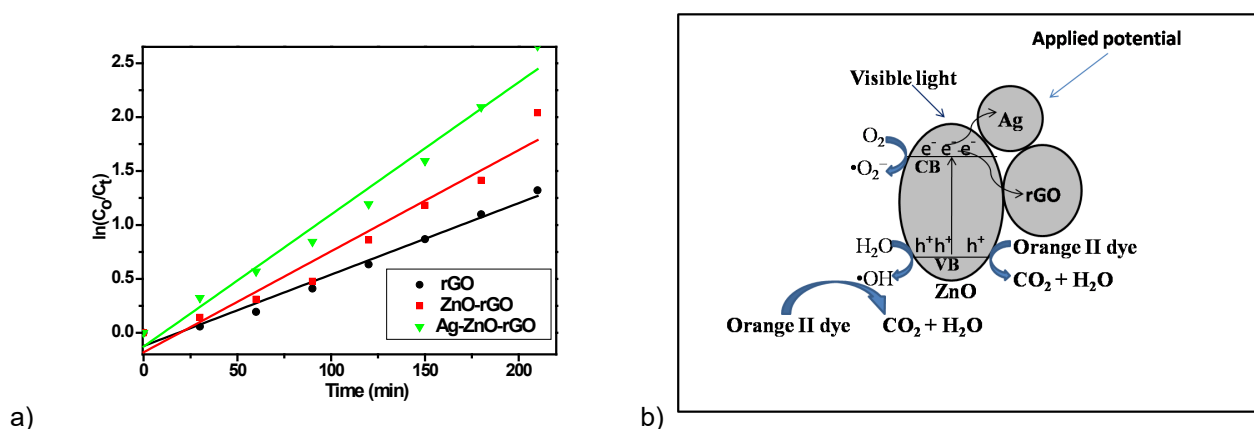


Figure 3.9. (a) Kinetic plots of photoelectrochemical degradation of orange II dye at pH 5 and  $15 \text{ mAcm}^{-2}$  using rGO, ZnO-rGO and Ag-ZnO-rGO electrodes; (b) photoelectrochemical set-up for the degradation of orange II dye (c) a proposed mechanism for the photoelectrochemical activity of the as-prepared Ag-ZnO-rGO for the degradation of orange II dye.

**Sub-Conclusion.** A novel photoanode of Ag-ZnO-GO nanocomposite was synthesised and characterised using various spectroscopic, electron microscopic and electrochemical techniques. The photoanode was used in the photoelectrochemical degradation of orange II dye with a percentage removal of 93%. The presence of Ag-ZnO improved the photoelectrochemical performance of the photoanode due to the production of hydroxyl radicals upon the irradiation of ZnO by visible light, and the surface plasmon resonance effect of Ag. The degradation kinetics followed a pseudo first order reaction. Hence Ag-ZnO-rGO photoanode can be employed in the photoelectrochemical degradation of dyes in water treatment process.

### 3.3.9.2 Degradation studies of 2 nitro phenol and orange II dye on EG- $\text{WO}_3$ photoanode

**Abstract of the full study** (Umukoro, Peleyeju et al., 2017). There is an ongoing quest for cheap, efficient and novel electrochemical materials for the construction of electrodes used for electrochemical and photo-assisted electrochemical degradation (probably, mineralisation) of organics in wastewater treatment. In this regard, a composite of tungsten trioxide ( $\text{WO}_3$ ) and exfoliated graphite (EG) was synthesised, characterised, fabricated into an electrode and employed in the electrochemical and photo-assisted electrochemical degradation of organics in water treatment.  $\text{WO}_3$  nanoparticles were synthesised using a modified simple chemical method followed by calcinations at  $600^\circ\text{C}$ . Then the composite was prepared by a wet chemical method after the exfoliation of the graphite. The  $\text{WO}_3$ -EG nanocomposite was characterised using cyclic



voltammetry, linear sweep voltammetry, X-ray diffractometry, Raman and Fourier transformed infrared spectroscopy, and scanning electron microscopy connected to energy dispersive X-ray spectrometry. The electrochemical and photo-assisted electrochemical applicability of the  $\text{WO}_3$ -EG as photo-electrode material was investigated by the degradation of 2-nitrophenol and orange II dye as model organic pollutants in a 0.1 M  $\text{Na}_2\text{SO}_4$  solution, using a  $10 \text{ mAcm}^{-2}$  current density. Decolourisation and removal of the dye and 2-nitrophenol were monitored using a UV-Visible spectrophotometer and the mineralisation level was investigated using a TOC analyser. The EG- $\text{WO}_3$  nanocomposite electrode gave a higher degree by 28% 2-nitrophenol and 24% orange II dye of decolourisation (82% for 2-nitrophenol and 95% for orange II dye) and by 34.4% 2-nitrophenol and 18% orange II dye of mineralisation (69% for 2-nitrophenol and 67% for orange II dye) in comparison to the EG electrode. Furthermore, the presence of  $\text{WO}_3$  rendered the electrode a good photoanode owing to its higher degradation efficiency.

**Photoelectrochemical degradation.** The performance of the EG and  $\text{WO}_3$ -EG electrodes were tested on the degradation of 2-nitrophenol. It was found that  $\text{WO}_3$ -EG electrode showed a higher removal efficiency in the electrochemical degradation of 2-nitrophenol (52%) in comparison with the EG electrode (39%). Furthermore,  $\text{WO}_3$ -EG electrode gave a better removal in the photo-assisted electrochemical degradation process (82%) than the EG electrode (54%) as seen in Fig. 4a. This can be construed to result from the low electron transfer resistance of the  $\text{WO}_3$ -EG composite electrode which could enhance its charge separation efficiency (Yu et al., 2014). As shown in Fig. 4b, the  $\text{WO}_3$ -EG composite electrode showed an enhanced removal performance in the photo-assisted electrochemical degradation process than the electrochemical degradation. This is attributed to the photosensitive nature of  $\text{WO}_3$ , leading to a flow of photogenerated holes and electrons upon irradiation, and the electron transport was enhanced due to the presence of EG that is very conductive. This argument can be buttressed with the results from the LSV and photocurrent responses of the electrodes. Thus, it suggests there is a synergistic combination of EG and  $\text{WO}_3$  in the composite electrode which aided the degradation process.

The degradation of 2 nitrophenols was found to be possible in the pH range of 3 to 8 demonstrating the robustness of this system.

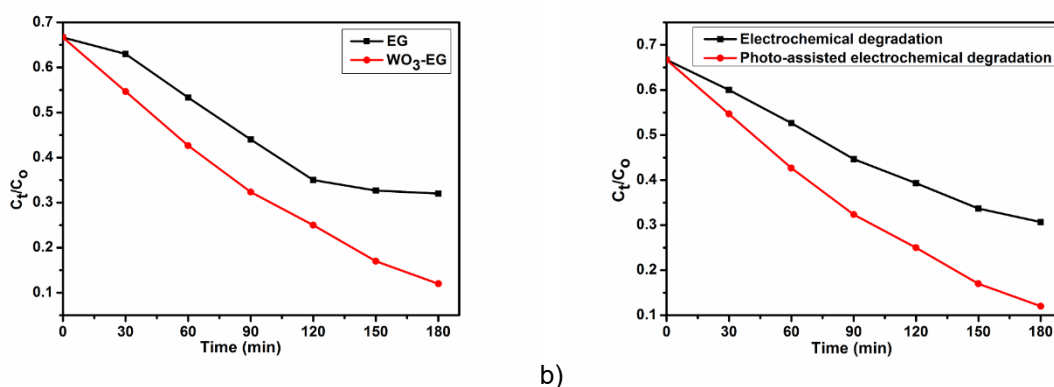


Figure 3.10. Normalised concentration decay versus time plots of the photo-assisted electrochemical degradation of 2-nitrophenol (a) at EG and  $\text{WO}_3$ -EG composite electrodes, (b) under electrochemical and photo-assisted electrochemical degradation processes

Table 3-3. Summary of results for degradation studies with WO<sub>3</sub>-EG photoanode

| Photoanode          | Pollutant     | Key results   |
|---------------------|---------------|---|
| WO <sub>3</sub> -EG | 2 nitrophenol | Time of degradation = 180 min<br>Electrochemical degradation: EG (39%); WO <sub>3</sub> -EG (52%)<br>Photoelectrochemical degradation: EG (54%); WO <sub>3</sub> -EG (82%)<br>pH range: 3-8<br>Optimum Current density: 10 mAcm <sup>-2</sup><br>Total Organic Carbon removal: Electrochemical = 34.6%;<br>Photoelectrochemical degradation = 69%<br><br>Kinetics (k <sub>app</sub> ): Electrochemical degradation = $4.5 \times 10^{-3} \text{ min}^{-1}$ ;<br>Photoelectrochemical degradation = $9.54 \times 10^{-3} \text{ min}^{-1}$ . |
|                     | Orange II dye | Time of degradation = 120 min<br>Electrochemical degradation: WO <sub>3</sub> -EG (71%)<br>Photoelectrochemical degradation: WO <sub>3</sub> -EG (95%)<br>pH optimum: 5.5<br>Optimum Current density: 10 mAcm <sup>-2</sup><br>Total Organic Carbon removal: Electrochemical = 49%;<br>Photoelectrochemical degradation = 67%<br><br>Kinetics (k <sub>app</sub> ): Electrochemical degradation = $6.89 \times 10^{-3} \text{ min}^{-1}$ ;<br>Photoelectrochemical degradation = $16.87 \times 10^{-3} \text{ min}^{-1}$ .                   |

**Sub Conclusion.** In this work, WO<sub>3</sub>-EG nanocomposite electrode was fabricated and employed successfully for the electrochemical and photo-assisted electrochemical degradation of 2-nitrophenol and orange II dye in water treatment. The WO<sub>3</sub> nanoparticles with average sizes of 24.69 nm were uniformly dispersed on the exfoliated graphite sheets. The removal efficiencies were 82% and 95% for the photo-assisted electrochemical degradation of 2-nitrophenol and orange II dye after 180 and 120 minutes respectively. The utilisation of a low current density (10 mAcm<sup>-2</sup>) by the WO<sub>3</sub>-EG composite electrode for the photo-assisted electrochemical degradation process is an indication of energy cost effectiveness. The synergy between WO<sub>3</sub> and EG in the WO<sub>3</sub>-EG composite is obvious from the improved photo-assisted electrochemical performance portrayed by WO<sub>3</sub>-EG electrode compared to its electrochemical performance. Thus, WO<sub>3</sub>-EG composite electrode renders itself a good photoanode in water treatment process due to its higher degradation efficiency.

### 3.3.9.3 Degradation of sulfamethoxazole (SMX) at EG and TiO<sub>2</sub>-EG electrodes

**Abstract of the full study** (Moses G Peleyeju et al., 2017). Sulfamethoxazole is an antibacterial agent which is commonly prescribed for the treatment of infections in man and animals. The detection of this drug in the aqueous environment has raised considerable health concerns. Herein, we report the photoelectrocatalytic degradation of sulfamethoxazole at a TiO<sub>2</sub>-exfoliated graphite (TiO<sub>2</sub>-EG) anode. The TiO<sub>2</sub>-EG nanocomposite, synthesised by sol-gel and microwave methods, was characterised by XRD, Raman and FTIR spectroscopies, SEM and TEM. The cyclic voltammograms of the fabricated electrodes were obtained in [Fe(CN)<sub>6</sub>]<sup>3-</sup> redox probe. Concentration abatement of the antibiotic was monitored on UV-Vis spectrophotometer and the possible intermediates were investigated using LCMS. After 6 h of the photoelectrocatalytic process, Almost 100% of

the drug has been degraded and a 90% COD decay was achieved. The photoelectrocatalytic degradation of sulfamethoxazole entailed  $\gamma$ -,  $\beta$ -,  $\delta$ - and  $\varepsilon$ - cleavages, hydroxylation and rings opening. The outcome of this study shows that the EG-TiO<sub>2</sub> anode can be applied for the photoelectrocatalytic remediation of water contaminated by pharmaceuticals.

**Photoelectrochemical degradation.** Oxidation of the analyte was monitored on UV-Vis spectrophotometer at its wavelength of maximum absorption ( $\lambda_{\text{max}} = 257 \text{ nm}$ ). In both electrochemical and photoelectrochemical processes at the TiO<sub>2</sub>-EG electrode, there was a gradual but very significant reduction (with time) in the absorbance of the antibiotic at the  $\lambda_{\text{max}}$  (Fig. 3.11a). This confirmed its degradation in the processes. However, a much higher degradation efficiency was obtained in the photo-assisted process (Fig. 3.11b). It is also noteworthy that the composite electrode exhibited a higher removal efficiency of the analyte than the pristine electrode in the electrochemical process (Fig. 3.11c). The improved degradation obtained in the photoelectrochemical process at the TiO<sub>2</sub> based electrode can be attributed to the photocatalytic behaviour of the semiconductor and the combined effect of electrical energy and solar energy which are beneficial for generating the hydroxyl radicals required to destroy the pollutant. Upon irradiation with light, the photo-generated holes in TiO<sub>2</sub> reacts with water to produce hydroxyl radicals, this powerful oxidant attacks and degrades the pollutant molecules until they are mineralised. Similarly, the holes also act as oxidant, attacking the organic specie until it is completely broken down. Furthermore, when the applied potential is sufficiently high, oxidation of water on the surface of the anode to form the hydroxyl radicals takes place. The enhanced performance of EG-TiO<sub>2</sub> compared to EG in the electrochemical process can be related to the higher electro-active surface area of the EG-TiO<sub>2</sub> which provides for greater number of sites for the oxidation of water to generate the oxidant. In addition, since direct electron transfer from the contaminant to the anode often occurs simultaneously with the indirect oxidation (Donaghue & Chaplin, 2013; Zhi, Wang, Nakashima, Rao & Fujishima, 2003), a larger electro-active surface area favours the oxidation of SMX at the anode. This observation is in agreement with the results of the cyclic voltammetry experiments in which higher current was obtained at the composite electrode.

The influence of current density on the degradation process was investigated. Oxidation of the analyte was achieved at the initial current density of 7 mAcm<sup>-2</sup>. There was however improvement in the process when the value was increased to 10 mAcm<sup>-2</sup>. Further increase to 13 mAcm<sup>-2</sup> did not lead to appreciable increase in the degradation efficiency (Fig. 3.11d). This trend suggests that the oxidation of SMX is mainly achieved by holes and hydroxyl radicals in the photoelectrochemical process. It is also believed that the anodic potential at 10 mAcm<sup>-2</sup> is optimal to prevent recombination of photogenerated charges and that further increase in potential is unutilised.

The effect of pH of the bulk solution on the degradation of SMX was studied. It can be observed that the rate of oxidation is higher at acidic pH (Fig. 3.11e), with the rate at pH 3 being slightly higher than the rate at pH 6. The  $\text{pK}_{\text{a}1}$  and  $\text{pK}_{\text{a}2}$  values of SMX are 1.7 and 5.6 respectively (H. Chen, Gao, Li & Ma, 2011). Below and above these values SMX is either positively or negatively charged. The proportion of cationic or anionic form of SMX present in a solution at a time depends on the pH of the solution. At pH 3, SMX molecules are expected to be in neutral form and since the degradation efficiency at this pH is higher than at the other two pH values, it can be said that the degradation of the analyte in this process is favoured when the molecules are uncharged. The

difference between the rates at pH 3 and pH 6 is not very large, thus it can be asserted that there is still a considerable amount of the neutral molecules at pH 6. Furthermore, although the degradation of SMX at pH 6.3 is a little slower, the pH of the electrolytic solution can still be maintained at 6.3 since it is milder.

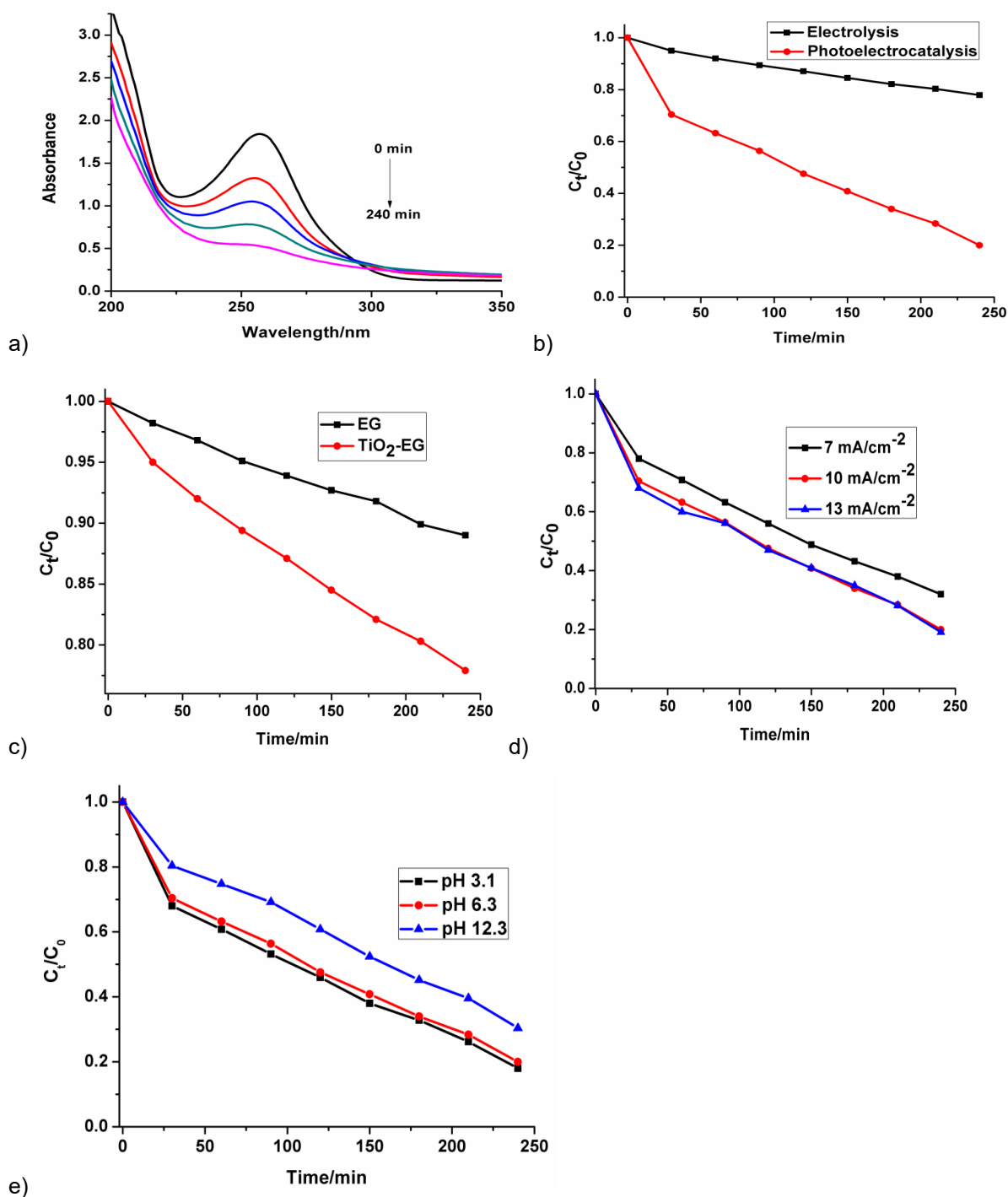


Figure 3.11. a) UV-Vis spectra of oxidised SMX solution and normalised plots of concentration abatement for b) electrochemical and photoelectrocatalytic degradation of SMX at TiO<sub>2</sub>-EG photoelectrode c) electrochemical degradation of SMX at EG and TiO<sub>2</sub>-EG anodes (experiments carried out at pH 6.3,  $j = 10 \text{ mAcm}^{-2}$ ,  $[\text{SMX}]_0 = 25 \text{ mgL}^{-1}$ , supporting electrolyte =  $\text{Na}_2\text{SO}_4$ ) d) current-dependence of SMX degradation e) effect of bulk solution pH on SMX degradation.

**Kinetics of SMX degradation, COD decay and current efficiency at TiO<sub>2</sub>-EG photoanode.** An efficient wastewater treatment technique is expected to lead to a significant reduction in the chemical oxygen demand (COD) of the water at a reasonable energy input. The removal of COD in this investigation was calculated using the relations:

$$\text{COD decay (\%)} = (\text{COD}_0 - \text{COD}_t) / \text{COD}_0 * 100\%$$

where COD<sub>0</sub> and COD<sub>t</sub> are the values (in mgL<sup>-1</sup>) of chemical oxygen demand at time, t = 0 and t = t respectively. After 6 hr of electrolysis and light irradiation at the optimum conditions, a 90% COD removal was obtained at the photoanode.

Using the COD approach, the current efficiency for the degradation of SMX was calculated using the following equation (M. Zhou, Dai, Lei, Ma & Wang, 2005):

$$\text{Total Current Efficiency (TCE)} = FV. (\text{COD}_0 - \text{COD}_t) / 8I\Delta t$$

where COD<sub>0</sub> and COD<sub>t</sub> are the COD (in gL<sup>-1</sup>) at time t = 0 and t = t, F is the Faraday constant (96487 Cmol<sup>-1</sup>), V is the volume of the electrolytic solution (in Litre), I is the current (A) and t is the electrolysis time (s). The TCE calculated for the degradation of SMX at optimum conditions was 0.674. This value indicates that a fairly high proportion of the electrical energy applied was utilised for the decay of the contaminant.

**Identification of intermediate products during the degradation of SMX.** LCMS analysis of standard sample and aliquots of degraded SMX solution were carried out. The chromatograms obtained are in Fig. 3.12 The major aromatic intermediates identified are m/z = 94, 157, 172. These species can result from the γ-, β-, δ- and ε- cleavages of the sulfamethoxazole molecules (de Amorim, Romualdo & Andrade, 2013). The peak at m/z = 94 can be considered as protonated aniline, it has been reported in a number of studies dealing with oxidation of SMX by hydroxyl radicals (de Amorim et al., 2013; Hussain, Gul, Steter, Miwa & Motheo, 2015; G. Liu et al., 2017). It can be thought to be formed by the attack of hydroxyl radicals on sulfonated moiety, leading to release of SO<sub>4</sub><sup>2-</sup> (G. Liu et al., 2017). The formation of a product having m/z = 157 has been attributed to the cleavage of the S-N bond in the parent molecule (W. Zhu, Sun, Goei & Zhou, 2017), and the m/z = 172 may be a sulfanilamide or ionic form of sulfanilic acid resulting from ε- cleavage (de Amorim et al., 2013; Hu, Flanders, Miller & Strathmann, 2007). The peaks at m/z = 270 and 286 have been indicated to result from the mono- and di-hydroxylated products of SMX (Ioannidou et al., 2017; Radjenovic & Petrovic, 2017). It can therefore be reasonably suggested that the photoelectrocatalytic oxidation of SMX is by cleavage of the S-N bond and hydroxylation and opening of ring systems in the molecule. A schematic representation of the degradation route of SMX is presented in Fig. 3.12D.

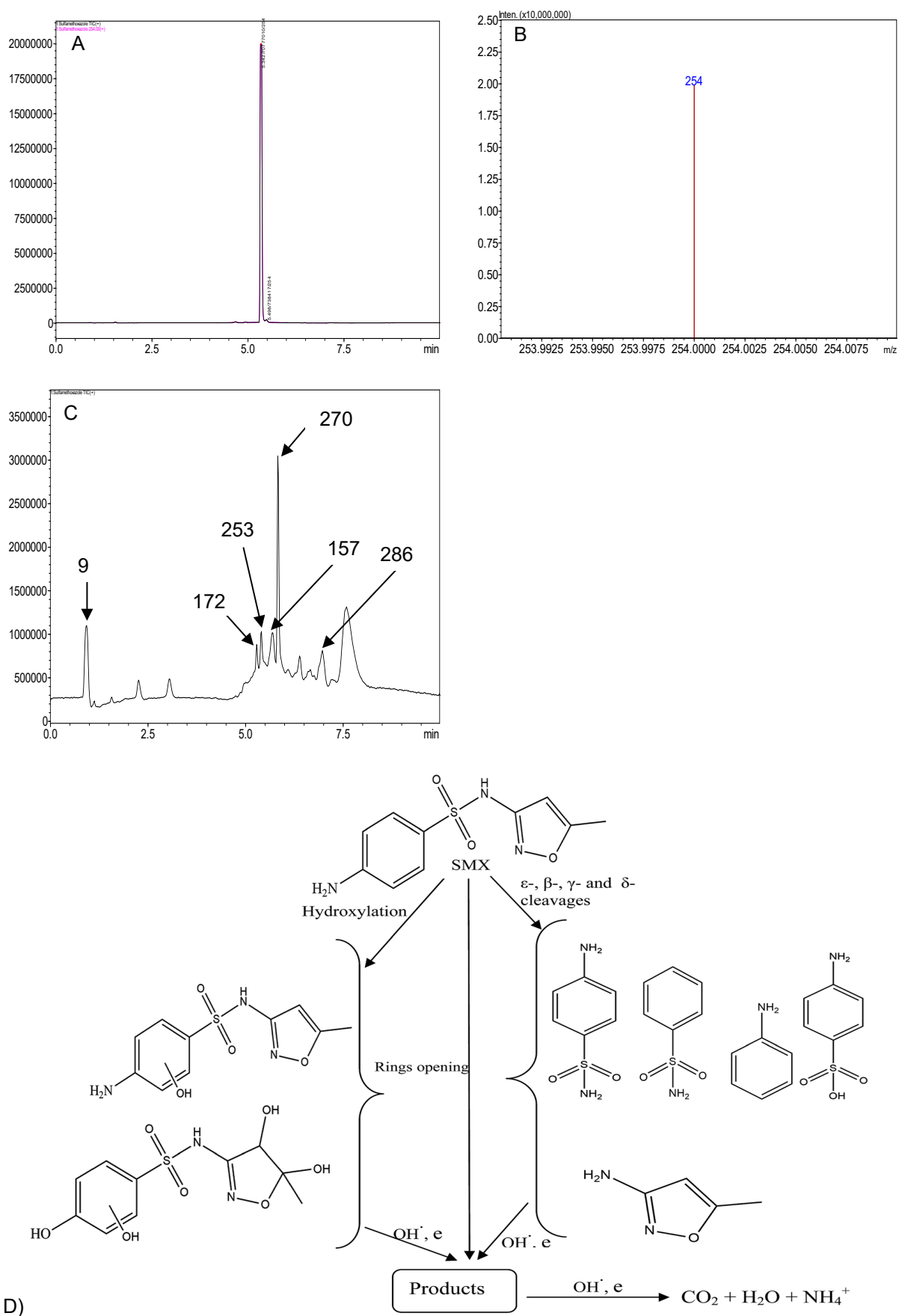


Figure 3.12. A) Chromatogram of SMX solution B) Mass spectrum of SMX solution C) Chromatogram of degraded SMX solution D) Proposed degradation route of SMX by photoelectrochemical process

Table 3-4. Summary of results for degradation studies with TiO<sub>2</sub>-EG photoanode

| Photoanode            | Pollutant        | Key results   |
|-----------------------|------------------|---|
| TiO <sub>2</sub> - EG | Sulfamethoxazole | <p>Time of degradation = 240 min to 360 min<br/> Photoelectrochemical degradation: ca 100% @ 360 min<br/> pH range: 3-6.3. Optimum pH 6<br/> Optimum Current density: 10 mAcm<sup>-2</sup><br/> Chemical oxygen removal (COD) = 90%</p> <p>Kinetics (<math>k_{app}</math>): Photoelectrochemical degradation = <math>5.74 \times 10^{-3}</math> min<sup>-1</sup>.</p> |

**Sub-Conclusion.** The applicability of TiO<sub>2</sub>-EG electrode for the oxidation of SMX via photoelectrocatalytic process was demonstrated in this study. The performance of the photoanode was enhanced in the presence of simulated sunlight, with a fourfold increase in the removal efficiency of the contaminant. The degradation of SMX at the electrode was dependent on pH of the solution and applied current, pH 6.3 and current density 10 mAcm<sup>-2</sup> were taken as optimum. After 6 h of the process at the optimum conditions, 90% of the COD of the solution was removed. LC-MS analysis of the degraded SMX revealed the formation of aniline and other by-products which are believed to result from the interaction of the photoelectrochemically generated hydroxyl radicals and electrons with the parent molecule. Given the ease of preparation, low cost and performance of the TiO<sub>2</sub>-EG anode, it can be further explored for the removal of pharmaceuticals from wastewater.

#### 3.3.9.4 Degradation studies of orange II dye on Pd g-ZnO-EG photoanode

**Abstract of the full study.** A novel Pd-ZnO-expanded graphite (EG) photoelectrode was constructed from a Pd-ZnO-EG nanocomposite synthesised by a hydrothermal method and characterised using various techniques such as X-ray diffractometry (XRD), Raman spectroscopy, UV-Vis diffuse reflectance spectroscopy, nitrogen adsorption-desorption analysis, transmission electron microscopy (TEM), scanning electron microscopy (SEM) and energy dispersive spectrometry (EDS). Cyclic voltammetry and photocurrent response measurements were also carried out on the electrode. The Pd-ZnO-EG electrode was employed in the photoelectrocatalytic removal of 4-nitrophenol as a target water pollutant at a neutral pH and current density of 7 mAcm<sup>-2</sup>. Optical studies revealed that the Pd-ZnO-EG absorbed strongly in the visible light region. The Pd-ZnO-EG electrode showed improved photoelectrocatalytic activity in relation to ZnO-EG and EG electrodes for the removal of the 4-nitrophenol. The photocurrent responses showed that the Pd-ZnO-EG nanocomposite electrode could be employed as a good photoelectrode for photoelectrocatalytic processes and environmental remediation such as treatment of industrial wastewaters. Density functional theory method was used to model the oxidative degradation of 4-nitrophenol by hydroxyl radical which generate hydroquinone, benzoquinone, 4-nitrocatechol, 4-nitroresorcinol and the opening of the 4-nitrophenol ring. Furthermore, the hydroxyl radical is regenerated and can further oxidise the ring structure and initiates a new degradation process.

**Degradation studies.** The photoelectrocatalytic activities of the EG, ZnO-EG and Pd-ZnO-EG electrodes were evaluated by the rate of removal of 4-nitrophenol as a target organic pollutant. The removal rate was monitored using UV-Visible spectroscopy and total organic carbon (TOC) analysis. For control experiments, photolytic, photocatalytic and electrocatalytic removal of 4-nitrophenol were carried out and compared with the photoelectrocatalytic process using the Pd-ZnO-EG material (Fan, Yang, Pu & Zhang, 2014). The results revealed that the removal of 4-nitrophenol was 20% for photolysis, 31% for photocatalysis, 69% for

electrocatalysis and 94% for the photoelectrocatalytic process (Fig. 3.13a). Furthermore, the EG and ZnO-EG electrodes were used as control experiments for the photoelectrocatalytic removal of 4-nitrophenol. As presented in Fig. 3.13b, the kinetics curves show that the ZnO-EG electrode gave a better removal efficiency compared to that of the EG electrode. This is attributed to the photoactive nature of ZnO in the ZnO-EG material. Moreover, after the addition of Pd to the ZnO-EG material, an enhanced photoelectrocatalytic removal performance (94%) was found.

The improved removal efficiency is as a result of the photoactive nature of ZnO and the enhanced absorption of visible light caused by the surface plasma resonance ability of Pd in the composite. The Pd can also behave as electron sink for the photoinduced electrons, thereby minimising the recombination of the electron-hole pairs generated (Long Zhang et al., 2014; W. Zhao et al., 2016). In addition, the ability of the EG to act as electron sink as well as its electron transport nature must have aided in inhibiting the recombination of the photoinduced holes and electrons which led to the improved photoelectrocatalytic performance of the Pd-ZnO-EG electrode. The synergic combination of ZnO, EG and Pd that led to improved photocatalytic degradation can be buttressed with photocurrent responses in Fig. 3.13b which was highest for the Pd-ZnO-EG electrode. The extent of mineralisation of the 4-nitrophenol was evaluated on a TOC analyser after a period of 150 min. The TOC results showed a removal percentage of 58% for Pd-ZnO-EG electrode which is better in comparison with that of EG (32%) and ZnO-EG (40%) electrodes.

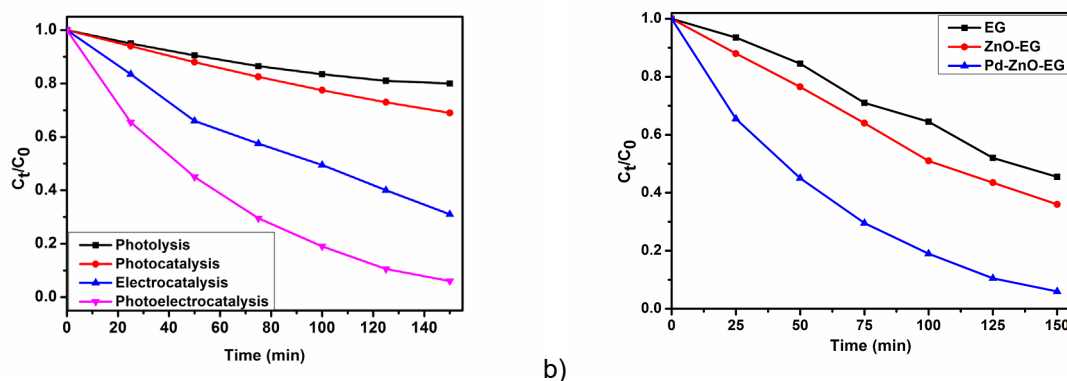


Figure 3.13. Kinetics curves of (a) electrochemical and photoelectrocatalytic removal of 4-nitrophenol at Pd-ZnO-EG electrode. (b) Photoelectrocatalytic removal of 4-nitrophenol at EG, ZnO-EG and Pd-ZnO-EG electrodes.



**Computational modelling of the degradation of 4-nitrophenol** was carried out to understand the degradation mechanism and to predict the degradation products (Umukoro, Peleyeju et al., 2018).

Table 3-5. Summary of results for Degradation studies of orange II dye on Pd g-ZnO-rGO photoanode

| Photoanode | Pollutant     | Key results   |
|------------|---------------|---|
| Pd-ZnO-EG  | 4-nitrophenol | <p>Time of degradation = 150 min</p> <p>The results revealed that the removal of 4-nitrophenol was 20% for photolysis, 31% for photocatalysis, 69% for electrocatalysis and 94% for the photoelectrocatalytic process</p> <p>Photolysis: 20%; Electrochemical degradation: 69%; Photoelectrochemical degradation: 94%</p> <p>Optimum pH: 7</p> <p>Optimum Current density: 5-7.5 mAcm<sup>-2</sup></p> <p>Kinetics: EG = <math>5.53 \times 10^{-3} \text{ min}^{-1}</math>. ZnO-EG = <math>6.97 \times 10^{-3} \text{ min}^{-1}</math> and Pd-ZnO-EG = <math>18.52 \times 10^{-3} \text{ min}^{-1}</math>.</p> <p>Total Organic Carbon removal: EG = 32%; ZnO-EG = 40%; Pd-ZnO-EG = 58%</p> |

**Sub Conclusion.** In summary, Pd-ZnO-EG electrode was constructed from a Pd-ZnO-EG nanocomposite, synthesised by a hydrothermal method and characterised using various techniques. The Pd-ZnO-EG nanomaterials have large surface area, pore size and volume, and strong absorption in the visible light region. The electrode was used for the photoelectrocatalytic removal of 4-nitrophenol as a target water pollutant. The Pd-ZnO-EG electrode showed improved photoelectrocatalytic activity in relation to ZnO-EG and EG electrodes for the removal of the 4-nitrophenol. This is as a result of the Pd nanoparticles and the conducting EG acting as collectors for the photoexcited electrons, thereby aiding charge transfer and reducing recombination of charges. In addition, the photocurrent responses showed that the Pd-ZnO-EG nanocomposite electrode could be employed as a good photo-electrode for the benefits of photoelectrocatalytic processes and environmental remediation such as treatment of industrial wastewaters. The oxidative degradation of 4-nitrophenol by hydroxyl radical was predicted using DFT method which led to the generation of hydroquinone, benzoquinone, 4-nitrocatechol, 4-nitroresorcinol and the ring opening of the 4-nitrophenol. This was obtained by DFT computations of plausible reaction mechanism and pathways resulting from hydroxyl radical attacks on different positions on the molecule of 4-nitrophenol, accompanied by hydrogen abstraction by ground state oxygen reactions. Furthermore, hydroxyl radical was regenerated which can further oxidised the ring structure and initiates a new degradation process.

#### 3.3.9.5 Degradation studies of ciprofloxacin on expanded graphite supported p-n MoS<sub>2</sub>-SnO<sub>2</sub> heterojunction nanocomposite electrode

**Abstract of the full study** (Umukoro, Kumar et al., 2018). Wastewater treatment challenges by conventional methods have necessitated the need for alternative/complementary methods that are environmentally benign and efficient especially toward recalcitrant organic pollutants. In this regard, a novel photoanode consisting of a p-n MoS<sub>2</sub>-SnO<sub>2</sub> heterojunction anchored on expanded graphite (EG) was fabricated and employed in the photo-electrocatalytic degradation of ciprofloxacin, a pharmaceutical pollutant, in water using a current density of 0.010 Acm<sup>-2</sup>. The photoanode material was characterised with transmission electron microscopy (TEM),

scanning electron microscopy (SEM), energy dispersive spectrometry (EDS), Raman spectroscopy and X-ray diffraction (XRD) to confirm that the nanocomposite was successfully prepared. Photoelectrochemical studies were carried out with cyclic/linear sweep voltammetry and chronoamperometry. The removal efficiency of the photo-electrocatalytic cell was determined on a UV-Visible spectrophotometer and the extent of mineralisation was measured by a total organic carbon analyser. The results obtained revealed that the  $\text{SnO}_2$  particles are nanosheets while the  $\text{MoS}_2$  particles are hierarchical microspheres having nanosheets of  $\text{MoS}_2$ , and they were anchored on the interlayers of the EG sheets. Also, the p-n  $\text{MoS}_2$ - $\text{SnO}_2$  heterojunction anchored on expanded graphite (EG) was found to be photoactive and displayed a better removal efficiency and mineralisation in comparison to EG,  $\text{SnO}_2$ -EG and  $\text{MoS}_2$ -EG electrodes. This may be due to the formation of the  $\text{MoS}_2$ - $\text{SnO}_2$  p-n heterojunction in the  $\text{MoS}_2$ - $\text{SnO}_2$ /EG nanocomposite which enhanced the light harvesting ability of the material resulting in its improved photo-electrocatalytic performance. Hence the  $\text{MoS}_2$ - $\text{SnO}_2$ /EG is potentially a good photoelectrode which may be beneficial for a photo-electrocatalytic treatment of industrial wastewaters and other photo-electrocatalytic applications.

**Degradation studies.** The application of the EG,  $\text{MoS}_2$ -EG,  $\text{SnO}_2$ -EG and  $\text{MoS}_2$ - $\text{SnO}_2$ /EG electrodes for the photo-electrocatalytic removal of ciprofloxacin as a typical pharmaceutical pollutant was investigated, and this was monitored using UV-Visible spectroscopy and TOC analysis. At a current density of  $0.010 \text{ A cm}^{-2}$  and a small electrode geometric area of  $1.33 \text{ cm}^2$ , the obtained results showed that the  $\text{MoS}_2$ - $\text{SnO}_2$ /EG electrode displayed a photo-electrocatalytic removal efficiency of 78.5% and an electrocatalytic removal efficiency of 55.5% (Figure 3.14a). Furthermore, as a control experiment, EG electrode was used for the photo-electrocatalytic removal of ciprofloxacin and it gave a removal efficiency of 50.5%. Upon the separate addition of  $\text{MoS}_2$  and  $\text{SnO}_2$  to the EG, 68.5 and 64.5% were obtained for the  $\text{MoS}_2$ -EG and  $\text{SnO}_2$ -EG electrodes respectively. This is due to the photosensitivity of  $\text{MoS}_2$  and  $\text{SnO}_2$ . Moreover, the addition of the  $\text{MoS}_2$ - $\text{SnO}_2$  nanohybrid to the EG gave 78.5% for the  $\text{MoS}_2$ - $\text{SnO}_2$ /EG electrode. This is due to the light harvesting nature of the nanocomposite and the formation of heterojunction between the  $\text{MoS}_2$  and  $\text{SnO}_2$  which led to an improved charge separation and transport, thereby resulting in an improved photo-electrocatalytic performance of the  $\text{MoS}_2$ - $\text{SnO}_2$ /EG nanocomposite. Thus, as shown in Figure 3.14b, the kinetic curves revealed a better photo-electrocatalytic removal of the ciprofloxacin compared to the EG,  $\text{MoS}_2$ -EG and  $\text{SnO}_2$ -EG electrodes (Ke et al., 2017; Yan et al., 2016). These can be corroborated by the results from the photocurrent and linear sweep voltammetry measurements of the different fabricated electrodes.

TOC analysis was carried out to investigate the mineralisation process of the ciprofloxacin after 2 h 30 min. The conversion of the organic carbon gave a removal of 39.7% for  $\text{MoS}_2$ - $\text{SnO}_2$ /EG nanocomposite electrode which is higher when compared to that of EG (25%),  $\text{MoS}_2$ -EG (32%) and  $\text{SnO}_2$ -EG (30%) electrodes. This is in agreement with results obtained for removal efficiency and TOC measurements reported in literatures (Giri & Golder, 2014; Ji, Ferronato, Salvador, Yang & Chovelon, 2014).

A possible mechanism based on band gap alignment for the photo-electrocatalytic process is presented in Fig. 3.14c.

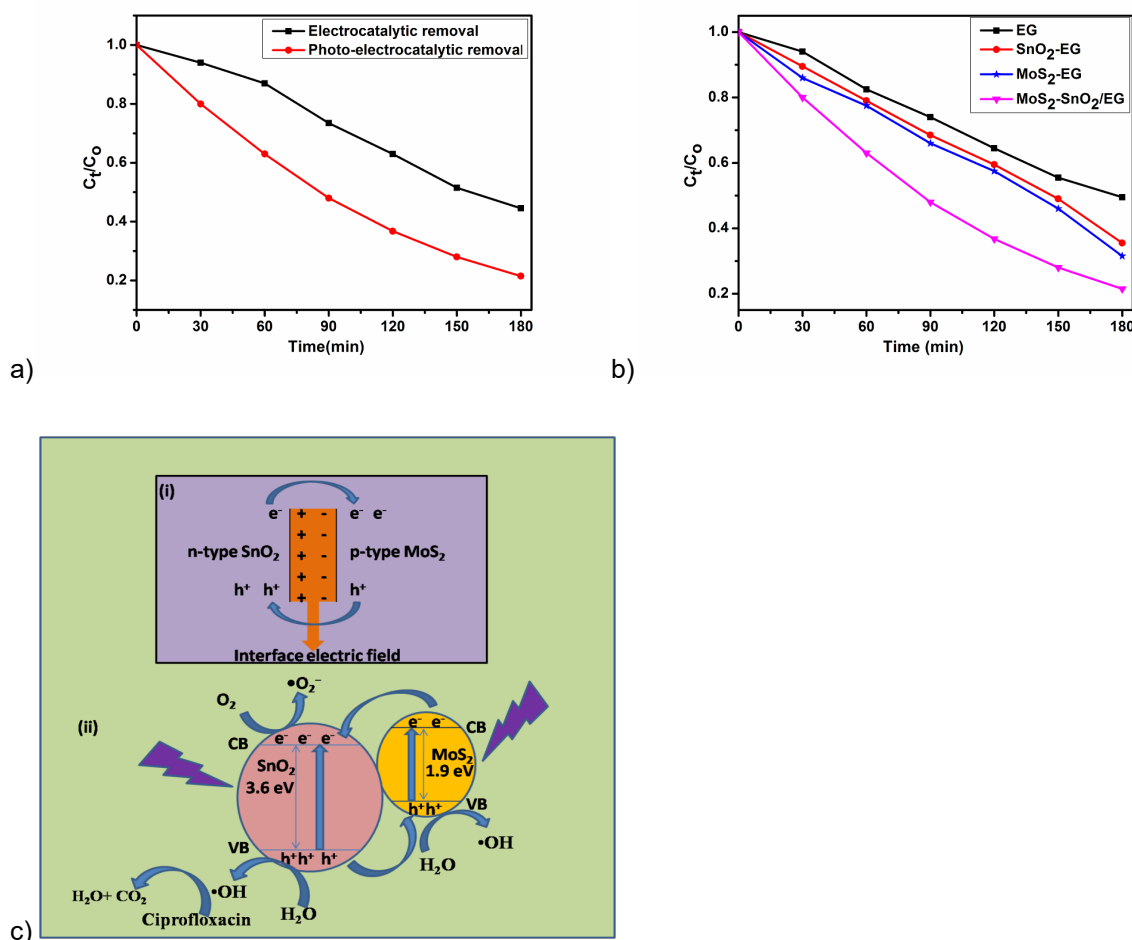


Figure 3.14. Degradation kinetics curves of ciprofloxacin of (a) Electrocatalytic and photo-electrocatalytic on MoS<sub>2</sub>-SnO<sub>2</sub>/EG electrode, and (b) photo-electrocatalytic removal on EG, SnO<sub>2</sub>-EG, MoS<sub>2</sub>-EG and MoS<sub>2</sub>-SnO<sub>2</sub>/EG electrodes. c) Proposed plausible charge transfer mechanism.

Table 3-6. Summary of results for degradation studies with MoS<sub>2</sub>-SnO<sub>2</sub>/EG photoanode

| Photoanode                             | Pollutant     | Key results  |
|--|---------------|--|
| MoS <sub>2</sub> -SnO <sub>2</sub> /EG | ciprofloxacin | <p>Time of degradation = 150 min</p> <p>ON MoS<sub>2</sub>-SnO<sub>2</sub>/EG electrode: Electrochemical degradation = 55.5%; Photoelectrochemical degradation = 78.5%</p> <p>Photoelectrochemical degradation: EG = 50.5%; MoS<sub>2</sub>-EG = 68.5%; SnO<sub>2</sub>-EG = 64.5% and MoS<sub>2</sub>-SnO<sub>2</sub>/EG = 78.5%</p> <p>Optimum pH: 5.4</p> <p>Optimum Current density: 10 mAcm<sup>-2</sup></p> <p>Total Organic Carbon removal: EG = 25%; MoS<sub>2</sub>-EG = 32%; SnO<sub>2</sub>-EG = 30% and MoS<sub>2</sub>-SnO<sub>2</sub>/EG = 39.7%</p> <p>Kinetics: EG = 4.06 × 10<sup>-3</sup> min<sup>-1</sup>; MoS<sub>2</sub>-EG = 5.97 × 10<sup>-3</sup> min<sup>-1</sup>; SnO<sub>2</sub>-EG = 5.47 × 10<sup>-3</sup> min<sup>-1</sup> and MoS<sub>2</sub>-SnO<sub>2</sub>/EG = 8.63 × 10<sup>-3</sup> min<sup>-1</sup>.</p> |

**Sub-Conclusion.** This work reports the synthesis and characterisation of a novel photo-electrode consisting of a p-n MoS<sub>2</sub>-SnO<sub>2</sub> heterojunction anchored on expanded graphite (EG). This was applied in the photo-electrocatalytic degradation of ciprofloxacin as a target pharmaceutical pollutant in water. The fabricated electrode exhibited a better photo-electrocatalytic performance compared to MoS<sub>2</sub>-EG, SnO<sub>2</sub>-EG and EG electrodes for the removal of the ciprofloxacin. This could be attributed to the formation of the MoS<sub>2</sub>-SnO<sub>2</sub> p-n heterojunction in the nanocomposite which aided charge separation and transfer, thereby resulting in the minimisation of the recombination rate of the photoinduced electrons and holes. Furthermore, the linear sweep voltammetry and photocurrent measurements revealed that the nanocomposite electrode is rendered a good photo-electrode which can be beneficial for photo-electrocatalytic treatment of industrial wastewaters and other photo-electrocatalytic reactions.

### 3.3.9.6 *Degradation studies of Rhodamine B on an exfoliated graphite-BiVO<sub>4</sub>/ZnO heterostructured nanocomposite Electrode*

**Abstract of the full study** (Orimolade et al., 2019). A novel photoanode consisting of an exfoliated graphite-BiVO<sub>4</sub>/ZnO heterostructured nanocomposite was fabricated. The material was characterised with scanning electron microscopy (SEM), energy dispersive spectrometry (EDS) and X-ray diffraction (XRD). Photoelectrochemical studies were carried out with cyclic/linear sweep voltammetry and chronoamperometry. The solar photoelectrochemical properties of the heterojunction photoanode were investigated through the degradation of rhodamine B in water. The results revealed that the nanoparticles of BiVO<sub>4</sub> and ZnO were well entrapped within the interlayers of the exfoliated graphite (EG) sheets. Improved charge separation was achieved in the EG-BiVO<sub>4</sub>/ZnO composite electrode which resulted in higher photoelectrochemical performance than individual BiVO<sub>4</sub> and ZnO electrodes. Higher degradation efficiency of 91% of rhodamine B was recorded using the composite electrode with the application of 10 mAcm<sup>-2</sup> current density and solution pH of 7. The highest total organic carbon removal of 74% was also recorded with the EG-BiVO<sub>4</sub>/ZnO. Data from scavenger studies were used to support the proposed mechanism of degradation. The electrode has high stability and reusability and hence lends itself to applications in photoelectrocatalysis especially in water treatment.

**Electrochemical characterisation of electrodes.** The cyclic voltammograms of EG, EG-ZnO, EG-BiVO<sub>4</sub> and EG-BiVO<sub>4</sub>/ZnO were recorded at a scan rate 20 mVs<sup>-1</sup> using 0.1 M KCl solution in 5 mM [Fe(CN)<sub>6</sub>]<sup>3-/4-</sup> as the redox probe as shown in Fig. 3.15a. The EG-BiVO<sub>4</sub>/ZnO electrode showed the highest faradaic peak current than all the other electrodes which suggested that the electrode reaction rate is higher (Umukoro, Peleyeju et al., 2017). Both the EG-ZnO and EG-BiVO<sub>4</sub> electrode performed better than the bare EG electrode and this could be attributed to that fact that the addition of ZnO and BiVO<sub>4</sub> to the EG resulted in increased electroactive surface area and thereby increased the conductivity. The electroactive surface area of all the electrodes were calculated using the Randles-Sevcik equation:  $p = kn^{3/2}AD^{1/2}v^{1/2}C$ . Where A is the electroactive surface area, ip is the peak current, C is the redox probe concentration, D is the diffusion coefficient (7.6 x 10<sup>-6</sup> for ferrocyanide), v is the scan rate and k is a constant (2.69 x 10<sup>5</sup>). The electroactive surface areas obtained are 0.196 mm<sup>2</sup>, 0.239 mm<sup>2</sup>, 0.248 mm<sup>2</sup> and 0.309 mm<sup>2</sup> for EG, EG-ZnO, EG-BiVO<sub>4</sub> and EG-BiVO<sub>4</sub>/ZnO electrodes respectively. The largest surface area of the EG-BiVO<sub>4</sub>/ZnO justified the highest faradaic current obtained with the electrode.

The linear sweep voltammetry of the EG, EG-ZnO, EG-BiVO<sub>4</sub> and EG-BiVO<sub>4</sub>/ZnO were recorded using 0.1 M Na<sub>2</sub>SO<sub>4</sub> as supporting electrolyte and was carried out both in the dark and light (Fig. 3.15b). The EG-BiVO<sub>4</sub>/ZnO composite electrode gave the highest current as compared to the other electrodes both in the dark and in the light. The enhanced current observed is due to the formation of heterojunction between the BiVO<sub>4</sub> and ZnO which resulted in better separation of the electron-hole pairs. This was further confirmed by the photocurrent response with the application of 1.5 V bias potential (Fig. 3.15c). The EG-BiVO<sub>4</sub> electrode gave a higher photocurrent (0.049 mAcm<sup>-2</sup>) than that of EG-ZnO (0.031 mAcm<sup>-2</sup>) and this is due to the fact that visible light was used to irradiate the electrode and BiVO<sub>4</sub> has higher photoactivity than ZnO in the visible light region due its lower band gap.

Overall, the EG-BiVO<sub>4</sub>/ZnO electrode gave the best photocurrent response of 0.069 mAcm<sup>-2</sup> and this confirmed that the heterojunction formed between the BiVO<sub>4</sub> and ZnO resulted in increased interfacial charge transfer and lowered the recombination rate of the charge carriers. Moreover, it is quite interesting to observe that the BiVO<sub>4</sub>, ZnO and BiVO<sub>4</sub>/ZnO electrodes with EG as the conducting substrate gave higher photocurrent responses than their counterpart electrodes with FTO used as the conducting substrate previously reported (Feng, Cheng, Zhang, Okoth & Chen, 2018; J.-S. Yang & Wu, 2017). This is mostly due to the fact that EG also enhanced effective charge separation by acting as a reservoir for the photogenerated charge carriers. In addition to this, carbon materials can also serve as dopants for semiconductors generating internal electric field contributing to formation of effective heterojunction (Liping Zhang & Jaroniec, 2018).

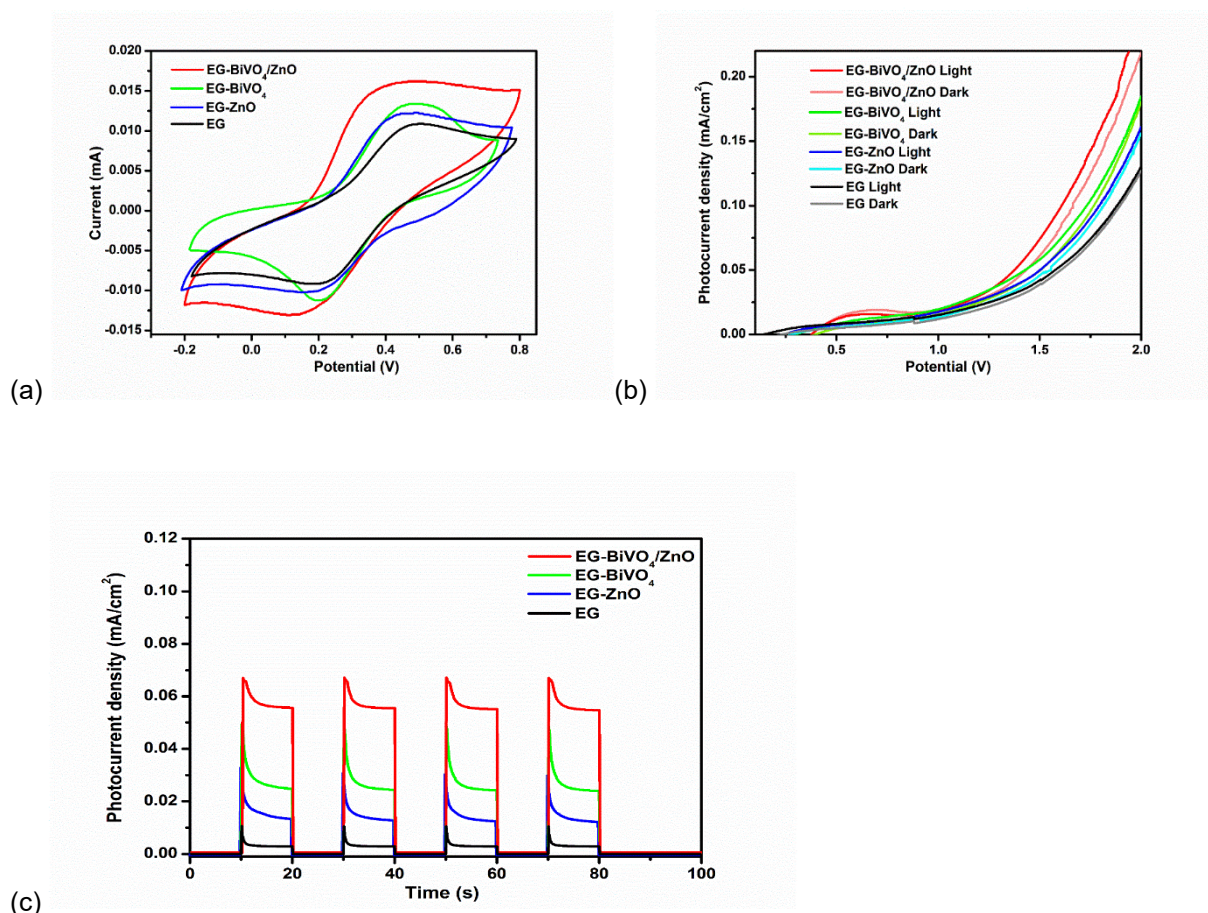


Figure 3.15. (a) CVs of EG, EG-BiVO<sub>4</sub>, EG-ZnO, EG-BiVO<sub>4</sub>/ZnO composite electrodes using 5 mM [Fe(CN)<sub>6</sub>]<sup>3-/4-</sup> in 0.1 M KCl solution at a scan rate of 20 mVs<sup>-1</sup>; (b) LSV and (c) Photocurrent responses of EG, EG-BiVO<sub>4</sub>, EG-ZnO and EG-BiVO<sub>4</sub>/ZnO in 0.1 M Na<sub>2</sub>SO<sub>4</sub>.

**Degradation of Rhodamine B.** The prepared electrodes were applied in the solar photoelectrocatalytic (PEC) degradation of rhodamine B dye with initial concentration of  $10 \text{ mgL}^{-1}$ . The degradation efficiency was monitored using UV-Visible spectrophotometer at a wavelength of 554 nm. As shown in Fig. 3.16a, there was decrease in the intensity of the peak at 554 nm with increase in the reaction time revealing the reduction in the concentration of the dye. Degradation efficiency of 91% was achieved using the EG-BiVO<sub>4</sub>/ZnO composite electrode in the photoelectrocatalytic degradation process. When the composite electrode was applied in electrochemical (EC) degradation (without the application of solar light), the degradation efficiency dropped to 56% while in photocatalysis (PC), 37% degradation efficiency was recorded (Fig. 3.16b). The total organic carbon (TOC) removal obtained were 74%, 46% and 35% using PEC, EC and PC respectively. This observation revealed that application of biased potential plays a vital role in the degradation process. Additionally, when the electrode is irradiated with the solar light, the electrode absorbs photons and electron-hole pairs are generated within the BiVO<sub>4</sub> and ZnO. The holes act as oxidants for breaking down the dye molecules and also react with water to generate hydroxyl radicals which are stronger oxidants necessary for the rapid oxidation of the dye molecules. The combined effect of electrical energy and solar energy accounted for the highest degradation efficiency achieved in the PEC process. The degradation rate constants for the three processes (PC, EC and PEC) were obtained by fitting the data into Langmuir-Hinshelwood pseudo first order kinetic model equation. As shown in Fig. 3.16c, the rate of the PEC process was the fastest with apparent rate constant of  $0.00921 \text{ min}^{-1}$  when compared to both PC and EC processes with rate constants of  $0.00154 \text{ min}^{-1}$  and  $0.00332 \text{ min}^{-1}$  respectively.

Among all the electrodes prepared, the bare EG electrode performed least with 27% degradation efficiency. The EG-BiVO<sub>4</sub> electrode performed better (61% efficiency) than the EG-ZnO (52%) electrode because the BiVO<sub>4</sub> has higher photocatalytic activity in the visible light region due to its lower band gap (Fig. 3.16d). The formation of BiVO<sub>4</sub>/ZnO heterojunction was deduced through the improved photoelectrocatalytic activity of all the composite electrodes with different ratios of BiVO<sub>4</sub> to ZnO. The formation of heterojunction enhanced better charge separation and lowered the rapid recombination rate of electron-hole pairs resulting in better light harvesting. The EG-BiVO<sub>4</sub>/ZnO consisting of BiVO<sub>4</sub> and ZnO in ratio 1:1 gave the highest degradation efficiency and was therefore used for all other studies.

The effects of parameters such as current densities and solution pH on the photoelectrocatalytic process were as studied. The degradation efficiency increased with increased in the applied current densities from  $5 \text{ mAcm}^{-2}$  to  $15 \text{ mAcm}^{-2}$  (Fig. 3.16e). The increase from  $5 \text{ mAcm}^{-2}$  to  $10 \text{ mAcm}^{-2}$  (62% to 91%) was more pronounced as compared to the increase observed from  $10 \text{ mAcm}^{-2}$  to  $15 \text{ mAcm}^{-2}$  (91% to 95%). This revealed the dependence of hydroxyl radicals production on the applied current densities but when too high current densities are applied, it could result in oxygen evolution which hinder the generation of hydroxyl radical and thereby limit the degradation efficiency (Qiu et al., 2019). More so, the application of higher current densities is not cost and energy effective. Increase in pH from 3 to 10 (Fig. 3.16f) resulted in decrease in the degradation efficiency which confirmed the suitability of acidic medium for degradation of Rhodamine B dye (Baddouh et al., 2018).

An ideal photoanode for degradation of organics is expected to be stable and reusable. The stability and reusability of the prepared EG-BiVO<sub>4</sub>/ZnO in PEC degradation process was also investigated by carrying out

repeating experiments (cycles) using the same electrode. The electrode was cleaned with deionized water after each cycle. As shown in Fig 4g, the degradation efficiency dropped by less than 1% after the third cycle which implies that the electrode is relative stable and can be reused for PEC degradation.



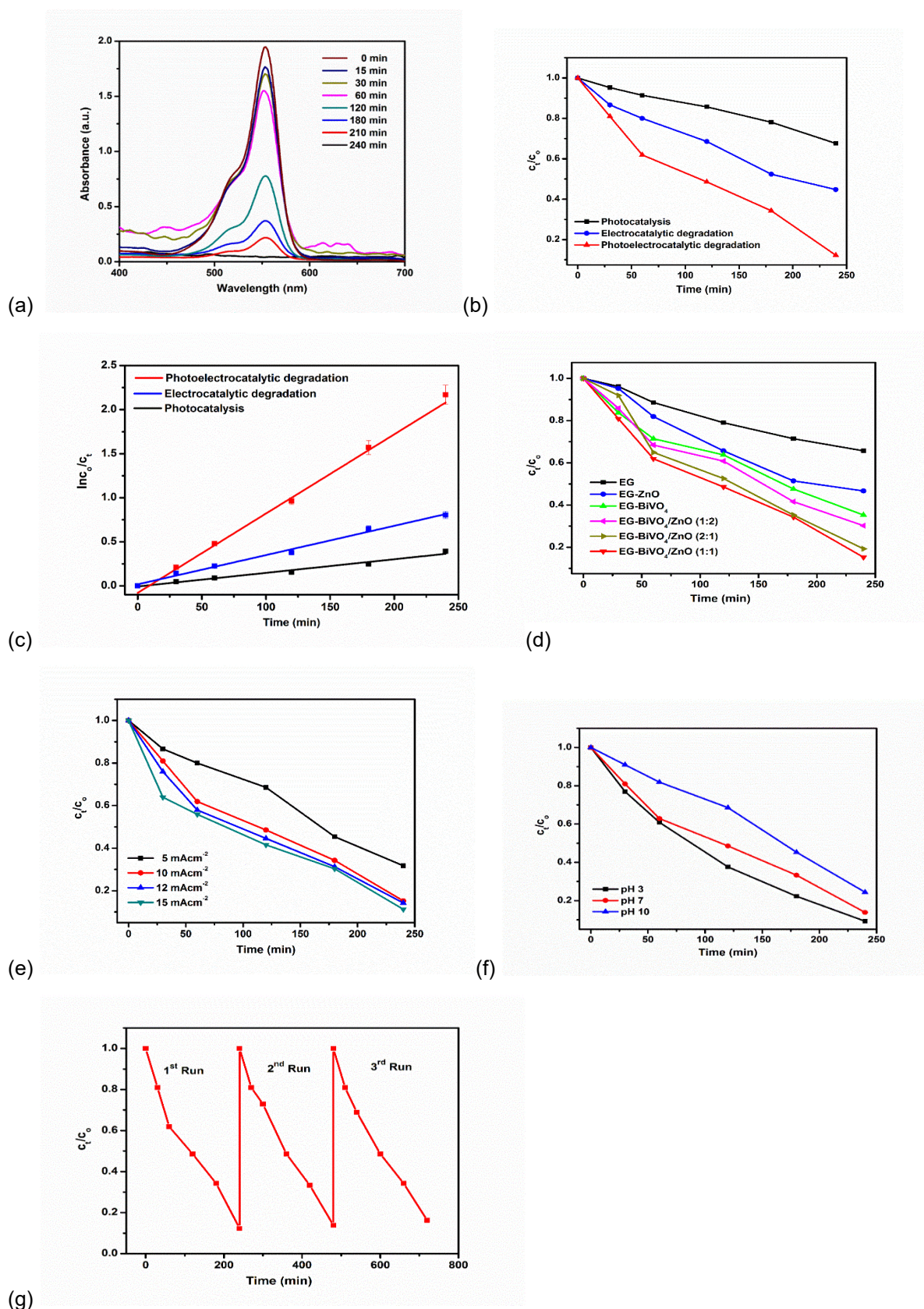
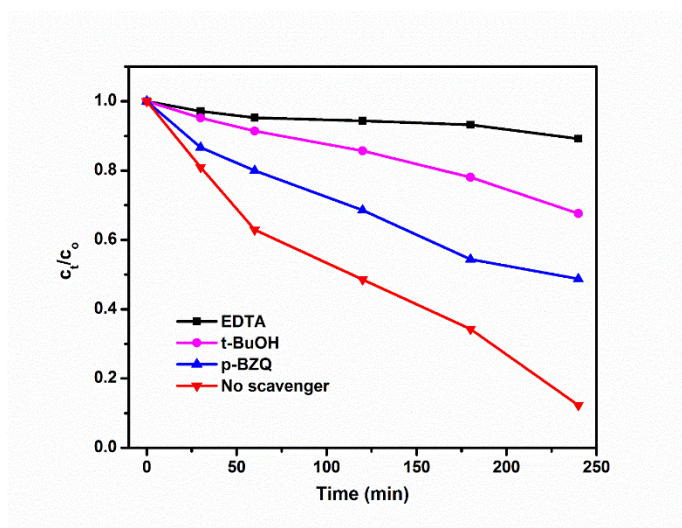


Figure 3.16. (a) UV-Vis spectra of PEC degradation of rhodamine B. (b) Normalised concentration decay versus time plot for photocatalytic, electrocatalytic and photoelectrocatalytic degradation of rhodamine B dye on EG-BiVO<sub>4</sub>/ZnO electrode and (c) corresponding kinetics plots. (d) Normalised concentration decay versus time plot for PEC degradation of rhodamine B dye on EG-ZnO, EG-BiVO<sub>4</sub>, EG-BiVO<sub>4</sub>/ZnO electrodes. (e) Effects of current density and (f) pH on degradation of rhodamine B dye. (g) Cycle experiments for the degradation of rhodamine B dye on EG-BiVO<sub>4</sub>/ZnO electrode.

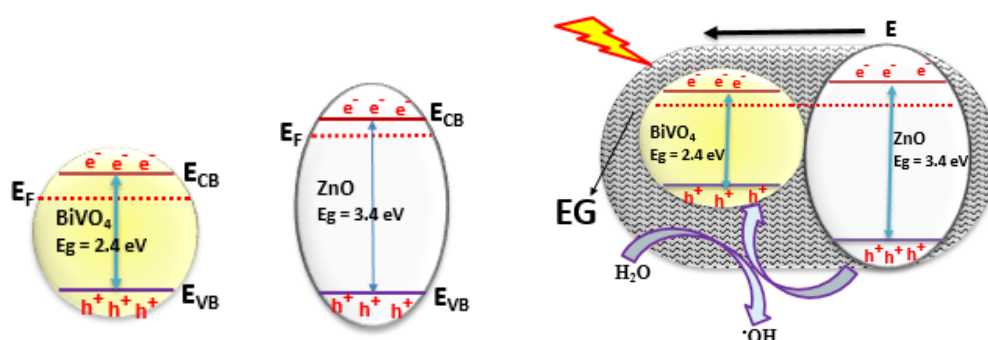


**Scavenger studies.** To get a clearer picture of the roles of the active species in the PEC degradation of rhodamine B, scavenger study was carried out. This was done by using ethylenediaminetetraacetate salt (EDTA), t-butanol (t-BuOH) and p-benzoquinone (p-BZQ) to suppress the effect of holes, hydroxyl radicals and superoxide radicals respectively (Akbarzadeh, Fung, Rather & Lo, 2018; Medel, Ramírez, Cardenas, Sires & Meas, 2019). The results are shown in Fig. 3.17a. Upon the addition of EDTA, the degradation efficiency dropped drastically to less than 10% which revealed that the photogenerated holes play a major role in the degradation of the rhodamine B dye. With the addition of t-BuOH and p-BZQ the degradation efficiencies were 31% and 52% respectively suggesting that both hydroxyl radicals and superoxide radicals play a lesser role in the degradation of the dye.

The pronounced role of the photogenerated holes in degradation of the dye molecules could be attributed to a better separation of the electron-hole pairs in the BiVO<sub>4</sub>/ZnO heterojunction making more holes available to oxidise the dye molecules. This observation provided a glimpse into the band alignment between ZnO and BiVO<sub>4</sub>. Considering the band edge positions of intrinsic BiVO<sub>4</sub> and ZnO, a type I heterojunction can be proposed in which the charge carriers accumulate onto the BiVO<sub>4</sub> and this will not result in proper charge separation as the charge carriers can still recombine in the surface of the BiVO<sub>4</sub>. This was unlikely to happen since carbons (from EG) act as dopants for both ZnO and BiVO<sub>4</sub> leading to non-negligible internal electric field. Therefore, Fermi energy levels ( $E_F$ ) of the two semiconductors aligned through the movement of electrons from the ZnO (higher  $E_F$ ) to BiVO<sub>4</sub> (lower  $E_F$ ) and the direction of internal electric field ( $E$ ) was from ZnO to BiVO<sub>4</sub> preventing the movement of electrons in the same direction after the formation of heterojunction. On the other hand the direction of the internal electric field favoured the movement of holes in the same direction and hence holes were most efficient separated onto the valence band of BiVO<sub>4</sub> and available for oxidizing the rhodamine B molecules (Liping Zhang & Jaronec, 2018). This deduction is illustrated in Fig. 3.17b.



(a)



(b)

Figure 3.17. (a) Scavenger studies of the PEC degradation of rhodamine B dye on EG-BiVO<sub>4</sub>/ZnO. (b) Band alignment between ZnO and BiVO<sub>4</sub>.

Table 3-7. Summary of results for degradation studies with EG-BiVO<sub>4</sub>/ZnO photoanode

| Photoanode                | Pollutant       | Key results   |
|---------------------------|-----------------|---|
| EG-BiVO <sub>4</sub> /ZnO | Rhodamine B dye | <p>Time of degradation = 240 min</p> <p>Degradation efficiency on EG-BiVO<sub>4</sub>/ZnO photoanode: 91% photoelectrocatalytic (PEC); 56% electrochemical (EC) degradation; 37% photocatalysis (PC).</p> <p>Degradation: 27% EG; 61% EG-BiVO<sub>4</sub> electrode; 51% EG-ZnO</p> <p>Kinetics on EG-BiVO<sub>4</sub>/ZnO: PEC = 0.00921 min<sup>-1</sup>; EC = 0.00332 min<sup>-1</sup>; PC = 0.00154 min<sup>-1</sup>.</p> <p>Total organic carbon (TOC) removal on EG-BiVO<sub>4</sub>/ZnO: 74% (PEC), 46% (EC) and 35% (PC).</p> |

**Sub Conclusion.** In this work, we have prepared a novel heterojunction photoanode of EG-BiVO<sub>4</sub>/ZnO. The formation of BiVO<sub>4</sub>/ZnO heterojunction with enhanced separation of charge carriers was confirmed through the photocurrent response of the EG-BiVO<sub>4</sub>/ZnO composite electrode which was higher than that of both the EG-BiVO<sub>4</sub> and EG-ZnO. The exfoliated graphite, used as the conducting substrate, also improved charge separations by acting as a sink for the charge carriers. When applied for the photoelectrocatalytic degradation of rhodamine B, a degradation efficiency of 91% (from visible spectroscopy) and a total organic carbon removal of 74% were recorded with the EG-BiVO<sub>4</sub>/ZnO heterostructured photoanode. Scavenger studies revealed that photogenerated holes played a major role in the degradation of the dye since the band alignment between the

BiVO<sub>4</sub> and ZnO resulted in better charge separation of the holes. The composite electrode has high stability and the reaction rate is fast with apparent rate constant of 0.00921 min<sup>-1</sup>. The electrode has a great potential for PEC applications in wastewater treatment for the removal of organics.

## **CHAPTER 4: ELECTROCOAGULATION FOR THE TREATMENT OF ORANGE II DYE COMBINED WITH HEAVY METALS IN WASTEWATER**

---

### **4.1 INTRODUCTION**

Limitation of water resources is a global challenge and South Africa is among the countries that are most affected. It is therefore necessary to effectively manage the increasingly limited water supply owing to industrialisation, increase in population, and so on. For example, the textile industry is among the fastest growing industries in the world due to increasing population (Halimoon & Yin, 2010). A positive aspect of this growth is the increase in Gross Domestic Product (GDP) of some countries such as India and Sri Lanka. The downside of industrialisation however, is the increase in water pollution due to the complex, toxic and recalcitrant chemicals (pollutants) generated during processes. These pollutants present a challenge to the conventional water treatment methods. This problem necessitates the need for industries producing harmful effluents to implement alternative/complementary methods that can be developed and applied on site before discharge and/or for the purpose of re-using the wastewater. Furthermore, these technological designs may be incorporated into the process operations of water treatment plants to optimise the availability of clean water for industrial and domestic use (Shannon et al., 2008).

In recent years, great attention has been given to the development of new methods or hybrids of some well-known technologies for wastewater treatment for cheaper, sustainable and more environmentally friendly processes. These new developments sometimes require the extension and advancement of methods, ideas/designs for improved efficiency and cost reduction (Cardoso, Bessegato & Zanoni, 2016). In SA, most of the wastewater is treated by physical/physicochemical process and biological processes, and only a few (probably less than 20%) account for other processes such as electrochemical and advanced oxidation processes (DWA, 2013). The majority of the applied conventional processes, however, faces a challenge in efficiently removing pollutants from complex wastewaters. Some techniques are either effective in lowering the concentration of dissolved organics or inorganics, whilst others are sensitive to toward the toxicity of certain chemicals, requires a lot of operation time, large land area, expensive chemicals, strict operating conditions, expensive and routine maintenance (Jaafarzadeh, Omidinasab & Ghanbari, 2016).

It is important to explore other water treatment processes and optimise them to adapt to the ever-changing pollution load of industrial effluents. In this manner, looking towards their implementation to be developed and applied on site by industries before discharge and/or incorporated into the process operations of water treatment plants (Jaafarzadeh et al., 2016; Touahria, Hazourli, Touahria, Eulmi & Aitbara, 2016). Electrocoagulation (EC) is one of the processes that has received a great deal of attention in treating various wastewaters, because of its versatility, environmental compatibility, its simplicity and suitability to be powered by renewable electricity sources and it allows for use as a small scale decentralized unit (Bocos, Brillas, Sanroman & Sirés, 2016; Touahria et al., 2016). It can achieve the removal of toxic heavy metals and the degradation of organic pollutants without some drawbacks that conventional chemical treatments have

(Neelavannan & Basha, 2008). In addition, it may offer an efficient means of controlling pollution without serious environmental concerns and possibly ensure better service delivery for municipalities, reduced wastewater treatment costs and increased plant efficiencies.

The EC process involves the destabilisation of emulsified contaminants in an aqueous medium or colloids, by introducing an electric current into the medium. Coagulants are generated progressively in-situ by dissolving sacrificial anodes, e.g. (Al/Fe) (Chafi, Gourich, Essadki, Vial & Fabregat, 2011; Oncel, Muhcu, Demirbas & Kobya, 2013), at appropriate conditions (e.g. pH, conductivity, etc.) via electro-oxidation process to form insoluble metal hydroxide. The hydroxide is then able to remove suspended particles by surface complexation, adsorption or electrostatic attraction (Bocos et al., 2016; Hakizimana et al., 2017). This technique solely aims at: i) Using less chemicals (coagulants and disinfectants) (Chafi et al., 2011), leading to less sludge formation. ii) Being able to remove recalcitrant pollutants. iii) Simultaneous removal of heavy metals iv) Being easy to design (requiring minimal start up time) and incorporated into the wastewater treatment process, v) being easy to operate with shorter retention time and high sedimentation velocities (Khandegar & Saroha, 2013). In addition to the considerably less sludge formed by EC, the sludge is non-toxic as it can be utilized as a soil additive and contains metal oxides that pass the leachability test. Most importantly, the cost of disposing the sludge is reduced considerably.

One of the important parameters to consider in application of the EC process is the material of the electrode, because it affects mainly the oxidation mechanism and the anodic reactions. In the selection process, electrode material properties of interest includes; non-toxicity to human, health and environment, cheap, readily available, its effectiveness, physical and chemical stability under high positive potentials as well as corrosion resistances. Generally, sacrificial electrode materials are Al and Fe. Iron electrode has been established as the cheapest material that has good COD and turbidity removal efficiencies. In most studies, stainless steel (SS) has been used as Fe electrodes, disregarding the other reactions that may occur due to other components in the SS. SS is an iron based alloy containing  $\geq 11\%$  chromium, with excellent corrosion resistances. SS 304 is the most commonly used alloy, with 18% Cr, 8% Ni and 0.08% C, whereas SS 316 has 18% Cr, 14% Ni, 0.03% C and 3% Mo, making it slightly more corrosion resistant especially in the environments that are inclined to cause pitting, e.g. chlorides (States, America, Institute, Iron & Institute, 1993).

Research on the combination of electrocoagulation with some other unconventional technologies is gaining momentum recently (Aziz, Asaithambi & Daud, 2016; García-García et al., 2015; Kruthika et al., 2013; Linares Hernández et al., 2017; Naje, Chelliapan, Zakaria & Abbas, 2015; Rubí-Juárez et al., 2015; Thiam et al., 2014). With good understanding of the basic and applied science of EC and photoelectrocatalysis, we envisage a hybrid system that can be used for the pre-treatment of wastewater.

This chapter focuses on two studies:

1. ***Treatment of orange II dye and heavy metal in simulated wastewater: Chemical coagulation (CC) versus electrocoagulation.*** This is a preliminary study towards the understanding of EC.

2. ***The application of SS 316 and SS 304 electrodes in electrocoagulation for the treatment of simulated wastewater: a comparative study.*** This a comparative study of three anodic materials.

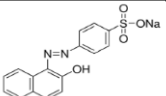
The methodology of this chapter is divided into these two topics with the following short titles: 1. CC vs EC and 2. Comparative study

## 4.2 METHODOLOGY ON CC VS EC

### 4.2.1 Materials, analytical measurements and experimental equipment

Orange II dye was used to impart colour into the synthetic wastewater. The characteristics of the dye are represented in Table 4-1. Heavy metal salts that were used for metal addition in the simulated wastewater were zinc (II) sulphate heptahydrate ( $\text{ZnSO}_4 \cdot 7\text{H}_2\text{O}$ ) and lead (II) nitrate ( $\text{Pb}(\text{NO}_3)_2$ ). Aluminium sulphate (Alum) and ferric chloride ( $\text{FeCl}_3$ ) were used as chemical coagulants. Electrode materials that were used are aluminium (alloy - temper: 1050 - H14, 99.5% purity), stainless steel (SS) (304 and 316 L) and copper. The pH of the simulated wastewater was adjusted using 0.1 M sodium hydroxide (NaOH) and hydrochloric acid (HCl), depending on the pH requirement for the coagulation stage and effluent's initial pH ( $\text{pH}_i$ ). NaCl was used to increase the conductivity of the synthetic effluent in the electrocoagulation studies. In addition, 0.01 M HCl was prepared and used for electrode cleaning after each experiment (Hussin, Abnisa, Issabayeva & Aroua, 2017). All reagents were of analytical grade, purchased from Sigma Aldrich, Germany, and they were used without further purifications.

Table 4-1: Orange II dye characteristics (de Deus Rodrigues, 2013)

| Generic name  | IUPAC name  | Molecular formula  | Molecular weight (g/mol) | Class | $\lambda_{\text{max}}$ (nm) | Chemical structure  |
|---------------|---|--|--------------------------|-------|-----------------------------|---|
| Orange II dye | Sodium;4-[(2E)-2-(2-oxonaphthalen-1-ylidene)hydrazinyl]benzenesulfonate | $\text{C}_{16}\text{H}_{11}\text{N}_2\text{NaO}_4\text{S}$ | 350.324                  | Azo   | 483                         |  |

Decolourisation of the dye was investigated with UV-Visible spectrophotometer at maximum absorption wavelength of 483 nm (Cary 60, Agilent technologies, Australia). Atomic absorption spectrometry (AAS CS1330) was used to analyse the metal concentration before and after each experiment. The simulated wastewater turbidity was measured using a portable Aqua Lytic turbidimeter AI250T-IR with features ranging from 0.01 to 1100 NTU. The chemical oxygen demand (COD) was measured with a HACH digester (150°C for 2 h), using digesting solutions of HR (0-1500 ppm) and a HACH spectrophotometer (Model DR/4000). The pH was measured using pH meter and conductivity meter was used to determine the conductivity of the samples. A 30 V/5 A direct power supply was used in the electrochemical part of the research for electricity supply. All characterisation experiments were performed on samples filtered with 0.22  $\mu\text{m}$  pore size filters, at the University of Johannesburg. The degree of decolourisation and metal removal, the amount (in grams) of electrode consumed after each run, electrical energy consumption and total operating cost were determined using the following equations (Ghosh, Medhi & Purkait, 2008);

$$\text{Pollutant removal (\%)} = \frac{C_o - C_t}{C_o} \times 100 \dots \dots \dots (1)$$

Where;  $C_o$  is the initial (ppm) of the pollutants and  $C_t$  is the pollutant concentration after treatment (ppm).

$$C_{electrode} \left( \frac{kg}{m^3} \right) = \frac{I \times t_{EC} \times M_w}{z \times F \times V} \dots \dots \dots (2)$$

Where,  $C_{electrode}$  is the consumption of metal electrode in  $kg/m^3$ ,  $I$  is the current (A),  $M_w$  is the molecular of the electrode material (g/mol),  $z$  (unitless) is the number of transferred electrons (e.g. for Al electrode,  $z = 3$ ),  $t_{EC}$  is the treatment time (s),  $F$  is Faraday's constant (96 487 C/mol) and  $V$  is slurry volume ( $m^3$ ).

$$C_{electrode} \left( \frac{kWh}{m^3} \right) = \frac{U \times I \times t_{EC}}{V} \dots \dots \dots (3)$$

Where;  $C_{electrodes}$  is the energy consumption in  $kWh/m^3$ ,  $U$  is the voltage (V),  $I$  is the current (A),  $T$  is the treatment time (h) and  $V$  is the volume of the aqueous solution ( $m^3$ ).

$$Operating \ cost \left( \frac{R}{m^3} \right) = aC_{energy} + bC_{electrode} \dots \dots \dots (4)$$

Where;  $a$  represents the 2017-2018 electricity price in South Africa (97.03 R/kWh),  $b$  represents the 2017 retail metal sheets (Al = 67.88 R/kg). The settleability of the bulk sample was determined by drawing the supernatant at different time intervals and analysed for different wastewater parameters discussed above.

Chemical coagulation (CC) experiments were carried out in a jar test apparatus (Fig. 4.1). The jar test apparatus consists of six 1 L cylindrical flasks with mounted steel stirrer of 0.8467 cm long rods and paddles of size 25.4 cm. The unit is also fitted with a digital RPM indicator and timer (that was used for settling rate determination). The effective level of slurry in the jars for the CC experiments was determined using different amounts of deionised water and stirring at maximum speed. All the CC experiments were run at total slurry volume of 400 mL in the jars to avoid vortexing. In addition, the coagulants were added as salts to the jars and allowed to dissolve, whilst stirring at 180 rpm for 1 min. The samples were allowed to coagulate for 29 min at a speed of 30 rpm. This sequence of stirring was done for all CC the experiments.

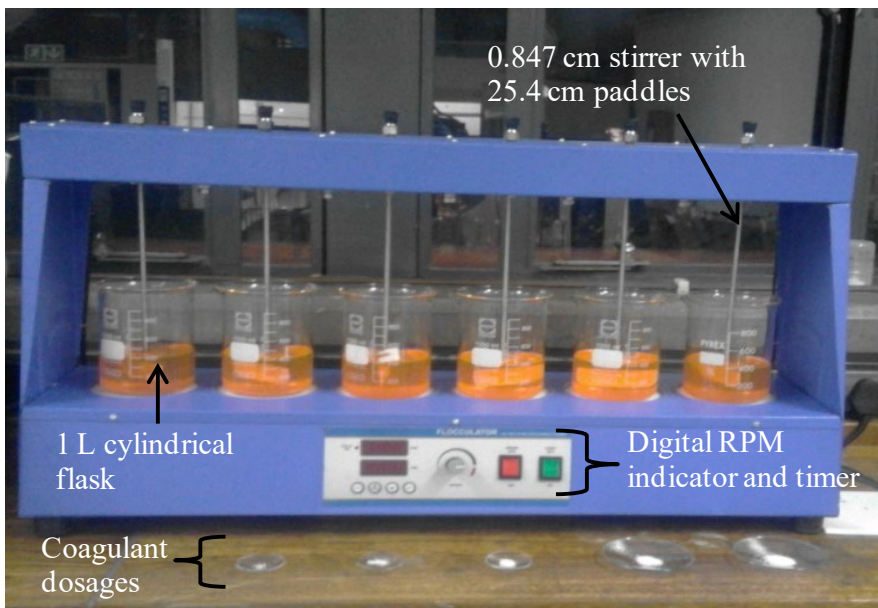


Figure 4.1. Jar test apparatus



A 600 mL pyrex jar filled with 400 mL working volume of slurry, placed on a magnetic stirrer was used in conducting EC experiments (Fig. 4.2). The agitation rate was kept at 250 rpm (Hussin et al., 2017). All the EC experiments were operated at galvanostatic conditions, in a batch mode and at an ambient temperature (Chafi et al., 2011). The inactive parts of the electrodes were covered with a parafilm to maintain the total effective electrode surface area of  $6\text{ cm} \times 5\text{ cm} \times 0.07\text{ cm}$ . Furthermore, the electrodes were cleaned after each process by immersion into 0.01M HCl for 2 min then rinsed with distilled water. The electrode were air dried and weighed before and after each use (Chafi et al., 2011).

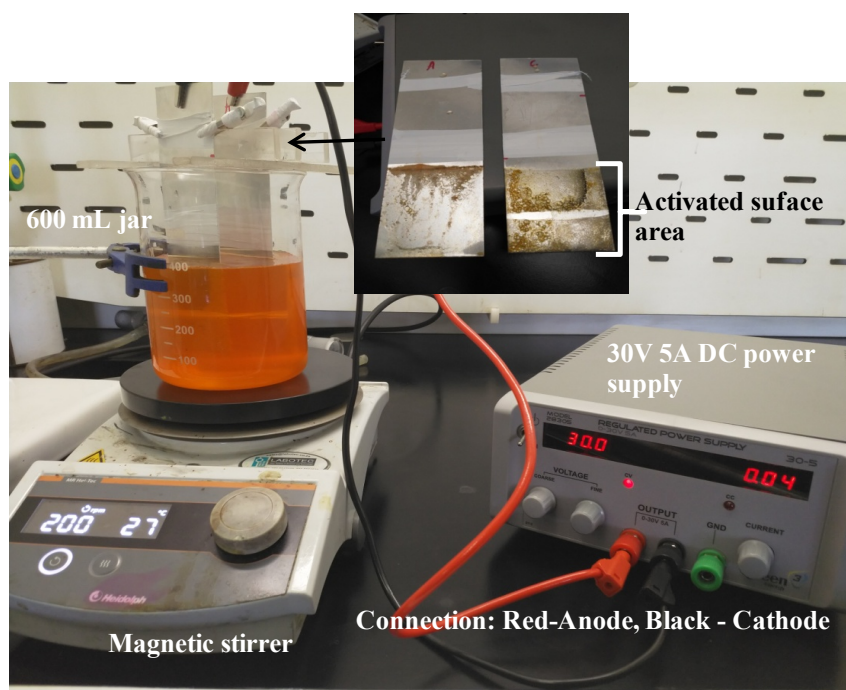


Figure 4.2. EC experimental setup

#### 4.2.2 Preparation of the synthetic effluent

An amount of 125.00 mg of orange II dye, 1332.14 mg of zinc salt and 199.81 mg of lead salt was added to 2.5 L of deionised water. A sample calculation used to determine the amount of salt to add to achieve 50 ppm of  $\text{Pb}^{2+}$  is as follows;

$$\begin{aligned} \frac{\% \text{wt of } \text{Pb}^{2+} \text{ in } \text{Pb}(\text{NO}_3)_2}{M_w(\text{Pb})} &= \frac{\% \text{wt of } [\text{Pb}^{2+}] \text{ ppm in } \text{Pb}(\text{NO}_3)_2}{[\text{Pb}] \text{ ppm}} \\ \frac{207.2}{331.2} &= \frac{50}{[\text{Pb}(\text{NO}_3)_2] \text{ ppm}} \end{aligned}$$

$$\therefore [\text{Pb}(\text{NO}_3)_2] \text{ ppm} = 79.92 = 199.81 \text{ mg added to 2.5 L Deionised H}_2\text{O}$$

The mixture was stirred until 100% pollutant dissolved. The remainder of the sample was contained and stored according to method 1060 B.4 and 1060 C respectively (Association & Association, 1989).



### 4.2.3 Chemical coagulation optimization

#### 4.2.3.1 Optimum coagulant dosage determination

The concentration of metal ions added as coagulants are shown in Table 4-2. Jar #1 was used as control as well as means of studying the effluent on its own without the addition of the coagulant. The concentration of coagulant was varied from 600-3200 ppm Alum and 200-1200 ppm iron chloride. In addition to coagulant optimum dosage studies, settling rate was also determined; where the samples were allowed to settle for 30, 60, 90 and 120 min.

Table 4-2: Coagulant dosages

| Jar no. | [I of Al <sup>3+</sup><br>desired (ppm) | Mass of Al salt<br>added (g) | [I of Fe <sup>3+</sup><br>desired (ppm) | Mass of Fe salt<br>added (g) |
|---------|---|------------------------------|---|------------------------------|
| 1       | -                                       | -                            | -                                       | -                            |
| 2       | 50                                      | 0.254                        | 50                                      | 0.097                        |
| 3       | 100                                     | 0.507                        | 100                                     | 0.194                        |
| 4       | 150                                     | 0.761                        | 150                                     | 0.290                        |
| 5       | 200                                     | 1.014                        | 200                                     | 0.387                        |
| 6       | 250                                     | 1.268                        | 250                                     | 0.484                        |

#### 4.2.3.2 Effect of initial pH of the slurry on pollutant removal

The pH studies were carried out using optimum coagulant dosage and setting time determined in the study above. The pH was varied from 4-11 in a manner shown in a Table 4-3.

Table 4-3: pH variations

| Jar no. | pH                     |
|---------|------------------------|
| 1       | Original slurry pH = 5 |
| 2       | 4                      |
| 3       | 6                      |
| 4       | 7                      |
| 5       | 8                      |
| 6       | 11                     |

## 4.3 RESULT AND DISCUSSION

### 4.3.1 Simulated wastewater characterisation

Table 4-4 shows the characteristics and behaviour of the simulated wastewater. Figure 4.3 presents of the coagulation as follows: The settleability of the bulk sample was very low with the maximum % dye removal of 14% after 2h. In a similar manner the Pb and COD removal was also low with percentages of 9.43 and 26.32 respectively. The results also showed that the pH of the sample does not change over time and even under agitation. Filtering (0.22µm pore size), however, effectively removes the turbidity with highest removal determined after 30 min to be 99.86%. Filtering was also able to remove 18% dye, 24% COD and 8.5% Pb without any treatment to the bulk sample.

Table 4-4: Bulk sample characteristics (no dilution)

| pH   | Conductivity<br>( $\mu\text{S}/\text{cm}$ ) | Dye $\lambda_{\text{max}}$<br>(nm) | Color  | Color intensity<br>(ppm) | COD (mg $\text{O}_2/\text{L}$ ) | Turbidity<br>(NTU) | Pb conc.<br>(ppm) | T ( $^{\circ}\text{C}$ )         |
|------|---|------------------------------------|--------|--------------------------|---------------------------------|--------------------|-------------------|----------------------------------|
| 5.78 | 1333  | 483                                | Orange | 39.80                    | 76.00                           | 235                | 20.65             | Ambient T ( $^{\circ}\text{C}$ ) |

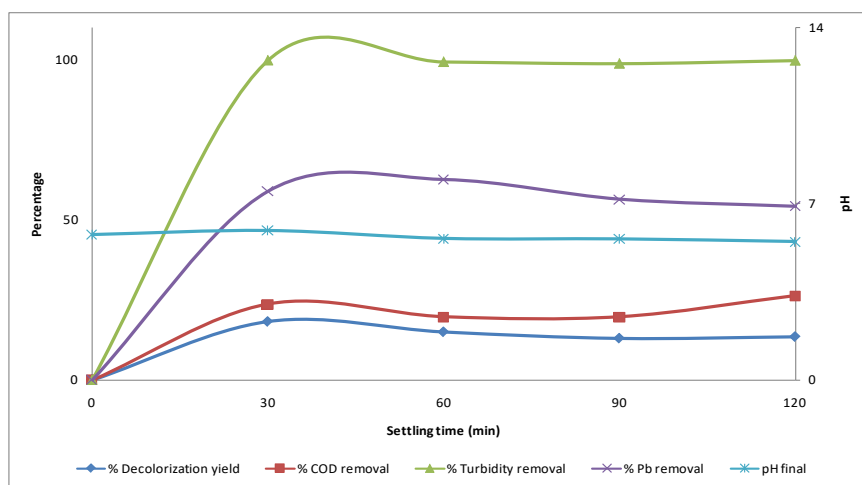


Figure 4.3. Bulk sample characterisation over time

#### 4.3.2 Chemical coagulation using alum as a coagulant

The optimum coagulant dosage was found to be 634.06 ppm (50 ppm Al ions) as presented in Fig. 4.4a. At this dosage the decolourisation yield went from 14% in 2h to 24% in 1 h. Addition of more coagulant increased the dissolved solids and had little impact in the removal of pollutants. The lowest % dye removals were obtained at coagulant dosage of 3170.29 ppm (250 ppm Al ions) at 2% after an hour.

In a similar manner for the dye removal, the optimum coagulant dosage was also determined at 50 ppm Al ions. The acceptable Pb removal was obtained after 60 min of settling at 75%. Contrary to the dye removal, increment of coagulant dosage, from 50 ppm Al ions to 250 ppm Al ions, to the wastewater, increased the removal of Pb to 82% after 1 h of settling (Fig. 4.4b).

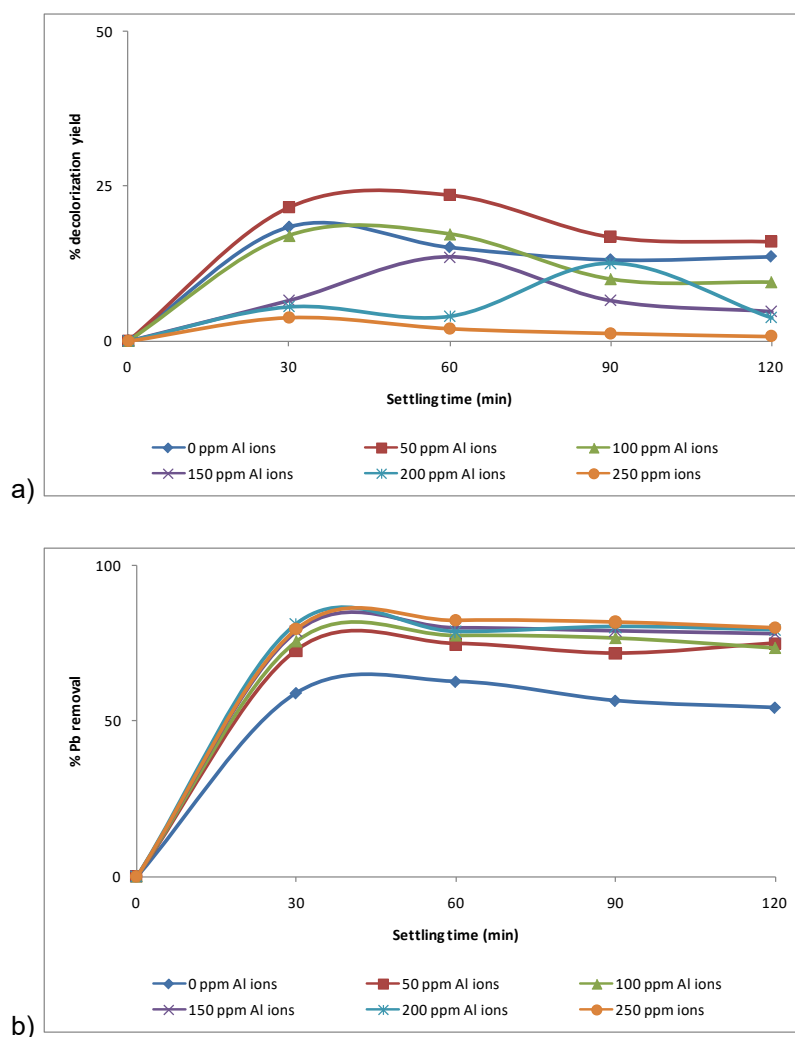


Figure 4.4. a) Optimum coagulant dosage and settling time determination. b) Pb removal at different settling times and coagulant dosage

COD obtained at optimum coagulant dosage (50 ppm Al ions) was 56 ppm (26% removal). At higher coagulant dosage COD increased above the bulk reading, i.e. at 150 ppm (Al ions) COD increased by 30% from the bulk solution to 99 ppm. This is presented in Fig. 4.5a.

Figure 4.5b shows results on turbidity. The turbidity of the samples at different coagulant had similar readings with the filtered bulk, with values above 90%. The addition of coagulants had no significant effect on the turbidity removal of the sample.

Increasing the pH of the increased the removal of pollutants tremendously (Fig. 4.5c). At pH 11, the removal of dye, Pb, COD, was at 91, 78, and 75% respectively. This proved that the CC process is pH dependant and heavy metal containing wastewaters favour the basic conditions for the efficient removal. Turbidity removal still remained above 90% at different initial pH of the bulk sample.

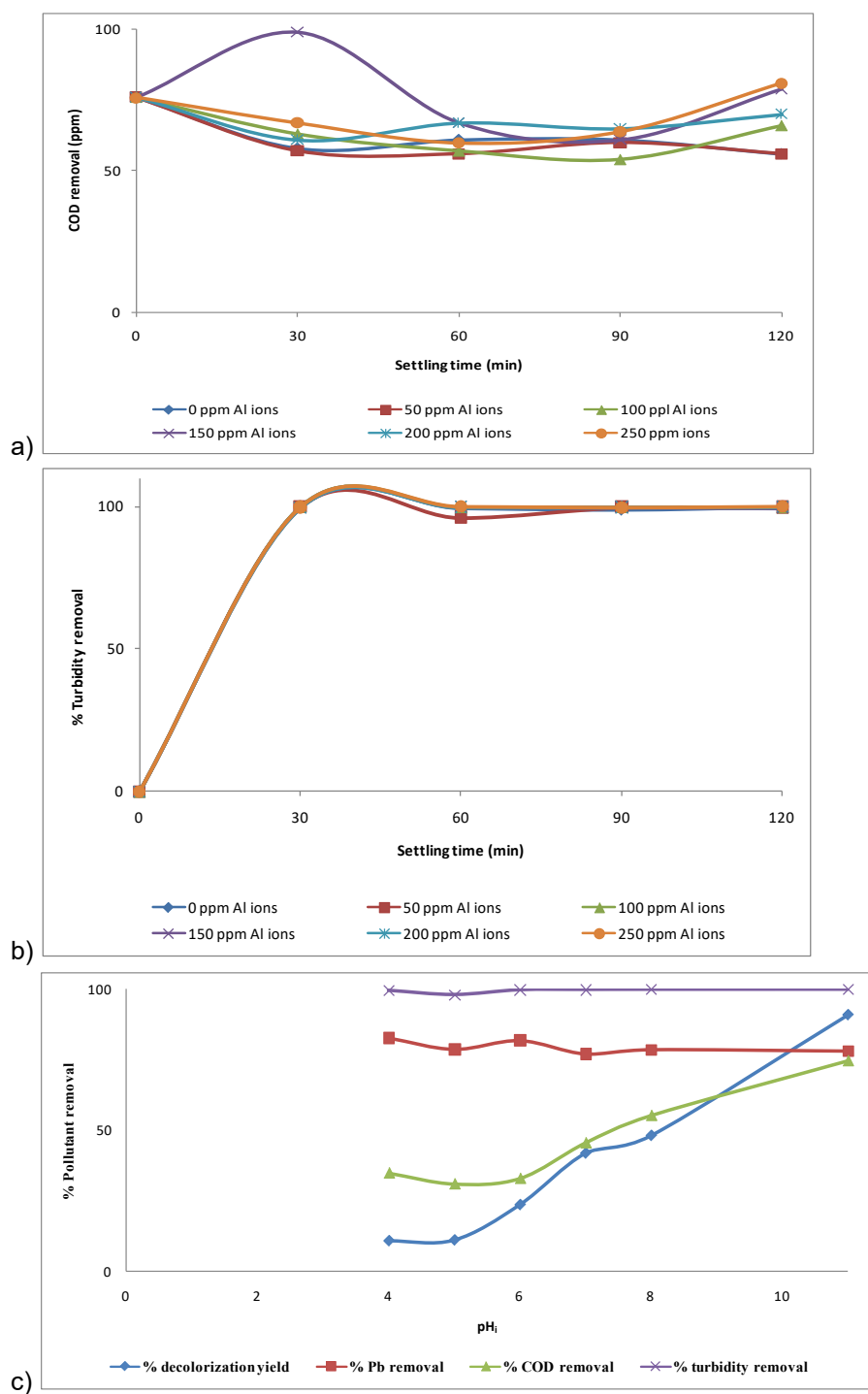


Figure 4.5. a) COD removal at different settling times and coagulant dosages. b) Turbidity removal at different settling times and coagulant dosage. c) Effect of initial pH of the bulk sample (Experimental conditions: Dye [] = 38.4 ppm, Pb [] = 25.51 ppm, COD [] = 103 ppm, turbidity of 207 NTU and settling time = 1 h)

### 4.3.3 Electrocoagulation experiments

#### 4.3.3.1 Electrocoagulation using Al-Al electrodes

EC, after 30 min of operation removed 92.78, 90.23, 41.79, and 99.21% of dye, COD, Pb and turbidity respectively (Fig 4.6a). The samples were allowed to settle for 30-120 min at an interval of 30 min. The change in the pollutant removal was insignificant, hence in the further studies, samples will be collected immediately after  $t_{EC}$ . The removal of dye, COD, Pb and turbidity changed to 93.3, 92.48, 39.69, and 99.9% after 2 h of settling respectively. The filtration, however, was easier after allowing the sample to settle for 2 h. A typical change in colour during EC is shown in Fig. 4.6b. The operation cost for this system was R 146.58/  $m^3$  of simulated wastewater.

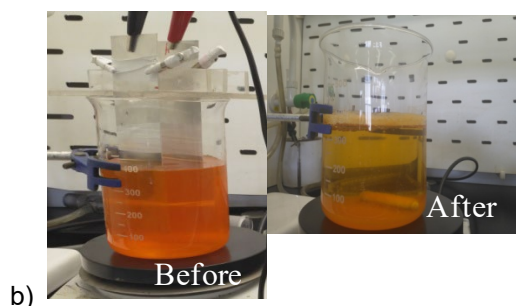
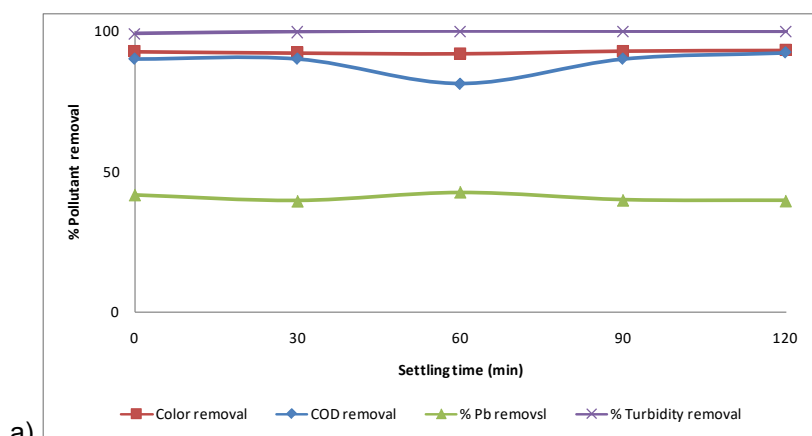


Figure 4.6. a) EC using Al-Al electrodes (Experimental conditions: Voltage 30 V. Current density = 0.65 mA/  $cm^2$ , inter-electrode spacing = 3.3 cm,  $t_{EC}$  = 30 min). b) Visual change of colour before and after treatment (EC using Al-Al electrodes)

#### 4.3.3.2 Sub conclusion on CC vs EC

Optimum coagulant dosage and settling time after treatment for a sample containing 39.8 ppm orange II dye, 76 ppm COD, turbidity of 207 NTU and 20.65 ppm Pb was 634.06 ppm and 1 h. CC is a pH dependant process, an initial pH of 11 was found to be the optimum. EC is more efficient in colour removal as compared to CC for the same concentration of pollutants.

#### 4.4 THE APPLICATION OF SS 316L AND SS 304 ELECTRODES IN ELECTROCOAGULATION FOR THE TREATMENT OF SIMULATED WASTEWATER: A COMPARATIVE STUDY.

**Abstract.** In this study, electrocoagulation was applied for the treatment of wastewater containing 50 ppm of orange II dye and Pb. Performance of aluminium plates was compared with stainless steel of grade 316L and 304 at the same operating parameters and simulated wastewater working volume of 400 mL. The effect of initial conductivity (3.8 -16.8 mS/cm), current density (1.6-16.3 mA/cm<sup>2</sup>) and  $t_{EC}$  (10-30 min) on the removal of pollutant efficiency and operation costs were investigated. Increase in conductivity hindered the COD removal, however had an effective removal of Pb and orange II dye, with removal efficiencies of greater than 90% for all electrode materials. It was established that SS 304 can rapidly remove Pb content as compared to SS 316. After 10 min of electrolysis at a current density of 1.6 mA/cm<sup>2</sup>, and an initial conductivity of 3.8 mS/cm, 96.6%, 49.8% and 67.5% of Pb was removed using SS 304, SS 316 and Al electrodes respectively. Both SS electrodes showed rapid removal of colour at percentages > 90% after 10 min of operation. In addition, at these conditions SS 316 showed to be slightly cheaper than SS 304 electrodes at R 280.4/ m<sup>3</sup> and R291.9/m<sup>3</sup> respectively.

#### 4.5 METHODOLOGY: COMPARATIVE STUDY

##### 4.5.1 Materials

Orange II dye was used to impact colour in the synthetic effluent. Heavy metal salt that was used for metal addition in the simulated wastewater was lead (II) nitrate (Pb(NO<sub>3</sub>)<sub>2</sub>). Sodium chloride (NaCl) was used to increase the conductivity of the sample. 0.01 M HCl was used in the cleaning of electrodes before and after each experiment. All reagents were of analytical grade, purchased from Sigma Aldrich, Germany, and they were used without further purifications.

##### 4.5.2 Analytical measurements

Decolourisation of the dye was investigated using UV-Visible spectrophotometer at maximum absorption wavelength of 483 nm (Cary 60, Agilent technologies, Australia). Atomic absorption spectrometry (AAS CS1330) was used to analyse the Pb concentration before and after each experiment. For the measurement of dye and Pb removal a linear calibration curve in the range of 0-50 ppm was set up based on absorbance measurements. The correlation factor ( $R^2$ ) for the calibration curves was 0.9998. The simulated wastewater turbidity was measured using a portable Aqua Lytic turbidimeter AI250T-IR with features ranging from 0.01 to 1100 NTU. The chemical oxygen demand (COD) was measured with a HACH digester (150°C for 2 h), using digesting solutions of HR (0-1500 ppm) and a HACH spectrophotometer (Model DR/4000). pH was measured using Ohaus ST 10 pen pH meter and C6 µS/ TDS was used to determine the conductivity of the samples. The degree of decolourisation and metal removal was determined using the formula shown below.

$$\text{Pollutant removal (\%)} = \frac{C_o - C_t}{C_o} \times 100 \dots \dots \dots (1)$$

Where;  $C_0$  is the initial concentration of the pollutants and  $C_t$  is the pollutant concentration after treatment in mg/ L. The density of the simulated wastewater was assumed to be equal that of water at 1000 kg/m<sup>3</sup>.

#### 4.5.3 Experimental

A 600 mL pyrex jar was filled with 400 mL working volume of simulated wastewater, placed on a magnetic stirrer was used in conducting EC experiments. Model 28305 regulated DC power supply (30V 5A) was used as a power source. Electrodes (dimensions; 15 cm × 5 cm × 0.07 cm) that were used are aluminium (alloy - temper: 1050 - H14, 99.5% purity) and stainless steel (SS) (304 and 316 L).

The inactive parts of the electrodes were covered with a parafilm to maintain the total effective electrode surface area of dimensions; 6 cm × 5 cm × 0.07cm. The agitation rate was kept at 250 rpm (Hussin et al., 2017). All the EC experiments were operated at galvanostatic conditions, in a batch mode and at an ambient temperature (Chafi et al., 2011). Furthermore, the electrodes were cleaned after each process by immersion into 0.01M HCl for 2 min then rinsed with distilled water. The electrodes were air dried and weighed before and after each use (Chafi et al., 2011). The amount (in grams) of anode consumed after each run and the amount of electrical energy was determined using formulae 2 and 3 shown below.

$$C_{electrode} \left( \frac{kg}{m^3} \right) = \frac{I \times t_{EC} \times M_w}{z \times F \times V} \dots \dots \dots (2)$$

Where,  $C_{electrode}$  is the consumption of metal electrode in kg/m<sup>3</sup>,  $I$  is the current (A),  $M_w$  is the molecular of the electrode material (g/mol),  $z$  (unitless) is the number of transferred electrons (e.g. for Al electrode,  $z = 3$ ),  $t_{EC}$  is the treatment time (s),  $F$  is Faraday's constant (96 487 C/mol) and  $V$  is slurry volume (m<sup>3</sup>).

$$C_{energy} \left( \frac{kWh}{m^3} \right) = \frac{U \times I \times t_{EC}}{V} \dots \dots \dots (3)$$

Where;  $C_{electrodes}$  is the energy consumption in kWh/m<sup>3</sup>,  $U$  is the voltage (V),  $I$  is the current (A),  $t_{EC}$  is the treatment time (h) and  $V$  is the volume of the aqueous solution (m<sup>3</sup>).

#### **EC on simulated wastewater**

Simulated wastewater with a conductivity of 3.8 mS/cm was electrocoagulated using two Al metal sheets (both as anode and cathode) with inter-electrode spacing of 3.3 cm. The initial electrolysis time ( $t_{EC}$ ) was kept at 30 min. An amount of treated wastewater was withdrawn immediately using a syringe and filtered using a 0.22 µm pore size filtering disc and analysed. In a similar manner EC was performed on bulk as is, using SS 316L as both cathode and anode, then SS 304.

#### **Effect of initial conductivity of simulated wastewater on pollutant removal**

The conductivity of the simulated wastewater was varied by adding sodium chloride (NaCl) at different concentrations from 2 g/L to 10 g/L. The conductivity of the simulated wastewater was therefore increased from 3.8 mS/cm to 17 mS/cm. the current density was kept constant at 0.65 mA/cm<sup>2</sup>.

#### **The effect of current intensity**

Studies have shown that the applied current density is an important parameter in EC as it determines coagulant dosage rate, the bubble production rate and the floc growth and size (Khandegar & Saroha, 2013; Oncel et al., 2013). In this study, current densities was varied from 0.65-16.2 mA/ cm<sup>2</sup> by increasing the current, whilst other operating conditions (initial pH and operating time) were kept constant.

### **Operating time determination ( $t_{EC}$ )**

Effect of operating time, was determined by varying electrolysis time from 10-30 min at 5 min interval and measuring the removal of pollutants from synthetic effluent at a current density of 8 mA/cm<sup>2</sup>.

### **Operating costs determination**

Optimisation of operating costs plays an important role in EC process. The cost of operation was determined using formula 4 below.

$$\text{Operating cost } \left( \frac{R}{m^3} \right) = aC_{\text{energy}} + bC_{\text{electrode}} \dots \dots \dots (4)$$

Where; a represents the 2017-2018 electricity price in South Africa (97.03 R/kWh), b represents the 2017 retail metal sheets (Al = 67.88 R/kg).

## **4.6 RESULTS AND DISCUSSION**

### **4.6.1 Effect of initial conductivity on pollutant removal and corresponding operational costs**

It is important to study the effect of initial conductivity because it affects the energy consumption and subsequently the cost of operation. Figure 4.7 shows the effect of initial conductivity on colour, Pb, COD removal and an estimated cost of operation with applied voltages related for the 3 materials of electrodes investigated. An increase in conductivity of the simulated wastewater had an insignificant effect on the removal of orange II dye with highest removal of greater than 90% for all the electrodes materials at different conductivities. A 91.6%, 96.6% and 96% of dye was removed after 30 min of operation by application of Al-Al, SS 316-SS 316 and SS 304-SS 304 respectively at a conductivity of 3.8 mS/cm (Fig. 4.7a). It was also observed that at operating conditions provided, stainless steel electrodes performed better than aluminum electrodes and SS 304 and SS 316 had similar removal yields.

For Al electrodes, increase in conductivity resulted in the decrease in Pb removal efficiency, with a decrease of 13.6% at a conductivity of 16.8 mS/cm from the 65.3% obtained at 3.8 mS/cm (Fig. 4.7b). SS 304 electrodes were able to remove over 90% whereas SS 316 removed 72.3% at a conductivity of 3.8 mS/cm. The two SS electrodes behaved differently during the removal of Pb. Higher conductivities favoured the removal of Pb using SS 316 as anode and cathode with the removal of 90.7% at 16.8 mS/cm as compared to SS 304 with a removal 73.0% at the same conductivity. It was observed that the addition of NaCl for conductivity increase resulted in COD removal hindrance (Fig. 4.7c). For aluminium and SS 316 electrodes, the COD increased from the initial COD at conductivities greater than 3.8 mS/cm. SS 304 electrodes were able to remove 55.6% of COD at a conductivity of 16.8 mS/cm.



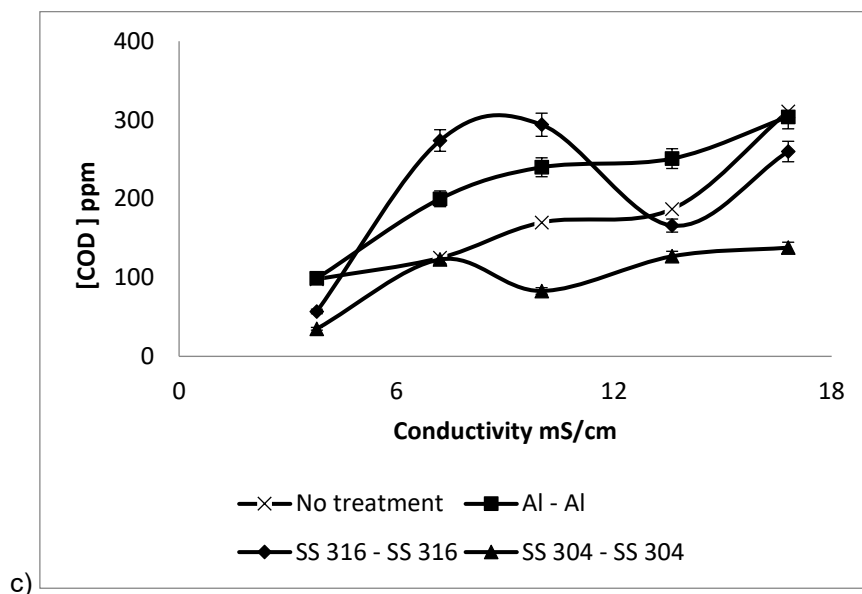
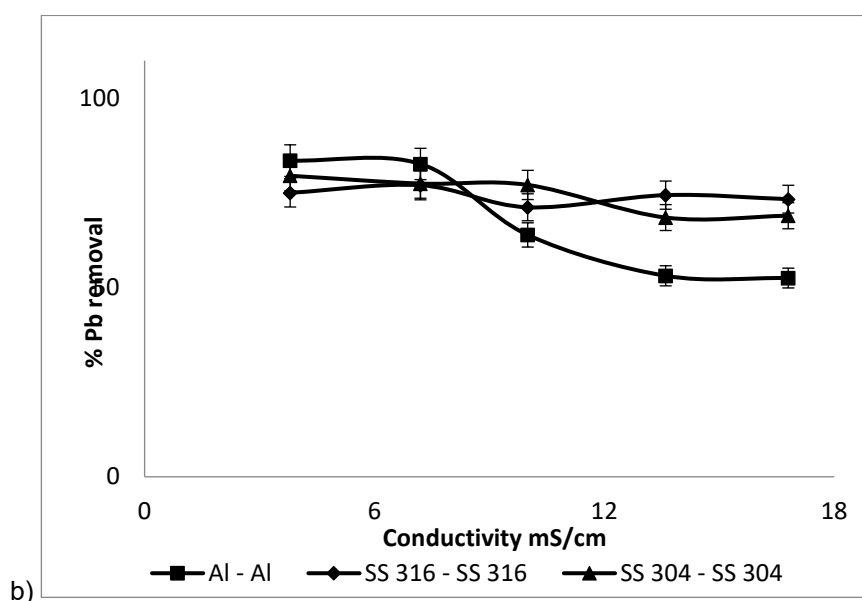
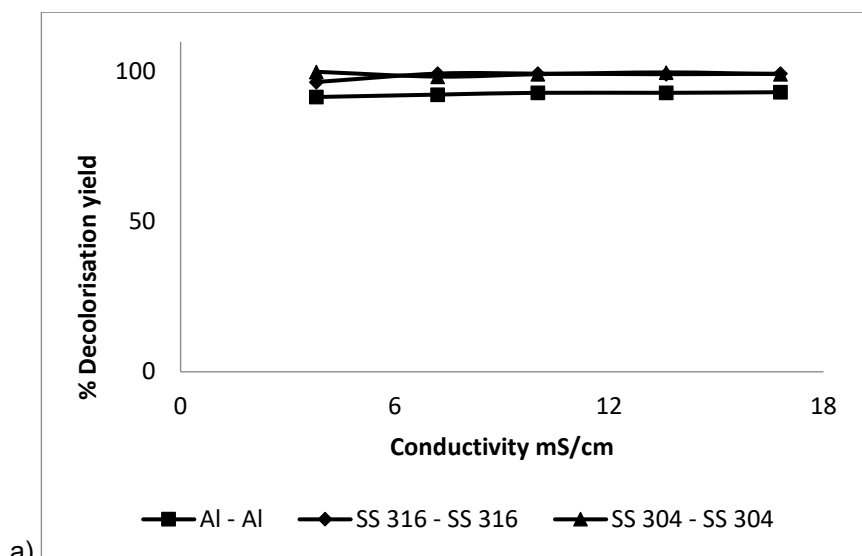


Figure 4.7. At operating parameters:  $i = 0.65 \text{ mA/cm}^2$ ,  $t_{EC} = 30 \text{ min}$ , inter-electrode spacing = 3.3 cm: a) Removal of orange II dye as function of initial conductivity of sample. b) Removal of Pb as function of initial conductivity of sample. c) Removal of COD as function of initial conductivity of sample.

At a conductivity of 3.8 mS/cm voltage that was applied to maintain a current density of 0.65 mA/cm<sup>2</sup> was 2.2V for aluminium electrodes and 3.2V for both SS 304 and SS 316 electrodes. The corresponding estimated cost at this conductivity was, R11.8/m<sup>3</sup>, R20.6/m<sup>3</sup> & R18.0/m<sup>3</sup> for aluminium, SS 316 and SS 304 electrodes respectively. As expected, the higher the conductivity of the sample the lower voltage is required to achieve a current density of 0.65 mA/cm<sup>2</sup>. This results in the reduction in operational costs for all electrode materials as the energy cost is reduced significantly. In addition, aluminium electrodes were cheaper to use at different initial conductivities of the simulated wastewater.

Contrary to the little effect that the increment in initial conductivity of bulk had on the pollutant removal at constant applied current density, the operational costs were decreased tremendously. The lowest operational cost was calculated to be R6.67 / m<sup>3</sup> of slurry at the highest conductivity of 16.8 mS/cm. This was attributed to the fact that less energy ( $C_{\text{energy}}$ , equation 3) was required to obtain the current density of 0.65 mS/ cm<sup>2</sup>.

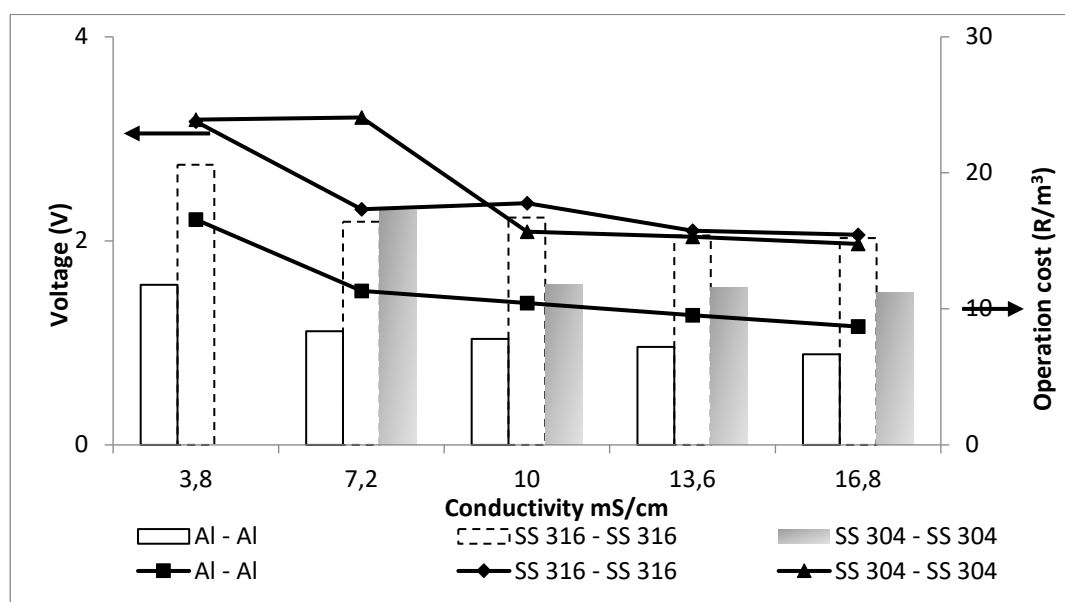


Figure 4.8. Voltage variation at different initial conductivities and Operational costs in (R/m<sup>3</sup>)

#### 4.6.2 Effect of current density on pollutant removal

In this study the experiments were carried out on the simulated wastewater with a conductivity of 3.8 mS/cm. Figures 4.9-4.11 show the effect of current density on the removal of colour, Pb and COD, the estimated operational cost associated with different current densities and the anode mass loss in the 30 min of operation for different material of electrodes respectively.

Increase of current density from 1.6 to 16.3 mA/cm<sup>2</sup> had a significant effect on the removal of orange II dye from the simulated wastewater for different electrode materials (Fig. 4.9). The decolourisation yield increased by 5.6%, 0.8% and 0.2% for aluminium, SS 316 and SS 304 electrodes respectively at a current density of 1.6 mA/cm<sup>2</sup> from 0.65 mA/cm<sup>2</sup>. As the current density increased, there was no significant change in the decolourisation yield.

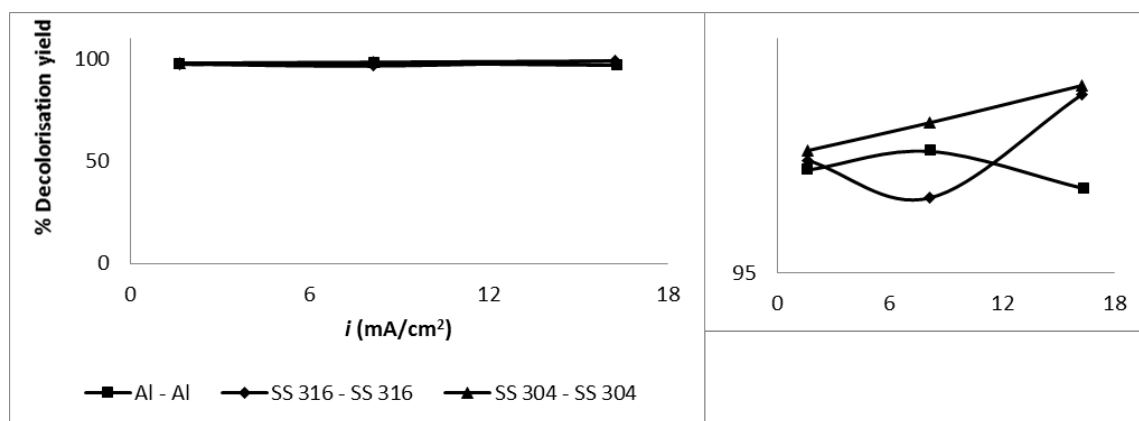


Figure 4.9. Effect of current density on decolourisation yield (Operating parameters:  $t_{EC} = 30$  min,  $k = 3.8$  mS/cm). Graph 2 is an expansion from 95%.

Lead removal increased to 89.5% as the current density was increased to 16.3 mA/cm<sup>2</sup> when using the aluminium electrodes (Fig. 4.10). It was also noticed that at different applied current densities, SS 304 and SS 316 behaved in a similar manner, where the Pb removal was increased to 97.7% at the same current density of 16.3 mA/cm<sup>2</sup>.

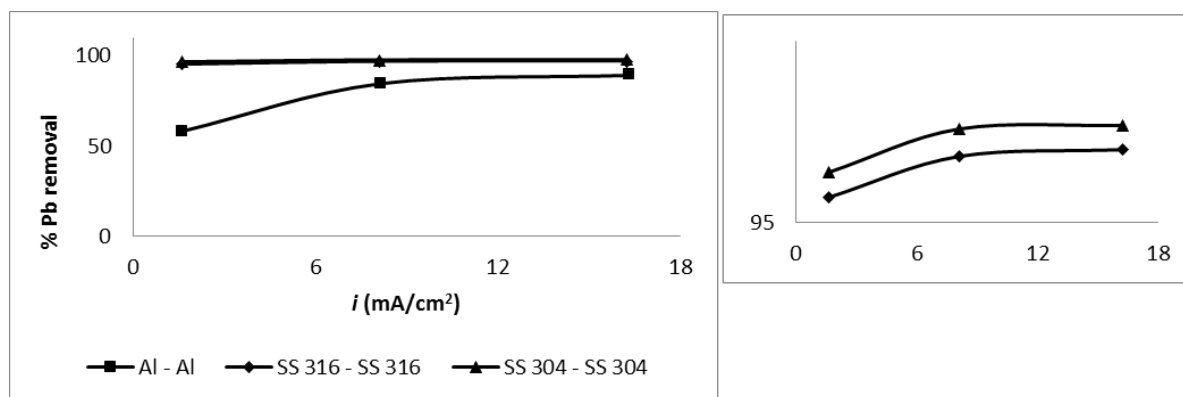


Figure 4.10. Effect of current density on Pb removal (Operational parameters:  $t_{EC} = 30$  min,  $k = 3.8$  mS/cm)

For all the electrode materials, there was a significant removal of COD at higher current densities. At 1.63 mA/cm<sup>2</sup>, the COD removal was 34.7%, 37.8% and 54.1% for aluminium, SS 316 and SS 304 electrodes respectively (Fig. 4.11). It was established, however, that the current density increased above the 1.63 mA/cm<sup>2</sup> caused a decrease in the removal of COD. This may be due to the overdosing of the coagulant, increasing the inorganic species (TSS) in the simulated wastewater.

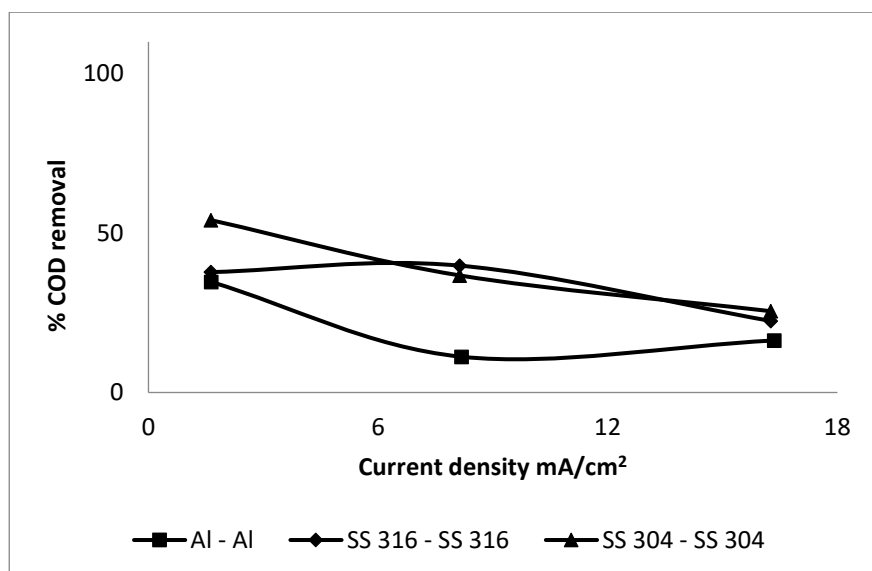


Figure 4.11. Effect of current density on COD removal (Operational parameters:  $t_{EC} = 30$  min,  $k = 3.8$  mS/cm)

**Effect of current density on OC including mass loss of electrodes.** As can be expected, the higher the current density, the more estimated operational costs. This is due to the energy requirement cost increase. SS 304, even though cheaper than SS 316 had the highest costs at a current density of  $16.3 \text{ mA/cm}^2$  at  $3364.3/\text{m}^3$  (Fig. 4.12a).

The mass loss of the electrodes (Fig 4.12b) is in accordance with Faradays Law, the more energy applied, the more the sacrificial anode corrodes/dissolves.

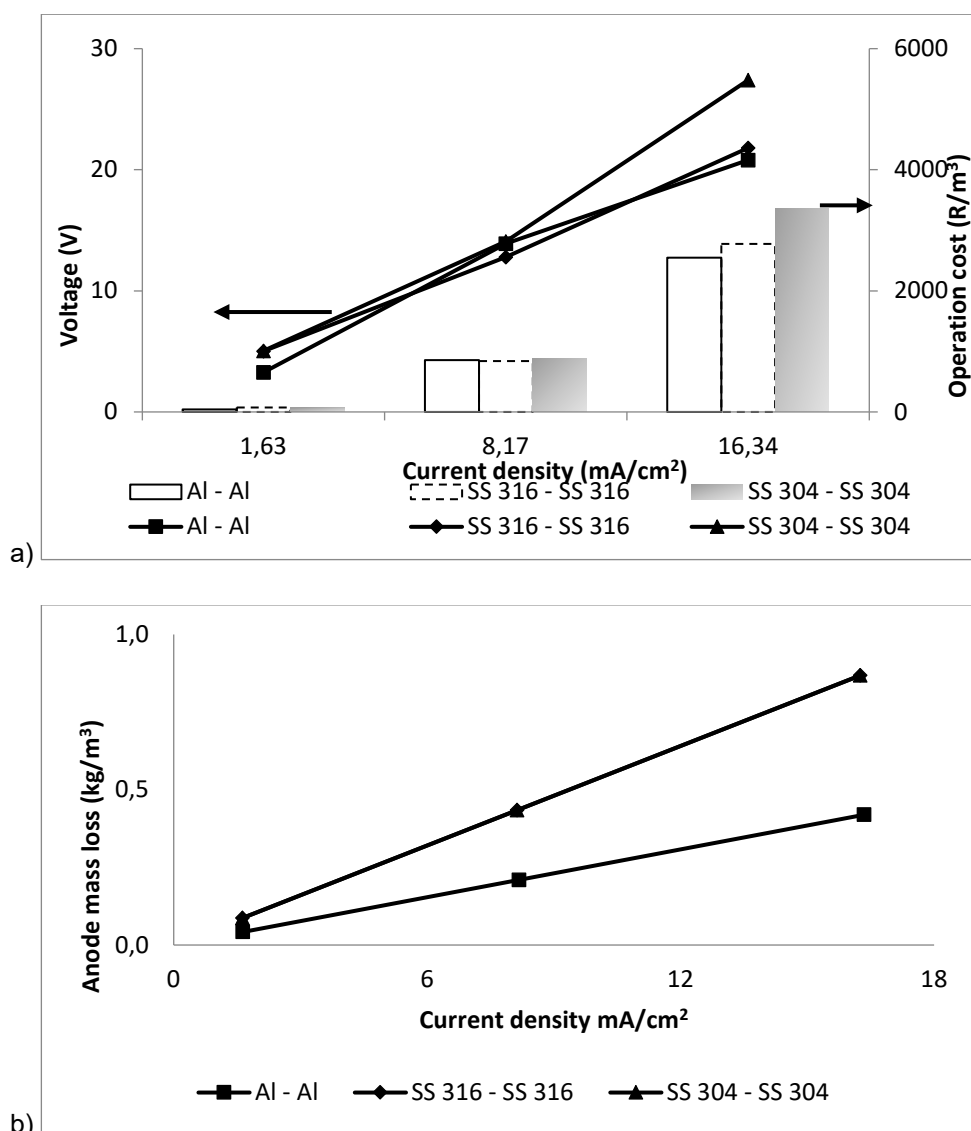


Figure 4.12. a) Voltage variation at different current densities and Operational costs in (R/m<sup>3</sup>). b) Effect of current density on electrode consumption (Operational parameters:  $t_{EC} = 30$  min,  $k = 3.8$  mS/cm)

#### 4.6.3 Electrocoagulation time studies ( $t_{EC}$ )

The study of electrolysis time effect on pollutant removal was carried out at a current density of 8.2 mA/cm<sup>2</sup> and an initial conductivity of 3.8 mS/cm. Figure 4.13 shows the removal of colour and Pb as a function of  $t_{EC}$  and the corresponding estimated operational cost with the mass loss of the sacrificial anode at a given time of the treatment for different material of electrodes respectively.

**Decolourisation** (Fig 4.13a). These results clearly show that, there is a rapid removal of orange II dye in the first 10 min of the process for all the electrode materials. The percentages of the dye that was removed in 10 min are 81.2%, 89.4% and 88.2% for aluminium, SS 316 and SS 304 electrodes respectively.

**Pb removal** (Fig. 4.13b). Aluminium and SS 316 showed similar pattern for the removal of Pb in the wastewater, where maximum Pb removed was obtained after 30 min of operation. SS 304, however, showed rapid removal of pollutants within 10 min of operation, where 96.6% of Pb was removed at the 10 min mark.

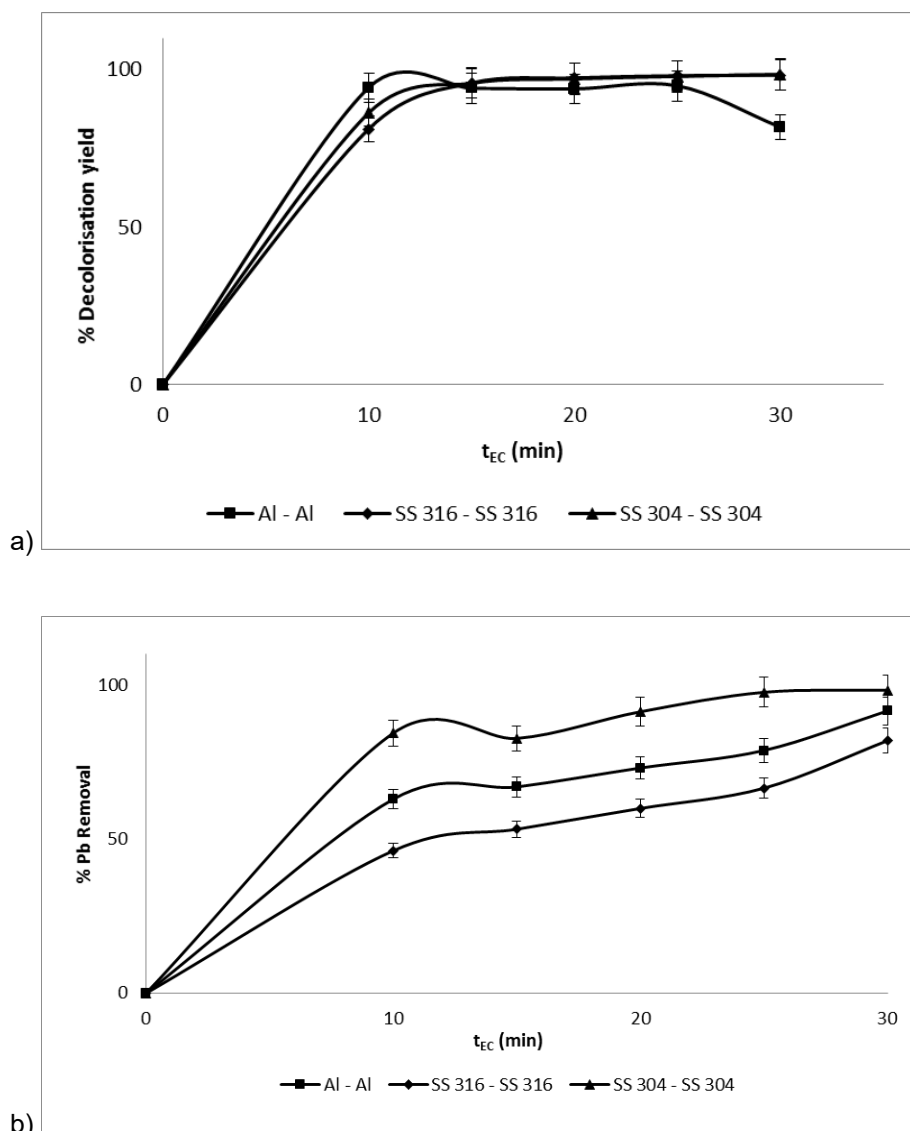


Figure 4.13. a) Effect of electrolysis time on the decolourisation yield. b) Effect of electrolysis time on the removal of Pb (operating parameters:  $i = 8 \text{ mA/cm}^2$ ,  $k = 3.8 \text{ mS/cm}$ )

#### 4.6.4 Sub Conclusion

Electrocoagulation on simulated wastewater containing initial concentration of orange II dye and Pb of 50 ppm using different types of electrodes showed positive results. In comparison of Al electrodes and both SS grades, SS had better pollutant removal efficiencies at different initial conductivities of simulated wastewater, applied current density and  $t_{EC}$  studies, however costs higher than Al electrode material. SS 316 and SS 304 showed different removal of pollutants properties at the same operating conditions. In conductivity studies, SS 316 and SS 304 decolourisation yields of 96.6% and ...as opposed to 91.6% yield when using Al electrodes at the lowest conductivity of 3.8 mS/cm and 30 min of operation. In addition, highest Pb removal was obtained at a conductivity of 16.8 mS/cm at 90.7% whereas SS 304 was....For wastewaters containing higher concentrations of electrolyte (higher conductivities) higher current densities are required for the removal of COD for the three electrode materials investigated. Current densities ranging from 1.63 to 16.3 mA/cm<sup>2</sup> had an insignificant effect on decolourisation yield and Pb removal for both SS materials. SS 304 removed 54.1% of COD at 1.63 mA/cm<sup>2</sup>, whereas SS 316 had a removal percentage of 37.8% at the same current density. It was established that

SS 316 and SS 304 have different pollutant removal efficacies when applied in an EC system for wastewater treatment. Based on the results, it can be concluded that SS 304 is better in COD removal at different current densities and rapid removal of Pb as compared to SS 316 material.

## CHAPTER 5: PHOTOELECTROCHEMICAL SYSTEMS ON TITANIUM SHEET BASED PHOTOANODES FOR THE DEGRADATION OF DYE IN WASTEWATER

---

### 5.1 MOTIVATION

The PEC processes reported in chapter 3 were all based on the use of carbon materials exfoliated graphite and reduced graphene oxide – as supports for the preparation of the photoanodes. The carbon based photoanodes could not withstand high current densities owing to the tendency to oxidise the carbon materials. Furthermore, the electrodes were not so rigid and thus may not be amenable to machining in the fabrication of the envisaged flow-through reactor. These challenges motivated the use of a more rigid substrate – titanium sheet. The titanium metal sheet may be easier to work with in the development of the anodic chamber of photoelectrocatalytic cell.

### 5.2 INTRODUCTION

Photoelectrocatalytic process (PEC) has been indicated to hold promise for wastewater remediation and energy conversion (X. Zhang et al., 2017). In this technique electrical energy is applied to a photocatalytic system to obtain synergistic benefit. In the last few years, combining electrochemical process and photocatalysis has been shown to yield improved performance for organic pollutants degradation compared to either electro-oxidation or photocatalysis alone. This enhanced performance has been attributed to the ability of the applied bias potential to promote the separation of the photogenerated hole and electron pairs (Bessegato, Cardoso & Zaroni, 2015; M. G. Peleyeju & Arotiba, 2018; Moses G Peleyeju et al., 2017).

Photocatalysts which are sensitive in the visible region of the solar spectrum have received considerable attention as anodic materials for PEC. This is because utilising sunlight for the process promotes sustainability. For instance,  $\text{BiVO}_4$  and its composites have been used as photoanodes in PEC system for hydrogen production via water splitting and organic contaminants decomposition (Monfort et al., 2016; Monfort, Raptis et al., 2017; Monfort, Sfaelou et al., 2017a; Tolod, Hernández & Russo, 2017; Y. Zhou et al., 2017). Having a narrow band gap of 2.4 eV,  $\text{BiVO}_4$  is an ideal semiconductor for visible-light driven processes. It is non-toxic, stable to photocorrosion, inexpensive and can be obtained via simple synthetic routes (T. Ahmed, Zhang, Xu & Zhang, 2017). However, apart from the rapid recombination of electron-hole pairs (Malathi, Vasanthakumar, Arunachalam, Madhavan & Ghanem, 2017),  $\text{BiVO}_4$  also suffers from poor electrical conductivity and low adsorptive performance (He et al., 2013). These drawbacks make  $\text{BiVO}_4$  an inefficient photocatalyst for pollutants degradation. Studies have shown that photocatalytic/photoelectrocatalytic degradation of organic pollutants at pristine  $\text{BiVO}_4$  presented low removal efficiency (Geng, Zhang, Li & Sun, 2015; Shang et al., 2009; J. Sun et al., 2018; Y. Sun et al., 2012).

$\text{WO}_3$  (band gap, 2.5-2.8 eV) is another promising material for PEC. It is inexpensive, demonstrates low susceptibility to photocorrosion, exhibits appreciable stability in acidic and oxidative conditions, and is non-



toxic (Dong, Hou, Xi, Shao & Dong, 2017; Hilliard et al., 2017; Sfaelou, Pop, Monfort, Dracopoulos & Lianos, 2016). Importantly,  $\text{WO}_3$  is being explored as a potential photocatalyst for destruction of organic pollutants because of the high oxidation power of its valence-bound holes (Weng, Wu, Zhang & Xu, 2014). In spite of its impressive properties, the photocatalytic activity of  $\text{WO}_3$  is poor owing to its relatively low conduction band edge. The position of the conduction band edge is unfavourable for one-electron reduction of adsorbed oxygen molecules (Sakai et al., 2015). This leads to accumulation of photogenerated electrons, and their consequent recombination with the holes which are needed for oxidation of target compounds. As a result, improving the photocatalytic activity of  $\text{WO}_3$  by modifying its electronic structure has been the focus of many studies. It has been reported that tuning the morphology/structure of  $\text{WO}_3$  can yield a catalyst with enhanced charges separation and improved photoactivity (B. Ahmed, Kumar, Ojha, Donfack & Materny, 2017; Dirany et al., 2016; Dong et al., 2017; Huang et al., 2015; T. Zhang, Su & Guo, 2016). Theerthagiri et al., Zhang et al. and Yao et al., in separate studies, showed that  $\text{WO}_3$  nanorods possesses suitable physico-chemical properties for enhanced photocatalytic performance (Theerthagiri et al., 2015; Yao, Qu, Wang & Wu, 2017; J. Zhang et al., 2017).

Fabricating a hybrid of two or more semiconductors has been hinted as one of the plausible approaches to overcoming the challenges of electron and hole recombination and some other limitations associated with individual photocatalyst such as the low conduction band edge in  $\text{WO}_3$  and the poor charge mobility in  $\text{BiVO}_4$  (Ho-Kimura, Moniz, Handoko & Tang, 2014; Kim et al., 2014; S. Wang et al., 2017; Xia et al., 2016; Yuan et al., 2015). The resulting nanocomposite catalysts have been reported to display much higher activity than the individual materials. Xia et al. reported the oxidation of phenol on a  $\text{Fe}_2\text{O}_3/\text{BiVO}_4$  thin film anode via photoelectrocatalytic process (Xia et al., 2017). The composite photoanode demonstrated superior performance to the pristine  $\text{BiVO}_4$  anode. The authors attributed the enhanced degradation performance to the ultra-thin iron oxide which minimised charge carriers recombination in  $\text{BiVO}_4$ . In another report by Martins et al. (Martins, Nuñez & de Vasconcelos Lanza, 2017),  $\text{WO}_3$  modified  $\text{TiO}_2$  nanotube array (NTAs) exhibited better mineralisation efficiency than the unmodified  $\text{TiO}_2$  (NTAs) when both electrodes were employed for the photoelectrocatalytic degradation of the endocrine disrupting compound propyl paraben. Similarly, Wei et al. (Wei et al., 2017) reported that decontamination of coking wastewater containing phenolic compounds was much more efficient at heterostructured  $\text{TiO}_2/\text{g-C}_3\text{N}_4$  than at pure  $\text{TiO}_2$  and  $\text{g-C}_3\text{N}_4$ . The improvement in the photoelectrocatalytic efficiency was attributed partly to the heterojunction that is formed between the two photocatalysts which suppresses the recombination rate of electrons and holes.

In this work,  $\text{BiVO}_4$  has been modified with carbon nanoparticles and boron to obtain a photocatalyst denoted as  $\text{CNP/B-BiVO}_4$ . This catalyst was then coupled to  $\text{WO}_3$  nanorods and the resulting nanocomposite was immobilised on Ti plate. The photoanode,  $\text{CNP/B-BiVO}_4/\text{WO}_3$  was then employed for the catalytic oxidation of orange II dye. In this study we hypothesised that modification of  $\text{BiVO}_4$  with substances such as CNP and B would impact positively on the photocatalytic performance of the semiconductor. In addition, we envisaged that coupling this modified material to  $\text{WO}_3$  nanorods will provide a nanocomposite anode with desirable properties for photoelectrocatalytic applications.

### 5.3 METHODOLOGY

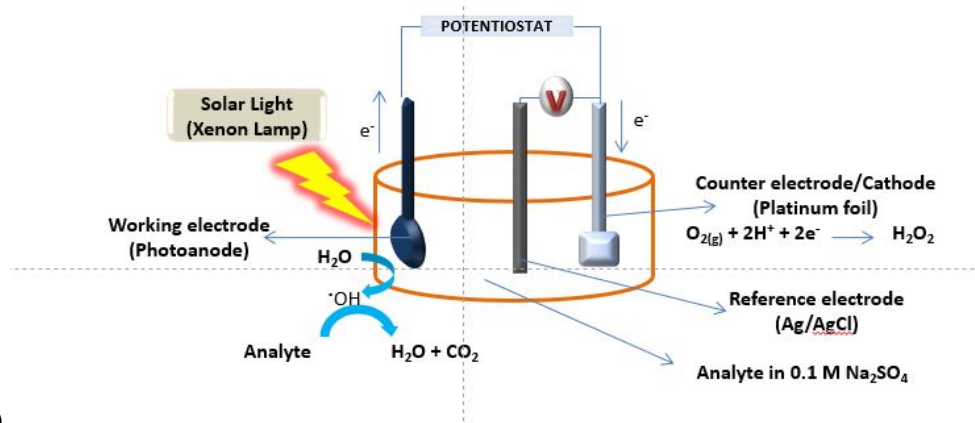
#### 5.3.1 Materials and Equipment

Sodium tungstate dihydrate ( $\text{Na}_2\text{WO}_4 \cdot 2\text{H}_2\text{O}$ ), bismuth nitrate pentahydrate ( $\text{Bi}(\text{NO}_3)_3 \cdot 5\text{H}_2\text{O}$ ), sodium metavanadate ( $\text{NaVO}_3$ ), sodium chloride ( $\text{NaCl}$ ), sodium sulphate ( $\text{Na}_2\text{SO}_4$ ), sodium hydrogen carbonate ( $\text{NaHCO}_3$ ), sodium hydroxide ( $\text{NaOH}$ ), orange II sodium salt, polyethylene glycol (PEG), boric acid ( $\text{H}_3\text{BO}_3$ ) and ethanol were purchased from Sigma-Aldrich South Africa. All solutions were prepared with deionised water.

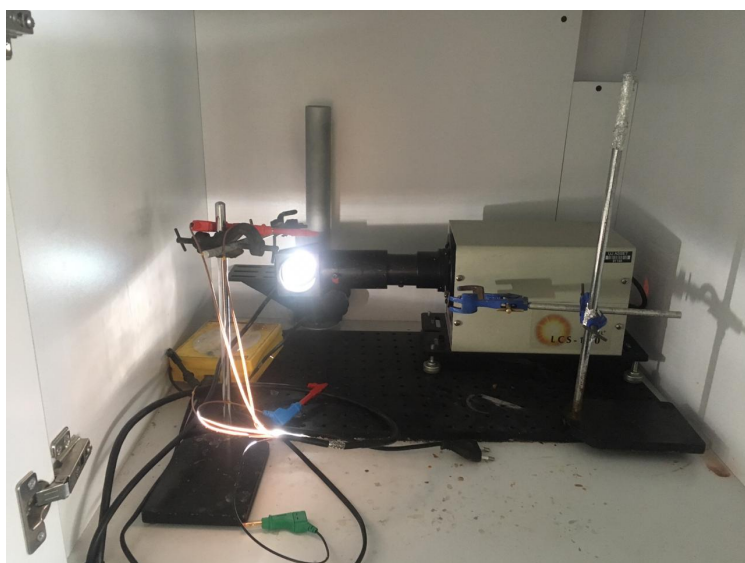
Powder x-ray diffraction analysis of the catalysts was done on Rigaku Smartlab x-ray diffractometer (USA) equipped with Cu  $\text{K}\alpha$  radiation and operated at 40 kV and 40 mA. The electron images were obtained on scanning electron microscope (TESCAN, Vega 3 XMU, Czech Republic) and transmission electron microscope ((JEOL 2100 HRTEM 200V, Japan). EDX analysis was performed on equipment attached to SEM. Diffuse reflectance spectroscopy was done on UV/Visible spectrophotometer (Shimadzu 2450, Japan), Concentration abatement of the dye was monitored on UV/Visible spectrophotometer (Agilent Cary 60, Malaysia) at its wavelength of maximum absorption. Chemical oxygen demand was determined on HACH DR3900 spectrophotometer.

#### 5.3.2 Electrochemical Reactor design and measurements:

A computer-controlled potentiostat (autolab PGSTAT 302N) using three-electrode system was used. The working electrodes used include  $\text{BiVO}_4/\text{Ti}$ ,  $\text{B-BiVO}_4/\text{Ti}$ ,  $\text{CNP-BiVO}_4/\text{Ti}$ ,  $\text{CNP/B-BiVO}_4/\text{Ti}$ ,  $\text{WO}_3/\text{Ti}$  and  $\text{CNP/B-BiVO}_4/\text{WO}_3/\text{Ti}$ , reference electrode was  $\text{Ag}/\text{AgCl}$  (3M KCl) and counter electrode was coiled platinum wire. Linear sweep voltammetric measurements were carried out in 0.1 M solution of  $\text{Na}_2\text{SO}_4$  and amperometric measurements in the presence and in the absence of photons were performed in  $5 \text{ mgL}^{-1}$  solution of orange II sodium salt (prepared in 0.1 M  $\text{Na}_2\text{SO}_4$ ). Electrochemical oxidation of the dye was carried out in a quartz photoelectrochemical cell in the presence and in the absence of light. Typically, 250 mL of the simulated wastewater (containing  $5 \text{ mgL}^{-1}$  of the analyte) was electrolysed in an experiment with continuous stirring of the electrolytic solution. The solar light source was Oriel solar simulator. The simulator has a xenon lamp of 100 W and a UV cut-off filter (Air Mass 1.5 Global filter), giving 1.0 sun output. The distance between the photoelectrochemical cell and the light source was about 5 cm. The schematic of the reactor setup and the actual image of the solar simulator are presented in Fig 5.1a and b respectively.



a)



b)

Figure 5.1. a) A schematic diagram of a single cell reactor for photoelectrochemical degradation. b) Picture of the actual photoelectrochemical reactor

### 5.3.3 Synthesis of WO<sub>3</sub> nanorods

The synthesis of WO<sub>3</sub> nanorods is as follows: 2.62 g of Na<sub>2</sub>WO<sub>4</sub>·2H<sub>2</sub>O was dissolved in 80 mL of deionised water and this was followed by addition of 1.0 g of NaCl. The homogeneous mixture obtained was then acidified with HCl until the pH was 2.06. Upon addition of HCl, the mixture turned white precipitate and this precursor solution was transferred to a 100 mL teflon-lined autoclave. The autoclave was sealed and maintained at 180°C in an oven for 24 h. After cooling to room temperature, the synthesised material was transferred into centrifuge tubes and washed by centrifugation repeatedly with deionised water and then ethanol. The material was then dried at 80°C in air oven for 8 h. The powder material obtained after drying was kept for use.

### 5.3.4 Preparation of carbon nanoparticles, BiVO<sub>4</sub> and CNP/B-BiVO<sub>4</sub>

Carbon nanoparticles (CNPs) were prepared from oats purchased from a local market in Johannesburg, South Africa. A 5 g of oats was powdered by grinding. The powder was then put into a crucible and transferred into a muffle furnace maintained at 400°C for 2 h. The black material formed was allowed to cool to room

temperature, pulverised and subsequently dispersed in deionised water. The dispersion was centrifuged and the supernatant was decanted into a clean beaker. This process was repeated severally to obtain more supernatants. The water in the supernatant was evaporated and the solid particles left in the beaker were collected and kept for use.

To synthesise pristine  $\text{BiVO}_4$ , 0.61 g of  $\text{NaVO}_3$  was dissolved in about 40 mL of deionised water and 2.43 g of  $\text{Bi}(\text{NO}_3)_3 \cdot 5\text{H}_2\text{O}$  were dissolved in 0.1 M  $\text{HNO}_3$ . The  $\text{NaVO}_3$  solution was then gradually added to the  $\text{Bi}(\text{NO}_3)_3$  solution. The yellow precursor solution formed was transferred into a teflon-lined autoclave, sealed and put into the stainless steel shell. This was then maintained  $180^\circ\text{C}$  for 24 h in an oven. Upon cooling, the material was transferred into centrifuge tubes and washed a few times with water. The yellow substance obtained after decantation was dried in an air oven at  $80^\circ\text{C}$  for 8 h. Preparation of CNP/B- $\text{BiVO}_4$  followed the same procedure except that 1.0 g of  $\text{H}_3\text{BO}_3$  and 10 mg of CNP were added to the solution of  $\text{NaVO}_3$  prior to mixing with  $\text{Bi}(\text{NO}_3)_3 \cdot 5\text{H}_2\text{O}$  solution.

### 5.3.5 Fabrication of the photoanode

Ti sheets were firstly degreased in 40% m/m NaOH solution heated to  $80^\circ\text{C}$  and maintained for 2 h. Etching of the sheets was then carried out in a 18% v/v HCl solution maintained at  $98^\circ\text{C}$  for 2 h.

The dispersions of  $\text{BiVO}_4$ , B- $\text{BiVO}_4$ , CNP/ $\text{BiVO}_4$ , CNP/B- $\text{BiVO}_4$  and  $\text{WO}_3$  were prepared by weighing 0.2 g of each of the catalysts into an ethanolic solution of polyethylene glycol (PEG) (containing 2 mL of ethanol and 1 mL of PEG). A mixture of both CNP/B- $\text{BiVO}_4$  and  $\text{WO}_3$  was also prepared by dispersing 0.1 g each of the catalysts in ethanolic solution of PEG. The dispersions were ultrasonicated for 60 min.

A 100  $\mu\text{L}$  of the dispersion was drop cast onto both sides of the prepared Ti sheets with exposed area  $4\text{ cm}^2$ . The coated sheets were dried in an air oven at a temperature of  $250^\circ\text{C}$ . The coating was repeated once more and the sheets were sintered at  $500^\circ\text{C}$  in a muffle furnace.

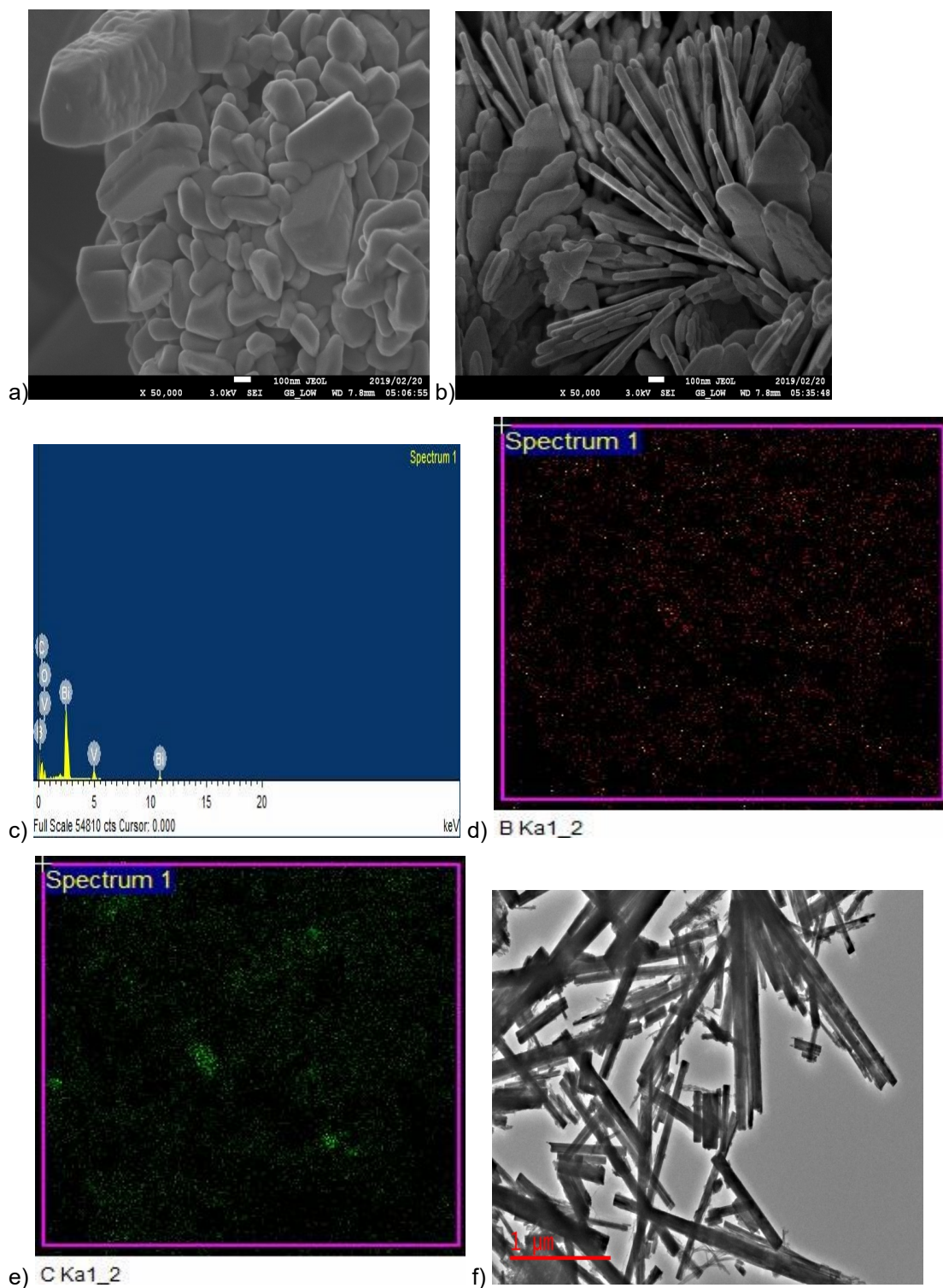
## 5.4 RESULT AND DISCUSSION

### 5.4.1 Morphology investigation, EDS analysis and elemental mapping

Prior to electron microscopy, XRD was used to confirm the successful synthesis of the  $\text{BiVO}_4$  and CNP/B- $\text{BiVO}_4$ , and b)  $\text{WO}_3$ .

The SEM and TEM images, EDS spectra and element maps are presented in fig. 2. From the SEM image of pristine  $\text{BiVO}_4$  (Fig. 2a), it can be observed that the nanoparticles formed, to a large extent, have uniformly distributed sizes. The particles are seen to be closely packed. The SEM image (Fig. 2b) of the doped  $\text{BiVO}_4$  shows a morphology characteristic of a composite material. It has no regular structure or shape, but the constituents can be seen to be well integrated. The EDS spectrum (Fig. 2c) reveals the presence of B, although it has a very low intensity owing to its very low concentration compared with the other component elements. The elemental map (Fig. 2d) further confirms the presence of B in the nanocomposite, with the element uniformly distributed within the material. Similarly, Fig. 2e reveals that carbon particles are present in the nanocomposite material. The TEM image at  $1\text{ }\mu\text{m}$  (Fig. 2f) reveals that the rods are of different lengths, but

the diameter can be seen to be essentially the same. The TEM image of the carbon particles is presented in fig. 2i, the particles appear to be spherical and agglomerated.



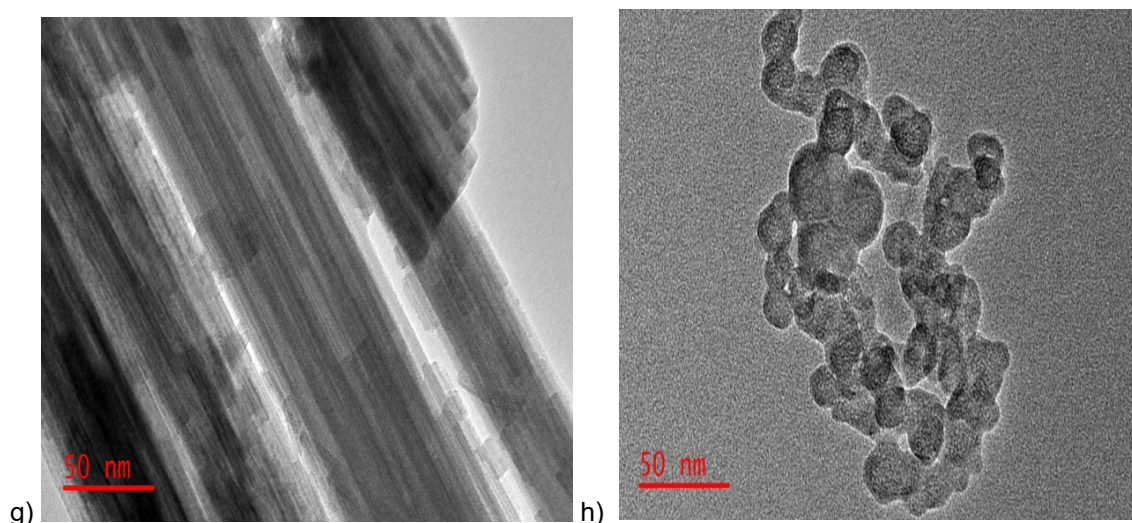


Figure 5.2. SEM images of a)  $\text{BiVO}_4$  and b)  $\text{CNP/B-BiVO}_4$ , c) EDS spectrum of  $\text{CNP/B-BiVO}_4$ , Elemental maps for d) Boron and e) Carbon, TEM images of f)  $\text{WO}_3$  at  $1\ \mu\text{m}$  scale, g)  $\text{WO}_3$  at  $50\ \text{nm}$  scale, h) CNP

#### 5.4.2 Diffuse reflectance spectroscopy

Diffuse reflectance spectroscopy (DRS) is a valuable technique that can be used to gain insights into the electronic states of semiconducting materials. The UV-Vis absorption spectra of  $\text{BiVO}_4$ ,  $\text{WO}_3$  and  $\text{CNP/B-BiVO}_4$  are shown in Fig. 5.3. The intrinsic absorption bands of both the pristine  $\text{BiVO}_4$  and doped  $\text{BiVO}_4$  span over UV and visible light regions. While that of  $\text{WO}_3$  can be seen to be strong within the UV region, extending slightly into the visible region. This absorption characteristic of  $\text{WO}_3$  is in agreement with earlier reports (Cui et al., 2017; Luo, Zhou, Ma & Xu, 2015). The doped  $\text{BiVO}_4$  demonstrates superior visible light absorption compared to pristine  $\text{BiVO}_4$ . In addition, the absorption edge of the CNP and B co-doped  $\text{BiVO}_4$  can be seen to exhibit red-shift. The extension of the absorption edge of the doped material may be as a result of band transitions occurring due to the presence of impurities in the forbidden band (F. Li et al., 2017).

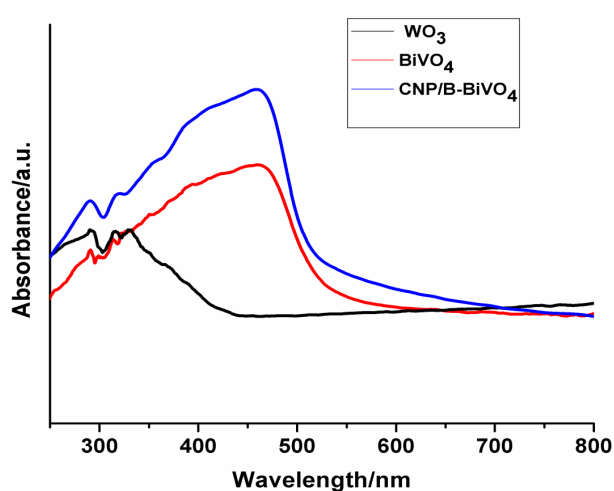


Figure 5.3. UV-Vis absorption spectra of  $\text{BiVO}_4$ ,  $\text{WO}_3$  and  $\text{CNP/B-BiVO}_4$



### 5.4.3 Linear sweep voltammetry and photo-current response

The linear sweep voltammograms of the fabricated photoanodes were obtained in the dark and in the presence of light. As shown in Fig. 5.4a, the current responses of both CNP/B-BiVO<sub>4</sub> and CNP/B-BiVO<sub>4</sub>/WO<sub>3</sub> in the dark are not significantly different until reaching the potential of about 1.0 V, with the bi-component electrode displaying a slightly higher current than the doped BiVO<sub>4</sub> electrode (0.16 and 0.15 mA at 1.3 V). Apparently, the presence of WO<sub>3</sub> contributed to the current signal of the bi-component electrode. It is well known that WO<sub>3</sub> exhibit better charge-transfer property than BiVO<sub>4</sub> (Hong, Lee, Jang & Lee, 2011; Lee et al., 2016). In addition, in both doped BiVO<sub>4</sub> and coupled electrodes, photocurrent can be seen to increase as the anodic potential increases. In the presence of light, the photoanodes showed markedly higher photocurrent than those recorded under dark condition (Fig. 5.4b). The significant photocurrent enhancement recorded by the coupled semiconductors anode can be attributed to synergistic effects of the BiVO<sub>4</sub> and WO<sub>3</sub> (Fig. 5.4b). The excellent charge transport property of the WO<sub>3</sub> and the high visible light activity of the BiVO<sub>4</sub> are beneficial for improved photoactivity. As evident in Fig. 5.4b, the photocurrent responses at both CNP/B-BiVO<sub>4</sub> and CNP/B-BiVO<sub>4</sub>/WO<sub>3</sub> are stable over the time range shown.

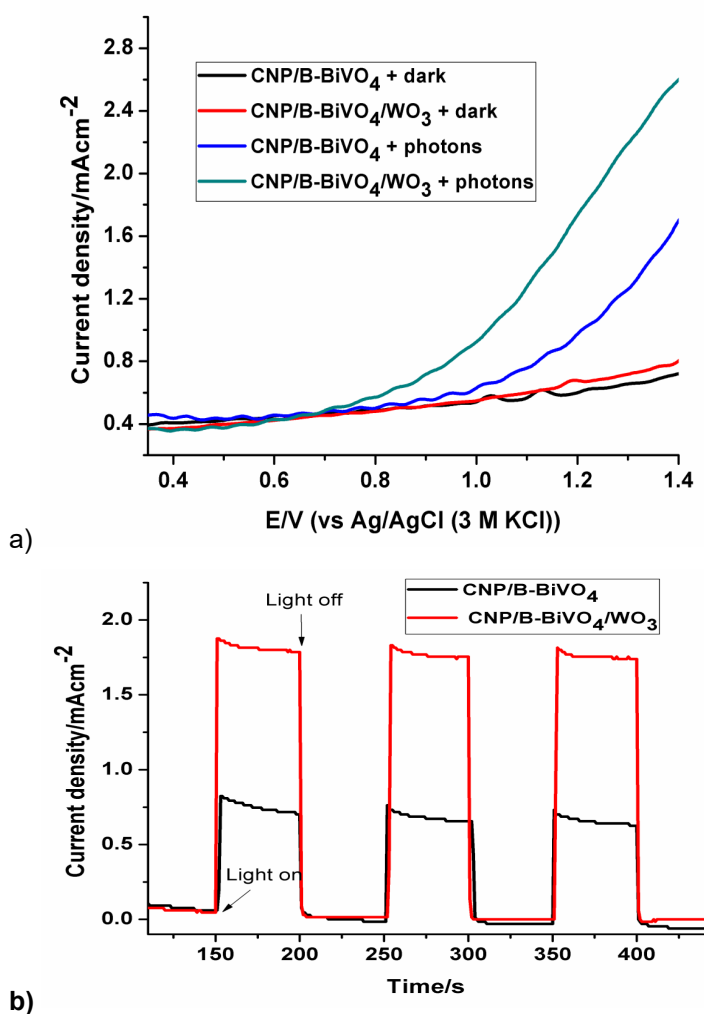


Figure 5.4. a) Linear sweep voltammograms of photoanodes measured in 0.1 M Na<sub>2</sub>SO<sub>4</sub>, b) Photocurrent response of CNP/B-BiVO<sub>4</sub> and CNP/B-BiVO<sub>4</sub>/WO<sub>3</sub> obtained in 5 mgL<sup>-1</sup> orange II dye (prepared in 0.1 M Na<sub>2</sub>SO<sub>4</sub>) at a potential of 1.2 V

#### 5.4.4 Photoelectrocatalytic degradation experiments

Degradation of orange II sodium salt was carried out at the fabricated electrodes to evaluate their photoelectrocatalytic performance.

The oxidation process was performed at applied anodic potential of 2.0 V. The removal efficiency of the dye was calculated from the following relation:

$$\% \text{ removal} = (A_0 - A_t)/A_0 \times 100$$

where  $A_0$  and  $A_t$  are the absorbance values at time  $t = 0$  and  $t = t$  respectively.

As can be seen in Fig. 5.5a, the CNP/B-BiVO<sub>4</sub>/WO<sub>3</sub> electrode exhibited the highest degradation efficiency with 92% removal of the dye in 3 h of the photoelectrocatalytic process. The performance of the photoanodes follows the order BiVO<sub>4</sub> < B-BiVO<sub>4</sub> < WO<sub>3</sub> < CNP-BiVO<sub>4</sub> < CNP/B-BiVO<sub>4</sub> < CNP/B-BiVO<sub>4</sub>/WO<sub>3</sub>. Degradation efficiency at B-doped BiVO<sub>4</sub> photoanode is only slightly higher than that obtained at the pristine BiVO<sub>4</sub> anode (data not shown). Wang et al. made similar observation in the photocatalytic performance of BiVO<sub>4</sub> and B-BiVO<sub>4</sub> (M. Wang, Che, Niu, Dang & Dong, 2013). The authors reported that boron doping narrows the band gap energy of the photocatalyst by a magnitude of 0.04 eV, thus increasing its light absorption in the visible region. It was also suggested that interstitial boron doping can increase the number of oxygen vacancies and V<sup>4+</sup>, leading to red-shifting of the absorption edge and consequently improved photocatalytic performance in the visible light region. It is noteworthy that the performance of pristine BiVO<sub>4</sub> is inferior to that of the pure WO<sub>3</sub> nanorods despite the former being a better absorber of visible light. The poor conductivity and low adsorption capability of BiVO<sub>4</sub> are some of the factors responsible for its low photoelectrocatalytic performance. On the other hand, the large surface area of WO<sub>3</sub> (BET surface area not shown) and its excellent conductivity are favourable for the degradation of organic pollutants. However, incorporation of CNP into BiVO<sub>4</sub> leads to significant improvement in its photoelectrocatalytic performance. In essence, the CNP and B co-doped BiVO<sub>4</sub> showed much more enhanced performance. Also, incorporation of CNP into the structure of BiVO<sub>4</sub> could lead to improved charge transport property and enhanced adsorption capability of the photocatalyst. Apparently, the CNP/B-BiVO<sub>4</sub>/WO<sub>3</sub> performed best because of the contributions of the various constituent materials. The kinetic rate constants obtained by fitting the degradation experimental data into the Langmuir Hinshelwood kinetic model are 0.0924, 0.1812, 0.254 and 0.845 h<sup>-1</sup> for BiVO<sub>4</sub>, WO<sub>3</sub>, CNP/B-BiVO<sub>4</sub> and CNP/B-BiVO<sub>4</sub>/WO<sub>3</sub> respectively. Figure 5.5b displays the plots of normalised concentration abatement of the dye via photolysis, electrolysis and photoelectrocatalysis. It can be seen that the coupled process offers a far more efficient removal of the dye than the individual processes. This observation further affirms the superiority of photoelectrocatalytic oxidation process to both electrochemical oxidation and photocatalytic oxidation processes. The COD decay after 3 h of the photoelectrocatalytic process at the preferred anode was 58%.



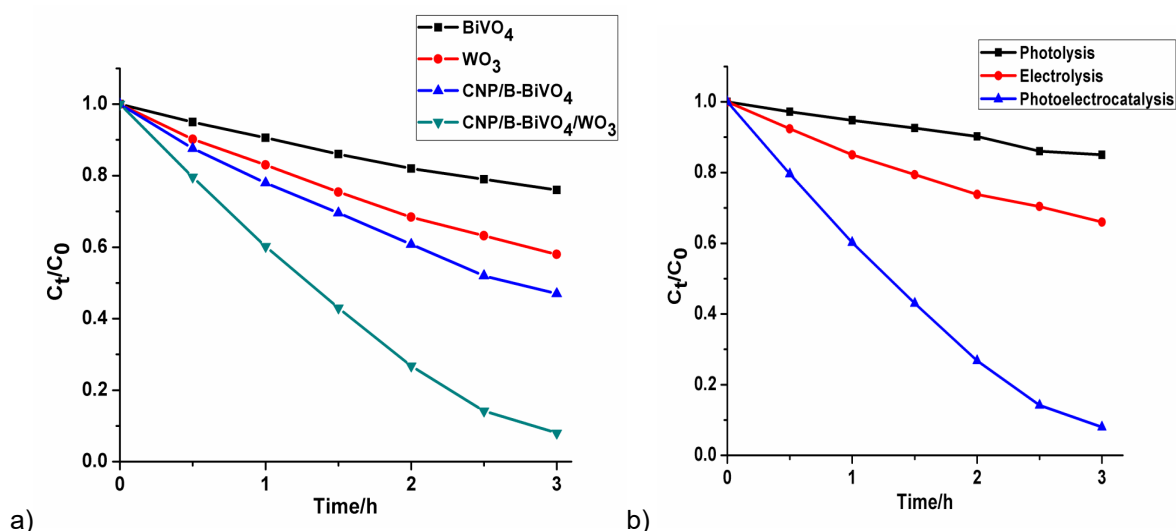


Figure 5.5. a) Degradation profiles of orange II sodium salt a) at different photoanodes, b) by different oxidation processes.

**Sub conclusion.** Two visible-light sensitive semiconductors, namely,  $\text{BiVO}_4$  and  $\text{WO}_3$  have been synthesised, characterised and applied for the degradation of a model organic pollutant, orange II dye. The results obtained shows that the combination of two semiconductors through band gap alignment can improve degradation efficiency. The higher performance of this electrode can be linked to the formation of n-n heterojunction which promotes separation of charges and generation of large amount of the valence-bound holes which are needed for the oxidation of the pollutant. The doping effect of boron also added to the performance of this novel photoanode.

We have also used a more rigid platform – a titanium sheet – for the preparation of the  $\text{BiVO}_4$  and  $\text{WO}_3$  photoanode. We believe this will fit better into the reactor compartment for a flow-through reactor. The robustness of the titanium sheet photoanode resumted in the use of a higher current density than our previously reported exfoliated graphite substrate.

## CHAPTER 6: FLOW-THROUGH REACTOR DESIGN

---

### 6.1 INTRODUCTION

In order to move towards real application or upscale, there is need to design a flow-through reactor that will be able to treat litres of wastewater on a continuous basis. A milestone towards this long-term realisation is the design of a prototype reactor the treatment of some volumes of wastewater continuously. In this project, we have collaborated with a company called Radical Waters.

#### 6.1.1 About Radical Waters

Radical Waters (Pty) Ltd has spent over 20 years focused on developing and commercialising its patented green Electrochemically Activated Water (ECA) technology. The company has installed operating ECA devices on 6 continents and in 27 countries primarily for blue chip companies. Their products are used in a wide range of markets formerly dependent on chemicals for controlling contamination and bacterial infection. Radical waters manufacture Natural Hygiene Generators for solutions generically known as Anolyte and Catholyte. These activated waters destabilizes and elevates the electrical charge of the water and creates an environment in which microbes cannot survive.

#### 6.1.2 The flow-through reactor design

In collaboration with the engineers at Radical Waters, we have designed (on paper) a prototype reactor which we hope to begin its fabrication soon. A part of the schematic is shown in Fig 6.1.

Some of the essential parts of the reactor design include:

1. Off Water pump 24V.dc (0-3.8l/min)
2. 10 micron bag filter
3. 5 micron bag filter
4. Visual flow meter for high flow
5. Hydraulic control valves (pinch valves)
6. Transparent 2 cell plate reactor block
7. 4 off level switches
8. Control box
9. 1-16V dc 40A variable PSU for activation
10. 10A 24V.dc PSU for Water pumps
11. Activation switch and indicator lamp
12. 2 off Pump control switch and indicator lamps
13. Power indicator lamp
14. Micro controller, Main board and LCD
15. Analog 0-5A current meter

## Low flow system description:

Figure 1 Process and instrumentation flow diagram for low f

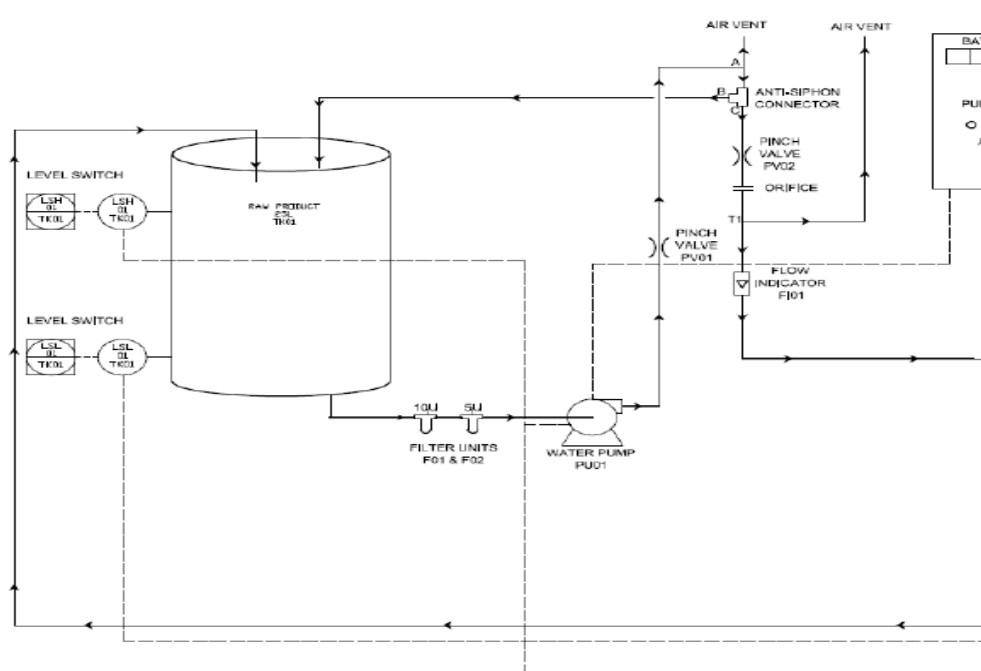


Figure 6.1. Part of the process design for the flow-through photoelectrochemical reactor

The reactor needs to be built and optimised. We envisage the use of titanium plate based anode for this reactor.

## CHAPTER 7: CONCLUSIONS & RECOMMENDATIONS

### 7.1 CONCLUSIONS

#### 7.1.1 Photoelectrochemical catalytic degradation

This research has demonstrated the possibilities of the treatment of water polluted with dyes and pharmaceuticals with PEC. A myriad of carbon and semiconductor materials such as exfoliated graphite, reduced graphene oxide, carbon nanoparticle,  $\text{TiO}_2$ ,  $\text{ZnO}$ ,  $\text{WO}_3$ , and  $\text{BiVO}_4$ , etc. have been successfully synthesised and characterised. Novel semiconductor photoanodes based on carbon substrates were fabricated and used in the removal of organic pollutants such as dyes and pharmaceuticals from water.

The photoanodes prepared and the pollutants degraded have been presented in Table 3-2, which is shown again as Table 7-1.

Table 7-1. Summary of photoanodes and pollutants degraded in this project

| S/N | Photoanode                                 | Organic pollutants degraded  | Reference                        |
|-----|--|------------------------------|----------------------------------|
| 1   | Ag-ZnO-rGO                                 | Orange II dye                | (Umukoro et al., 2016a, 2016b)   |
| 2   | EG- $\text{WO}_3$                          | Orange II dye, 2-nitrophenol | (Umukoro, Peleyeju et al., 2017) |
| 3   | EG- $\text{TiO}_2$                         | sulfamethoxazole             | (M. G. Peleyeju et al., 2017)    |
| 4   | Pd-ZnO-EG                                  | 4-nitrophenol                | (Umukoro, Madyibi et al., 2017)  |
| 5   | $\text{MoS}_2$ - $\text{SnO}_2$ /EG        | ciprofloxacin                | (Umukoro, Kumar et al., 2018)    |
| 6   | EG- $\text{BiVO}_4$ / $\text{ZnO}$         | Rhodamine B dye              | (Orimolade et al., 2019)         |
| 7   | CNP/B- $\text{BiVO}_4$ / $\text{WO}_3$ /Ti | Orange II dye                | Manuscript in preparation        |

The initial sets of photoanodes prepared (Table 7-1, no. 1-4) were based on single semiconductor or doped semiconductors. These types of photoanodes yielded good degradation efficiencies. The effect of semiconductor doping on degradation efficiency has been studied and demonstrated. This project has shown that exfoliated graphite can be used as a photoanode component to reduce the rate of recombination of electron-hole in a semiconductor and thus improve degradation efficiency.

In the quest to improve the performance of the photoanodes, we started investigation on the possibilities of mixed semiconductors or formation of heterojunctions. Though this is still under current investigations, but we can see that the photocurrent responses can be improved using the concept of heterojunctions. The response of the photoanode to solar light is a measure of its sustainability as we drive our research towards harnessing the huge untapped energy from the sun. While it is difficult to make absolute conclusions on the performances of these photoanodes when compared, their responses to solar light can give an indication of light harvesting improvement. As presented in Fig 7.1, the highest photocurrent response was observed for the heterojunction photoanodes.

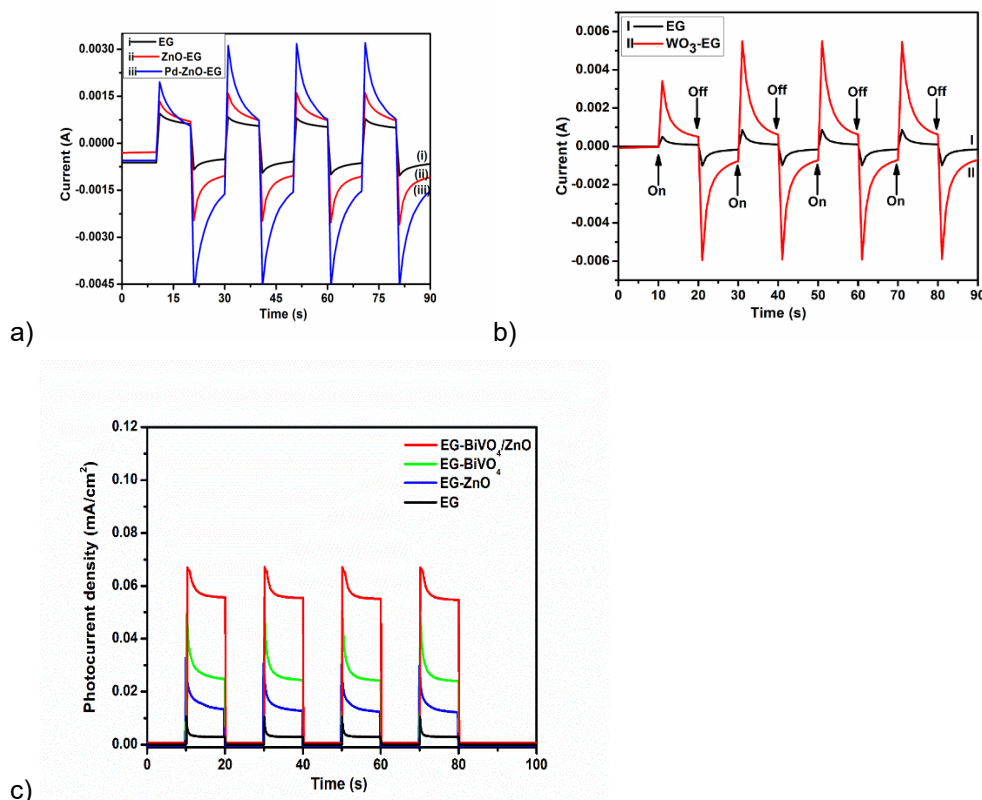


Figure 7.1. Photocurrent responses of photoanodes in the dark and in the presence of solar light (a) Pd-ZnO-EG (b) WO<sub>3</sub>-EG and (c) EG-BiVO<sub>4</sub>/ZnO

The exfoliated graphite support, though yielded excellent degradation efficiencies, was found to not be strong mechanically. The flow-through reactor may need a more rigid electrode plate that may need to be screwed to the reactor chamber. EG based photoanodes may pose a challenge in this regard. Thus, we have prepared new photoanodes on titanium sheet (Table 7-1, no. 7).

This work has given us the platform to understand the concept of photoelectrochemical catalysis and the behaviours of the materials we have prepared. The knowledge gleaned can now be transferred to a more complex system – the flowthrough reactor.

### 7.1.2 Electrocoagulation

This work has demonstrated the advantage of electrocoagulation over chemical coagulation using a dye and heavy metal as case study.

We have shown that the material used for anodes in EC can be a determinant of the efficiency of coagulation. Particularly, we have shown that stainless steels do not perform alike. In our work, we compared the performances of two different types of stainless steel. Results showed that each type of steel behaves differently in the presence of organic pollutant and heavy metal. This is a very important result which suggests that there is need to optimise EC performance with a particular electrode type.

## **7.2 RECOMMENDATIONS**

### **7.2.1 Photoelectrochemical catalytic degradation**

In order to take the research forward, we propose the following recommendations

Further study on semiconductor combination as heterojunctions in photoanode fabrication.

We encountered many challenges with the preparation of Ti based photoanodes especially in the stability of the semiconductor film. The current method used in our lab is anodisation, thus there is need to explore more sophisticated film deposition techniques to deter the leaching of the semiconductor from the titanium surface. There need to explore other photoanode supports such as conducting glass, etc.

The fabrication or design and testing of the flow through prototype reactor should be encouraged to commence. There is need to now commence investigation on the treatment of more complex samples and real sample.

### **7.2.2 Electrocoagulation**

The application of other non-conventional anodic materials for EC should be investigated.

Since the performance of an anodic material may vary with organic or metal removal, the use of alloys may present a plausible optimisation approach.

There is need to increase the volume of water treated with EC and now commence investigation on the treatment of more complex samples and real sample.

### **7.2.3 Combination of Photoelectrochemical catalytic degradation (PEC) with Electrocoagulation (EC)**

The knowledge gleaned in the study of PEC and EC for wastewater treatment can now be used in the development of a combined reactor, which we could not realise in this project owing to limited time and finance. A combined reactor will involve variables such cell configuration, light penetration, flow rate, retention time, order of arrangement of EC and PEC, etc. These variables need to be considered carefully and optimised for good reactor performance.

## REFERENCES

- Abramian, L. & El-Rassy, H. (2009). Adsorption kinetics and thermodynamics of azo-dye Orange II onto highly porous titania aerogel. *Chemical Engineering Journal*, 150(2-3), 403-410.
- Ahmed, B., Kumar, S., Ojha, A. K., Donfack, P. & Materny, A. (2017). Facile and controlled synthesis of aligned WO<sub>3</sub> nanorods and nanosheets as an efficient photocatalyst material. *Spectrochimica Acta Part A: Molecular and Biomolecular Spectroscopy*, 175, 250-261.
- Ahmed, T., Zhang, H.-l., Xu, H.-b. & Zhang, Y. (2017). m-BiVO<sub>4</sub> hollow spheres coated on carbon fiber with superior reusability as photocatalyst. *Colloids and Surfaces A: Physicochemical and Engineering Aspects*, 531, 213-220.
- Akbarzadeh, R., Fung, C. S., Rather, R. A. & Lo, I. M. (2018). One-pot hydrothermal synthesis of g-C<sub>3</sub>N<sub>4</sub>/Ag/AgCl/BiVO<sub>4</sub> micro-flower composite for the visible light degradation of ibuprofen. *Chemical Engineering Journal*, 341, 248-261.
- Ama, O., Mabuba, N. & Arotiba, O. (2015). Synthesis, Characterization, and Application of Exfoliated Graphite/Zirconium Nanocomposite Electrode for the Photoelectrochemical Degradation of Organic Dye in Water. *Electrocatalysis*, 6(4), 390-397.
- An, C., Huang, G., Yao, Y. & Zhao, S. (2017). Emerging usage of electrocoagulation technology for oil removal from wastewater: A review. *Science of The Total Environment*, 579, 537-556.
- Aoudj, S., Khelifa, A., Drouiche, N., Belkada, R. & Miroud, D. (2015). Simultaneous removal of chromium (VI) and fluoride by electrocoagulation-electroflotation: application of a hybrid Fe-Al anode. *Chemical Engineering Journal*, 267, 153-162.
- Association, A. P. H. & Association, A. W. W. (1989). *Standard methods for the examination of water and wastewater*: American public health association.
- Aziz, A. R. A., Asaithambi, P. & Daud, W. M. A. B. W. (2016). Combination of electrocoagulation with advanced oxidation processes for the treatment of distillery industrial effluent. *Process Safety and Environmental Protection*, 99, 227-235.
- Baddouh, A., Bessegato, G. G., Rguiti, M. M., El Ibrahim, B., Bazzi, L., Hilali, M. & Zanon, M. V. B. (2018). Electrochemical decolorization of Rhodamine B dye: Influence of anode material, chloride concentration and current density. *Journal of Environmental Chemical Engineering*, 6(2), 2041-2047.
- Bessegato, G. G., Cardoso, J. C. & Zanon, M. V. B. (2015). Enhanced photoelectrocatalytic degradation of an acid dye with boron-doped TiO<sub>2</sub> nanotube anodes. *Catalysis Today*, 240, 100-106.
- Bhagawan, D., Poodari, S., Golla, S., Himabindu, V. & Vidyavathi, S. (2016). Treatment of the petroleum refinery wastewater using combined electrochemical methods. *Desalination and Water Treatment*, 57(8), 3387-3394.
- Bocos, E., Brillas, E., Sanroman, M. A. & Sirés, I. (2016). Electrocoagulation: simply a phase separation technology? The case of bronopol compared to its treatment by EAOPs. *Environmental science & technology*, 50(14), 7679-7686.
- Brillas, E. & Martínez-Huitle, C. A. (2015). Decontamination of wastewaters containing synthetic organic dyes by electrochemical methods. An updated review. *Applied Catalysis B: Environmental*, 166-167, 603-643. doi: 10.1016/j.apcatb.2014.11.016
- Butterfield, I. M., Christensen, P. A., Hamnett, A., Shaw, K. E., Walker, G. M., Walker, S. A. & Howarth, C. R. (1997). Applied studies on immobilized titanium dioxide films as catalysts for the photoelectrochemical detoxification of water. *Journal of Applied Electrochemistry*, 27(4), 385-395.
- Cardoso, J. C., Bessegato, G. G. & Zanon, M. V. B. (2016). Efficiency comparison of ozonation, photolysis, photocatalysis and photoelectrocatalysis methods in real textile wastewater decolorization. *Water research*, 98, 39-46.
- Chafi, M., Gourich, B., Essadki, A., Vial, C. & Fabregat, A. (2011). Comparison of electrocoagulation using iron and aluminium electrodes with chemical coagulation for the removal of a highly soluble acid dye. *Desalination*, 281, 285-292.
- Chamjangali, M. A. & Boroumand, S. (2013). Synthesis of flower-like Ag-ZnO nanostructure and its application in the photodegradation of methyl orange. *Journal of the Brazilian Chemical Society*, 24(8), 1329-1338.
- Chellam, S. & Sari, M. A. (2016). Aluminum electrocoagulation as pretreatment during microfiltration of surface water containing NOM: A review of fouling, NOM, DBP, and virus control. *Journal of Hazardous Materials*, 304, 490-501.
- Chen, F., Liu, Z., Liu, Y., Fang, P. & Dai, Y. (2013). Enhanced adsorption and photocatalytic degradation of high-concentration methylene blue on Ag<sub>2</sub>O-modified TiO<sub>2</sub>-based nanosheet. *Chemical Engineering Journal*, 221, 283-291.

- Chen, F., Yan, F., Chen, Q., Wang, Y., Han, L., Chen, Z. & Fang, S. (2014). Fabrication of Fe<sub>3</sub>O<sub>4</sub>@SiO<sub>2</sub>/TiO<sub>2</sub> nanoparticles supported by graphene oxide sheets for the repeated adsorption and photocatalytic degradation of rhodamine B under UV irradiation. *Dalton Transactions*, 43(36), 13537-13544.
- Chen, H., Gao, B., Li, H. & Ma, L. Q. (2011). Effects of pH and ionic strength on sulfamethoxazole and ciprofloxacin transport in saturated porous media. *Journal of contaminant hydrology*, 126(1-2), 29-36.
- Cui, L., Ding, X., Wang, Y., Shi, H., Huang, L., Zuo, Y. & Kang, S. (2017). Facile preparation of Z-scheme WO<sub>3</sub>/gC<sub>3</sub>N<sub>4</sub> composite photocatalyst with enhanced photocatalytic performance under visible light. *Applied Surface Science*, 391, 202-210.
- Das, A. K., Srivastav, M., Layek, R. K., Uddin, M. E., Jung, D., Kim, N. H. & Lee, J. H. (2014). Iodide-mediated room temperature reduction of graphene oxide: a rapid chemical route for the synthesis of a bifunctional electrocatalyst. *Journal of Materials Chemistry A*, 2(5), 1332-1340.
- Davey, J. & Schäfer, A. (2009). Ultrafiltration to supply drinking water in international development: a review of opportunities *Appropriate technologies for environmental protection in the developing world* (pp. 151-168): Springer.
- de Amorim, K. P., Romualdo, L. L. & Andrade, L. S. (2013). Electrochemical degradation of sulfamethoxazole and trimethoprim at boron-doped diamond electrode: performance, kinetics and reaction pathway. *Separation and Purification Technology*, 120, 319-327.
- de Deus Rodrigues, C. S. (2013). Textile Dyeing Wastewater Treatment by Single and Integrated Processes of Coagulation, Chemical Oxidation and Biological Degradation.
- Demirbas, E. & Kobya, M. (2017). Operating cost and treatment of metalworking fluid wastewater by chemical coagulation and electrocoagulation processes. *Process Safety and Environmental Protection*, 105, 79-90.
- Di Paola, A., García-López, E., Marci, G. & Palmisano, L. (2012). A survey of photocatalytic materials for environmental remediation. *Journal of Hazardous Materials*, 211, 3-29.
- Dirany, N., Arab, M., Leroux, C., Villain, S., Madigou, V. & Gavarri, J. (2016). Effect of WO<sub>3</sub> nanoparticles morphology on the catalytic properties. *Materials Today: Proceedings*, 3(2), 230-234.
- Donaghue, A. & Chaplin, B. P. (2013). Effect of select organic compounds on perchlorate formation at boron-doped diamond film anodes. *Environmental science & technology*, 47(21), 12391-12399.
- Dong, P., Hou, G., Xi, X., Shao, R. & Dong, F. (2017). WO<sub>3</sub>-based photocatalysts: morphology control, activity enhancement and multifunctional applications. *Environmental Science: Nano*, 4(3), 539-557.
- DWA. (2013). The Green Drop Handbook. Retrieved June, 2019, from [http://www.dwa.gov.za/Dir\\_WS/DWQR/subscr/ViewComDoc.asp?Docid=417](http://www.dwa.gov.za/Dir_WS/DWQR/subscr/ViewComDoc.asp?Docid=417)
- El-Ashtoukhy, E. Z., Amin, N., El-Latif, M. A., Bassyouni, D. & Hamad, H. (2017). New insights into the anodic oxidation and electrocoagulation using a self-gas stirred reactor: A comparative study for synthetic Cl Reactive Violet 2 wastewater. *Journal of cleaner production*, 167, 432-446.
- Emamjomeh, M. M. & Sivakumar, M. (2009). Review of pollutants removed by electrocoagulation and electrocoagulation/flotation processes. *Journal of environmental management*, 90(5), 1663-1679.
- Esfandyari, Y., Mahdavi, Y., Seyedsalehi, M., Hoseini, M., Safari, G. H., Ghosikali, M. G., . . . Jaafari, J. (2015). Degradation and biodegradability improvement of the olive mill wastewater by peroxi-electrocoagulation/electrooxidation-electroflotation process with bipolar aluminum electrodes. *Environmental Science and Pollution Research*, 22(8), 6288-6297.
- Fajardo, A. S., Rodrigues, R. F., Martins, R. C., Castro, L. M. & Quinta-Ferreira, R. M. (2015). Phenolic wastewaters treatment by electrocoagulation process using Zn anode. *Chemical Engineering Journal*, 275, 331-341.
- Fan, M., Yang, C., Pu, W. & Zhang, J. (2014). Liquid phase deposition of ZnO film for photoelectrocatalytic degradation of p-nitrophenol. *Materials Science in Semiconductor Processing*, 17, 104-109.
- Feng, J., Cheng, L., Zhang, J., Okoth, O. K. & Chen, F. (2018). Preparation of BiVO<sub>4</sub>/ZnO composite film with enhanced visible-light photoelectrocatalytic activity. *Ceramics International*, 44(4), 3672-3677.
- García-García, A., Martínez-Miranda, V., Martínez-Cienfuegos, I. G., Almazán-Sánchez, P. T., Castañeda-Juárez, M. & Linares-Hernández, I. (2015). Industrial wastewater treatment by electrocoagulation-electrooxidation processes powered by solar cells. *Fuel*, 149, 46-54.
- Garcia-Segura, S., Eiband, M. M. S., de Melo, J. V. & Martínez-Huitle, C. A. (2017). Electrocoagulation and advanced electrocoagulation processes: A general review about the fundamentals, emerging applications and its association with other technologies. *Journal of Electroanalytical Chemistry*, 801, 267-299.
- Garza-Campos, B. R., Guzmán-Mar, J. L., Reyes, L. H., Brillas, E., Hernández-Ramírez, A. & Ruiz-Ruiz, E. J. (2014). Coupling of solar photoelectro-Fenton with a BDD anode and solar heterogeneous photocatalysis for the mineralization of the herbicide atrazine. *Chemosphere*, 97, 26-33. doi: 10.1016/j.chemosphere.2013.10.044
- Geng, Y., Zhang, P., Li, N. & Sun, Z. (2015). Synthesis of Co doped BiVO<sub>4</sub> with enhanced visible-light photocatalytic activities. *Journal of Alloys and Compounds*, 651, 744-748.



- Ghosh, D., Medhi, C. & Purkait, M. (2008). Treatment of fluoride containing drinking water by electrocoagulation using monopolar and bipolar electrode connections. *Chemosphere*, 73(9), 1393-1400.
- Giri, A. S. & Golder, A. K. (2014). Ciprofloxacin degradation from aqueous solution by Fenton oxidation: reaction kinetics and degradation mechanisms. *RSC Advances*, 4(13), 6738-6745.
- Grbić, B., Radić, N., Stojadinović, S., Vasilić, R., Dohčević-Mitrović, Z., Šaponjić, Z. & Stefanov, P. (2014). TiO<sub>2</sub>/WO<sub>3</sub> photocatalytic composite coatings prepared by spray pyrolysis. *Surface and Coatings Technology*, 258, 763-771.
- Hai, F. I., Yamamoto, K. & Fukushi, K. (2007). Hybrid treatment systems for dye wastewater. *Critical Reviews in Environmental Science and Technology*, 37(4), 315-377. doi: 10.1080/10643380601174723
- Hakizimana, J. N., Gourich, B., Chafi, M., Stiriba, Y., Vial, C., Drogui, P. & Naja, J. (2017). Electrocoagulation process in water treatment: A review of electrocoagulation modeling approaches. *Desalination*, 404, 1-21.
- Halimoon, N. & Yin, R. G. S. (2010). Removal of heavy metals from textile wastewater using zeolite. *Environment Asia*, 3(2010), 124-130.
- Harif, T., Khai, M. & Adin, A. (2012). Electrocoagulation versus chemical coagulation: coagulation/flocculation mechanisms and resulting floc characteristics. *Water research*, 46(10), 3177-3188.
- He, Z., Shi, Y., Gao, C., Wen, L., Chen, J. & Song, S. (2013). BiOCl/BiVO<sub>4</sub> p-n heterojunction with enhanced photocatalytic activity under visible-light irradiation. *The Journal of Physical Chemistry C*, 118(1), 389-398.
- Hilliard, S., Baldinozzi, G., Friedrich, D., Kressman, S., Strub, H., Artero, V. & Laberty-Robert, C. (2017). Mesoporous thin film WO<sub>3</sub> photoanode for photoelectrochemical water splitting: a sol-gel dip coating approach. *Sustainable Energy & Fuels*, 1(1), 145-153.
- Ho-Kimura, S., Moniz, S. J., Handoko, A. D. & Tang, J. (2014). Enhanced photoelectrochemical water splitting by nanostructured BiVO<sub>4</sub>-TiO<sub>2</sub> composite electrodes. *Journal of Materials Chemistry A*, 2(11), 3948-3953.
- Hong, S. J., Lee, S., Jang, J. S. & Lee, J. S. (2011). Heterojunction BiVO<sub>4</sub>/WO<sub>3</sub> electrodes for enhanced photoactivity of water oxidation. *Energy & Environmental Science*, 4(5), 1781-1787.
- Hu, L., Flanders, P. M., Miller, P. L. & Strathmann, T. J. (2007). Oxidation of sulfamethoxazole and related antimicrobial agents by TiO<sub>2</sub> photocatalysis. *Water research*, 41(12), 2612-2626.
- Hua, H., Xi, Y., Zhao, Z., Xie, X., Hu, C. & Liu, H. (2013). Gram-scale wet chemical synthesis of Ag<sub>2</sub>O/TiO<sub>2</sub> aggregated sphere heterostructure with high photocatalytic activity. *Materials Letters*, 91, 81-83.
- Huang, Z. F., Song, J., Pan, L., Zhang, X., Wang, L. & Zou, J. J. (2015). Tungsten oxides for photocatalysis, electrochemistry, and phototherapy. *Advanced Materials*, 27(36), 5309-5327.
- Hunge, Y., Mahadik, M., Mohite, V., Kumbhar, S., Deshpande, N., Rajpure, K., . . . Bhosale, C. (2016). Photoelectrocatalytic degradation of methyl blue using sprayed WO<sub>3</sub> thin films. *Journal of Materials Science: Materials in Electronics*, 27(2), 1629-1635.
- Hussain, S., Gul, S., Steter, J. R., Miwa, D. W. & Motheo, A. J. (2015). Route of electrochemical oxidation of the antibiotic sulfamethoxazole on a mixed oxide anode. *Environmental Science and Pollution Research*, 22(19), 15004-15015.
- Hussin, F., Abnisa, F., Issabayeva, G. & Aroua, M. K. (2017). Removal of lead by solar-photovoltaic electrocoagulation using novel perforated zinc electrode. *Journal of cleaner production*, 147, 206-216.
- Ioannidou, E., Frontistis, Z., Antonopoulou, M., Venieri, D., Konstantinou, I., Kondarides, D. I. & Mantzavinos, D. (2017). Solar photocatalytic degradation of sulfamethoxazole over tungsten-Modified TiO<sub>2</sub>. *Chemical Engineering Journal*, 318, 143-152.
- Jaafarzadeh, N., Omidinasab, M. & Ghanbary, F. (2016). Combined electrocoagulation and UV-based sulfate radical oxidation processes for treatment of pulp and paper wastewater. *Process Safety and Environmental Protection*, 102, 462-472.
- Ji, Y., Ferronato, C., Salvador, A., Yang, X. & Chovelon, J.-M. (2014). Degradation of ciprofloxacin and sulfamethoxazole by ferrous-activated persulfate: implications for remediation of groundwater contaminated by antibiotics. *Science of The Total Environment*, 472, 800-808.
- Kansal, S., Singh, M. & Sud, D. (2007). Studies on photodegradation of two commercial dyes in aqueous phase using different photocatalysts. *Journal of Hazardous Materials*, 141(3), 581-590.
- Ke, J., Liu, J., Sun, H., Zhang, H., Duan, X., Liang, P., . . . Wang, S. (2017). Facile assembly of Bi<sub>2</sub>O<sub>3</sub>/Bi<sub>2</sub>S<sub>3</sub>/MoS<sub>2</sub>n-p heterojunction with layered n-Bi<sub>2</sub>O<sub>3</sub> and p-MoS<sub>2</sub> for enhanced photocatalytic water oxidation and pollutant degradation. *Applied Catalysis B: Environmental*, 200, 47-55.
- Khan, M. E., Khan, M. M. & Cho, M. H. (2016). Fabrication of WO<sub>3</sub> nanorods on graphene nanosheets for improved visible light-induced photocapacitive and photocatalytic performance. *RSC Advances*, 6(25), 20824-20833.
- Khandegar, V. & Saroha, A. K. (2013). Electrocoagulation for the treatment of textile industry effluent – a review. *Journal of environmental management*, 128, 949-963.

- Kim, E. S., Kang, H. J., Magesh, G., Kim, J. Y., Jang, J.-W. & Lee, J. S. (2014). Improved photoelectrochemical activity of  $\text{CaFe}_2\text{O}_4/\text{BiVO}_4$  heterojunction photoanode by reduced surface recombination in solar water oxidation. *ACS applied materials & interfaces*, 6(20), 17762-17769.
- Kobya, M., Ozyonar, F., Demirbas, E., Sik, E. & Oncel, M. (2015). Arsenic removal from groundwater of Sivas-Şarkışla Plain, Turkey by electrocoagulation process: comparing with iron plate and ball electrodes. *Journal of Environmental Chemical Engineering*, 3(2), 1096-1106.
- Kruthika, N. L., Karthika, S., Raju, G. B. & Prabhakar, S. (2013). Efficacy of electrocoagulation and electrooxidation for the purification of wastewater generated from gelatin production plant. *Journal of Environmental Chemical Engineering*, 1(3), 183-188.
- Kumar, M. P., Nidhi, M. & Srivastava, C. (2015). Electrochemical exfoliation of graphite to produce graphene using tetrasodium pyrophosphate. *RSC Advances*, 5(32), 24846-24852.
- Kusmieriek, E. & Chrzescijanska, E. (2015). Application of  $\text{TiO}_2\text{-RuO}_2/\text{Ti}$  electrodes modified with  $\text{WO}_3$  in electro- and photoelectrochemical oxidation of Acid Orange 7 dye. *Journal of Photochemistry and Photobiology A: Chemistry*, 302, 59-68.
- Lawrence, K., Baker, C. L., James, T. D., Bull, S. D., Lawrence, R., Mitchels, J. M., . . . Marken, F. (2014). Functionalized carbon nanoparticles, blacks and soots as electron-transfer building blocks and conduits. *Chemistry – An Asian Journal*, 9(5), 1226-1241. doi: 10.1002/asia.201301657
- Lawrence, K., Xia, F., Arrowsmith, R. L., Ge, H., Nelson, G. W., Foord, J. S., . . . Marken, F. (2014). Hydrothermal Conversion of One-Photon-Fluorescent Poly(4-vinylpyridine) into Two-Photon-Fluorescent Carbon Nanodots. *Langmuir*, 30(39), 11746-11752. doi: 10.1021/la404866s
- Lee, M. G., Kim, D. H., Sohn, W., Moon, C. W., Park, H., Lee, S. & Jang, H. W. (2016). Conformally coated  $\text{BiVO}_4$  nanodots on porosity-controlled  $\text{WO}_3$  nanorods as highly efficient type II heterojunction photoanodes for water oxidation. *Nano Energy*, 28, 250-260.
- Li, F., Zhang, L., Chen, X., Liu, Y., Xu, S. & Cao, S. (2017). Synergistically enhanced photocatalytic reduction of  $\text{CO}_2$  on N-Fe codoped  $\text{BiVO}_4$  under visible light irradiation. *Physical Chemistry Chemical Physics*, 19(32), 21862-21868.
- Li, J.-h., Liu, Q. & Da, H.-f. (2007). Preparation of sulfur-free exfoliated graphite at a low exfoliation temperature. *Materials Letters*, 61(8-9), 1832-1834.
- Li, J., Lv, S., Liu, Y., Bai, J., Zhou, B. & Hu, X. (2013). Photoelectrocatalytic activity of an n- $\text{ZnO}/\text{p-Cu}_2\text{O}/\text{n-TNA}$  ternary heterojunction electrode for tetracycline degradation. *Journal of Hazardous Materials*, 262, 482-488.
- Li, Q., Yu, N., Qiu, Z., Zhou, X. & Wu, C. F. (2008). Preparation of modified carbon black with nano-scale size and enhanced stability in organic solvent by solid state method. *Colloids and Surfaces A: Physicochemical and Engineering Aspects*, 317(1-3), 87-92.
- Li, Y., Zhang, L., Xiang, X., Yan, D. & Li, F. (2014). Engineering of ZnCo-layered double hydroxide nanowalls toward high-efficiency electrochemical water oxidation. *Journal of Materials Chemistry A*, 2(33), 13250-13258.
- Linares Hernández, I., Barrera Díaz, C., Valdés Cerecero, M., Almazán Sánchez, P. T., Castañeda Juárez, M. & Lugo Lugo, V. (2017). Soft drink wastewater treatment by electrocoagulation-electrooxidation processes. *Environmental technology*, 38(4), 433-442.
- Liu, C.-F., Huang, C., Hu, C.-C., Juang, Y. & Huang, C. (2016). Photoelectrochemical degradation of dye wastewater on  $\text{TiO}_2$ -coated titanium electrode prepared by electrophoretic deposition. *Separation and Purification Technology*, 165, 145-153.
- Liu, G., Li, X., Han, B., Chen, L., Zhu, L. & Campos, L. C. (2017). Efficient degradation of sulfamethoxazole by the Fe (II)/ $\text{HSO}_5^-$  process enhanced by hydroxylamine: efficiency and mechanism. *Journal of Hazardous Materials*, 322, 461-468.
- Liu, S., Wang, N., Zhang, Y., Li, Y., Han, Z. & Na, P. (2015). Efficient removal of radioactive iodide ions from water by three-dimensional  $\text{Ag}_2\text{O-Ag}/\text{TiO}_2$  composites under visible light irradiation. *Journal of Hazardous Materials*, 284, 171-181.
- Luo, J., Zhou, X., Ma, L. & Xu, X. (2015). Enhanced visible-light-driven photocatalytic activity of  $\text{WO}_3/\text{BiOI}$  heterojunction photocatalysts. *Journal of Molecular Catalysis A: Chemical*, 410, 168-176.
- Ma, S., Xue, J., Zhou, Y. & Zhang, Z. (2014). Photochemical synthesis of  $\text{ZnO}/\text{Ag}_2\text{O}$  heterostructures with enhanced ultraviolet and visible photocatalytic activity. *Journal of Materials Chemistry A*, 2(20), 7272-7280.
- Malathi, A., Vasanthakumar, V., Arunachalam, P., Madhavan, J. & Ghanem, M. A. (2017). A low cost additive-free facile synthesis of  $\text{BiFeWO}_6/\text{BiVO}_4$  nanocomposite with enhanced visible-light induced photocatalytic activity. *Journal of Colloid and Interface Science*, 506, 553-563.
- Martins, A. S., Nuñez, L. & de Vasconcelos Lanza, M. R. (2017). Enhanced photoelectrocatalytic performance of  $\text{TiO}_2$  nanotube array modified with  $\text{WO}_3$  applied to the degradation of the endocrine disruptor propyl paraben. *Journal of Electroanalytical Chemistry*, 802, 33-39.

- Medel, A., Ramírez, J. A., Cardenas, J., Sires, I. & Meas, Y. (2019). Evaluating the electrochemical and photoelectrochemical production of hydroxyl radical during electrocoagulation process. *Separation and Purification Technology*, 208, 59-67.
- Meng, A., Shao, J., Fan, X., Wang, J. & Li, Z. (2014). Rapid synthesis of a flower-like ZnO/rGO/Ag micro/nano-composite with enhanced photocatalytic performance by a one-step microwave method. *RSC Advances*, 4(104), 60300-60305.
- Mohora, E., Rončević, S., Agbaba, J., Tubić, A., Mitić, M., Klašnja, M. & Dalmacija, B. (2014). Removal of arsenic from groundwater rich in natural organic matter (NOM) by continuous electrocoagulation/flocculation (ECF). *Separation and Purification Technology*, 136, 150-156.
- Monfort, O., Pop, L.-C., Sfaelou, S., Plecenik, T., Roch, T., Dracopoulos, V., . . . Lianos, P. (2016). Photoelectrocatalytic hydrogen production by water splitting using BiVO<sub>4</sub> photoanodes. *Chemical Engineering Journal*, 286, 91-97.
- Monfort, O., Raptis, D., Satrapinskyy, L., Roch, T., Plesch, G. & Lianos, P. (2017). Production of hydrogen by water splitting in a photoelectrochemical cell using a BiVO<sub>4</sub>/TiO<sub>2</sub> layered photoanode. *Electrochimica Acta*, 251, 244-249.
- Monfort, O., Sfaelou, S., Satrapinskyy, L., Plecenik, T., Roch, T., Plesch, G. & Lianos, P. (2017a). Comparative study between pristine and Nb-modified BiVO<sub>4</sub> films employed for photoelectrocatalytic production of H<sub>2</sub> by water splitting and for photocatalytic degradation of organic pollutants under simulated solar light. *Catalysis Today*, 280, 51-57.
- Monfort, O., Sfaelou, S., Satrapinskyy, L., Plecenik, T., Roch, T., Plesch, G. & Lianos, P. (2017b). Comparative study between pristine and Nb-modified BiVO<sub>4</sub> films employed for photoelectrocatalytic production of H<sub>2</sub> by water splitting and for photocatalytic degradation of organic pollutants under simulated solar light. *Catalysis Today*, 280, 51-57.
- Moreira, F. C., Boaventura, R. A., Brillas, E. & Vilar, V. J. (2015). Degradation of trimethoprim antibiotic by UVA photoelectro-Fenton process mediated by Fe (III)-carboxylate complexes. *Applied Catalysis B: Environmental*, 162, 34-44.
- Moreira, F. C., Boaventura, R. A., Brillas, E. & Vilar, V. J. (2017). Electrochemical advanced oxidation processes: a review on their application to synthetic and real wastewaters. *Applied Catalysis B: Environmental*, 202, 217-261.
- Moreira, F. C., Garcia-Segura, S., Vilar, V. J., Boaventura, R. A. & Brillas, E. (2013). Decolorization and mineralization of Sunset Yellow FCF azo dye by anodic oxidation, electro-Fenton, UVA photoelectro-Fenton and solar photoelectro-Fenton processes. *Applied Catalysis B: Environmental*, 142, 877-890.
- Moussa, D. T., El-Naas, M. H., Nasser, M. & Al-Marri, M. J. (2017). A comprehensive review of electrocoagulation for water treatment: Potentials and challenges. *Journal of environmental management*, 186, 24-41.
- Naje, A. S., Chelliapan, S., Zakaria, Z. & Abbas, S. A. (2015). Enhancement of an electrocoagulation process for the treatment of textile wastewater under combined electrical connections using titanium plates. *Int. J. Electrochem. Sci*, 10(6), 4495-4512.
- Ndlovu, T., Arotiba, O. A., Sampath, S., Krause, R. W. & Mamba, B. B. (2011). Electrochemical detection and removal of lead in water using poly(propylene imine) modified re-compressed exfoliated graphite electrodes. *Journal of Applied Electrochemistry*, 41(12), 1389-1396. doi: 10.1007/s10800-011-0360-6
- Ndlovu, T., Mamba, B. B., Sampath, S., Krause, R. W. & Arotiba, O. A. (2014). Voltammetric detection of arsenic on a bismuth modified exfoliated graphite electrode. *Electrochimica Acta*, 128, 48-53. doi: 10.1016/j.electacta.2013.08.084
- Neelavannan, M. & Basha, C. A. (2008). Electrochemical-assisted photocatalytic degradation of textile wastewater. *Separation and Purification Technology*, 61(2), 168-174.
- Neumann-Spallart, M., Shinde, S. S., Mahadik, M. & Bhosale, C. H. (2013). Photoelectrochemical degradation of selected aromatic molecules. *Electrochimica Acta*, 111, 830-836. doi: 10.1016/j.electacta.2013.08.080
- Ntsendwana, B., Mamba, B. B., Sampath, S. & Arotiba, O. A. (2013). Synthesis, characterisation and application of an exfoliated graphite-diamond composite electrode in the electrochemical degradation of trichloroethylene. *RSC Advances*, 3(46), 24473-24483. doi: 10.1039/c3ra44977g
- Ntsendwana, B., Peleyeju, M. G. & Arotiba, O. A. (2016). The application of exfoliated graphite electrode in the electrochemical degradation of p-nitrophenol in water. *Journal of Environmental Science and Health – Part A Toxic/Hazardous Substances and Environmental Engineering*, 51(7), 571-578. doi: 10.1080/10934529.2016.1141623
- Ntsendwana, B., Sampath, S., Mamba, B. & Arotiba, O. (2013). Photoelectrochemical oxidation of p-nitrophenol on an expanded graphite-TiO<sub>2</sub> electrode. *Photochemical & Photobiological Sciences*, 12(6), 1091-1102.
- Ntsendwana, B., Sampath, S., Mamba, B. B., Oluwafemi, O. S. & Arotiba, O. A. (2016). Photoelectrochemical degradation of eosin yellowish dye on exfoliated graphite-ZnO nanocomposite electrode. *Journal of Materials Science: Materials in Electronics*, 27(1), 592-598. doi: 10.1007/s10854-015-3793-6

- Oncel, M., Muhcu, A., Demirbas, E. & Kobya, M. (2013). A comparative study of chemical precipitation and electrocoagulation for treatment of coal acid drainage wastewater. *Journal of Environmental Chemical Engineering*, 1(4), 989-995.
- Orimolade, B. O., Koiki, B. A., Zwane, B. N., Peleyeju, G. M., Mabuba, N. & Arotiba, O. A. (2019). Interrogating solar photoelectrocatalysis on an exfoliated graphite-BiVO<sub>4</sub>/ZnO composite electrode towards water treatment. *RSC Advances*, 9(29), 16586-16595.
- Ozyonar, F. (2016). Treatment of train industry oily wastewater by electrocoagulation with hybrid electrode pairs and different electrode connection modes. *Int. J. Electrochem. Sci*, 11(2), 1456-1471.
- Patel, U. D., Ruparelia, J. & Patel, M. U. (2011). Electrocoagulation treatment of simulated floor-wash containing Reactive Black 5 using iron sacrificial anode. *Journal of Hazardous Materials*, 197, 128-136.
- Peleyeju, M., Umukoro, E., Babalola, J. & Arotiba, O. (2016). Electrochemical Degradation of an Anthraquinonic Dye on an Expanded Graphite-Diamond Composite Electrode. *Electrocatalysis*, 7(2), 132-139.
- Peleyeju, M. G. & Arotiba, O. A. (2018). Recent trend in visible-light photoelectrocatalytic systems for degradation of organic contaminants in water/wastewater. *Environmental Science: Water Research and Technology*, 4(10), 1389-1411. doi: 10.1039/c8ew00276b
- Peleyeju, M. G., Umukoro, E. H., Tshwenya, L., Moutloali, R., Babalola, J. O. & Arotiba, O. A. (2017). Photoelectrocatalytic water treatment systems: degradation, kinetics and intermediate products studies of sulfamethoxazole on a TiO<sub>2</sub>-exfoliated graphite electrode. *RSC Advances*, 7(64), 40571-40580.
- Peleyeju, M. G., Umukoro, E. H., Tshwenya, L., Moutloali, R., Babalola, J. O. & Arotiba, O. A. (2017). Photoelectrocatalytic water treatment systems: Degradation, kinetics and intermediate products studies of sulfamethoxazole on a TiO<sub>2</sub>-exfoliated graphite electrode. *RSC Advances*, 7(64), 40571-40580. doi: 10.1039/c7ra07399b
- Poh, H. L., Šaněk, F., Ambrosi, A., Zhao, G., Sofer, Z. & Pumera, M. (2012). Graphenes prepared by Staudenmaier, Hofmann and Hummers methods with consequent thermal exfoliation exhibit very different electrochemical properties. *Nanoscale*, 4(11), 3515-3522.
- Prajapati, A. K., Chaudhari, P. K., Pal, D., Chandrakar, A. & Choudhary, R. (2016). Electrocoagulation treatment of rice grain based distillery effluent using copper electrode. *Journal of Water Process Engineering*, 11, 1-7.
- Qin, J., Li, R., Lu, C., Jiang, Y., Tang, H. & Yang, X. (2015). Ag/ZnO/graphene oxide heterostructure for the removal of rhodamine B by the synergistic adsorption-degradation effects. *Ceramics International*, 41(3), 4231-4237.
- Qiu, L., Cui, Y., Tan, X., Zheng, S., Zhang, H., Xu, J. & Wang, Q. (2019). Construction of Ag<sub>3</sub>PO<sub>4</sub>/Ag<sub>4</sub>P<sub>2</sub>O<sub>7</sub> nanospheres sensitized hierarchical titanium dioxide nanotube mesh for photoelectrocatalytic degradation of methylene blue. *Separation and Purification Technology*, 215, 619-624.
- Radjenovic, J. & Petrovic, M. (2017). Removal of sulfamethoxazole by electrochemically activated sulfate: implications of chloride addition. *Journal of Hazardous Materials*, 333, 242-249.
- Rubí-Juárez, H., Barrera-Díaz, C., Linares-Hernández, I., Fall, C. & Bilyeu, B. (2015). A combined electrocoagulation-electrooxidation process for carwash wastewater reclamation. *Int. J. Electrochem. Sci*, 10(8), 6754-6767.
- Sakai, Y., Shimanaka, A., Shioi, M., Kato, S., Satokawa, S., Kojima, T. & Yamasaki, A. (2015). Fabrication of high-sensitivity palladium loaded tungsten trioxide photocatalyst by photodeposit method. *Catalysis Today*, 241, 2-7.
- Salazar, R., Garcia-Segura, S., Ureta-Zañartu, M. S. & Brillas, E. (2011). Degradation of disperse azo dyes from waters by solar photoelectro-Fenton. *Electrochimica Acta*, 56(18), 6371-6379. doi: 10.1016/j.electacta.2011.05.021
- Sánchez-Martínez, D., Martínez-De La Cruz, A. & López-Cuellar, E. (2013). Synthesis of WO<sub>3</sub> nanoparticles by citric acid-assisted precipitation and evaluation of their photocatalytic properties. *Materials Research Bulletin*, 48(2), 691-697.
- Sarkar, D., Ghosh, C. K., Mukherjee, S. & Chattopadhyay, K. K. (2012). Three dimensional Ag<sub>2</sub>O/TiO<sub>2</sub> type-II (p-n) nanoheterojunctions for superior photocatalytic activity. *ACS applied materials & interfaces*, 5(2), 331-337.
- Schwarzenbach, R. P., Escher, B. I., Fenner, K., Hofstetter, T. B., Johnson, C. A., Von Gunten, U. & Wehrli, B. (2006). The challenge of micropollutants in aquatic systems. *Science*, 313(5790), 1072-1077.
- Sfaelou, S., Pop, L.-C., Monfort, O., Dracopoulos, V. & Lianos, P. (2016). Mesoporous WO<sub>3</sub> photoanodes for hydrogen production by water splitting and PhotoFuelCell operation. *International Journal of Hydrogen Energy*, 41(14), 5902-5907.
- Shang, M., Wang, W., Sun, S., Ren, J., Zhou, L. & Zhang, L. (2009). Efficient visible light-induced photocatalytic degradation of contaminant by spindle-like PANI/BiVO<sub>4</sub>. *The Journal of Physical Chemistry C*, 113(47), 20228-20233.

- Shannon, M. A., Bohn, P. W., Elimelech, M., Georgiadis, J. G., Mariñas, B. J. & Mayes, A. M. (2008). Science and technology for water purification in the coming decades. *Nature*, 452(7185), 301-310. doi: 10.1038/nature06599
- States, S. S. I. o. t. U., America, S. S. I. o. N., Institute, N. D., Iron, A. & Institute, S. (1993). *Design Guidelines for the Selection and Use of Stainless Steel*: Specialty Steel Industry of the United States.
- Suárez-Escobar, A., Pataquiva-Mateus, A. & López-Vasquez, A. (2016). Electrocoagulation—photocatalytic process for the treatment of lithographic wastewater. Optimization using response surface methodology (RSM) and kinetic study. *Catalysis Today*, 266, 120-125.
- Sun, J., Guo, Y., Wang, Y., Cao, D., Tian, S., Xiao, K., . . . Zhao, X. (2018). H<sub>2</sub>O<sub>2</sub> assisted photoelectrocatalytic degradation of diclofenac sodium at g-C<sub>3</sub>N<sub>4</sub>/BiVO<sub>4</sub> photoanode under visible light irradiation. *Chemical Engineering Journal*, 332, 312-320.
- Sun, Y., Qu, B., Liu, Q., Gao, S., Yan, Z., Yan, W., . . . Xie, Y. (2012). Highly efficient visible-light-driven photocatalytic activities in synthetic ordered monoclinic BiVO<sub>4</sub> quantum tubes-graphene nanocomposites. *Nanoscale*, 4(12), 3761-3767.
- Tang, M., Xu, X., Wu, T., Zhang, S., Li, X. & Li, Y. (2014). Polyacrylamide grafting of modified graphene oxides by in situ free radical polymerization. *Materials Research Bulletin*, 60, 576-583.
- Theerthagiri, J., Senthil, R., Malathi, A., Selvi, A., Madhavan, J. & Ashokkumar, M. (2015). Synthesis and characterization of a CuS-WO<sub>3</sub> composite photocatalyst for enhanced visible light photocatalytic activity. *RSC Advances*, 5(65), 52718-52725.
- Thiam, A., Zhou, M., Brillas, E. & Sirés, I. (2014). Two-step mineralization of Tartrazine solutions: study of parameters and by-products during the coupling of electrocoagulation with electrochemical advanced oxidation processes. *Applied Catalysis B: Environmental*, 150, 116-125.
- Tian, M., Adams, B., Wen, J., Asmussen, R. M. & Chen, A. (2009). Photoelectrochemical oxidation of salicylic acid and salicylaldehyde on titanium dioxide nanotube arrays. *Electrochimica Acta*, 54(14), 3799-3805.
- Tian, Y., He, W., Zhu, X., Yang, W., Ren, N. & Logan, B. E. (2016). Energy efficient electrocoagulation using an air-breathing cathode to remove nutrients from wastewater. *Chemical Engineering Journal*, 292, 308-314.
- Tolod, K., Hernández, S. & Russo, N. (2017). Recent advances in the BiVO<sub>4</sub> photocatalyst for sun-driven water oxidation: top-performing photoanodes and scale-up challenges. *Catalysts*, 7(1), 13.
- Touahria, S., Hazourli, S., Touahria, K., Eulmi, A. & Aitbara, A. (2016). Clarification of Industrial Mining Wastewater Using Electrocoagulation. *Int. J. Electrochem. Sci*, 11, 5710-5723.
- Trostová, S., Stibor, I., Karpíšková, J., Kolská, Z. & Švorčík, V. (2013). Characterization of surface chemical modified carbon nano-particles. *Materials Letters*, 102, 83-86.
- Tshwenya, L. & Arotiba, O. A. (2017). Ethylenediamine functionalized carbon nanoparticles: Synthesis, characterization, and evaluation for cadmium removal from water. *RSC Advances*, 7(54), 34226-34235. doi: 10.1039/c7ra04709f
- Uddin, A. I., Phan, D.-T. & Chung, G.-S. (2015). Low temperature acetylene gas sensor based on Ag nanoparticles-loaded ZnO-reduced graphene oxide hybrid. *Sensors and Actuators B: Chemical*, 207, 362-369.
- Ulu, F., Barişçi, S., Kobya, M. & Sillanpää, M. (2015). An evaluation on different origins of natural organic matters using various anodes by electrocoagulation. *Chemosphere*, 125, 108-114.
- Umukoro, E. H., Kumar, N., Ngila, J. C. & Arotiba, O. A. (2018). Expanded graphite supported pn MoS<sub>2</sub>-SnO<sub>2</sub> heterojunction nanocomposite electrode for enhanced photo-electrocatalytic degradation of a pharmaceutical pollutant. *Journal of Electroanalytical Chemistry*, 827, 193-203. doi: 10.1016/j.jelechem.2018.09.027
- Umukoro, E. H., Madyibi, S. S., Peleyeju, M. G., Tshwenya, L., Viljoen, E. H., Ngila, J. C. & Arotiba, O. A. (2017). Photocatalytic application of Pd-ZnO-exfoliated graphite nanocomposite for the enhanced removal of acid orange 7 dye in water. *Solid State Sciences*, 74, 118-124. doi: 10.1016/j.solidstatesciences.2017.11.001
- Umukoro, E. H., Peleyeju, M. G., Idris, A. O., Ngila, J. C., Mabuba, N., Rhyman, L., . . . Arotiba, O. A. (2018). Photoelectrocatalytic application of palladium decorated zinc oxide-expanded graphite electrode for the removal of 4-nitrophenol: Experimental and computational studies. *RSC Advances*, 8(19), 10255-10266. doi: 10.1039/c8ra00180d
- Umukoro, E. H., Peleyeju, M. G., Ngila, J. C. & Arotiba, O. A. (2016a). Photocatalytic degradation of acid blue 74 in water using Ag-Ag<sup>+</sup>/O-ZnO nanostructures anchored on graphene oxide. *Solid State Sciences*, 51, 66-73. doi: 10.1016/j.solidstatesciences.2015.11.015
- Umukoro, E. H., Peleyeju, M. G., Ngila, J. C. & Arotiba, O. A. (2016b). Photoelectrochemical degradation of orange II dye in wastewater at a silver-zinc oxide/reduced graphene oxide nanocomposite photoanode. *RSC Advances*, 6(58), 52868-52877. doi: 10.1039/c6ra04156f

- Umukoro, E. H., Peleyeju, M. G., Ngila, J. C. & Arotiba, O. A. (2017). Towards wastewater treatment: Photo-assisted electrochemical degradation of 2-nitrophenol and orange II dye at a tungsten trioxide-exfoliated graphite composite electrode. *Chemical Engineering Journal*, 317, 290-301. doi: 10.1016/j.cej.2017.02.084
- Unal, B. O., Dizge, N., Karagunduz, A. & Keskinler, B. (2019). Combined electrocoagulation and electrooxidation process in electro membrane bioreactor to improve membrane filtration effectiveness. *Bioresource Technology Reports*, 100237.
- Vogelpohl, A. & Kim, S. M. (2004). Advanced oxidation processes (AOPS) in wastewater treatment. *Journal of Industrial and Engineering Chemistry*, 10(1), 33-40.
- Wang, M., Che, Y., Niu, C., Dang, M. & Dong, D. (2013). Effective visible light-active boron and europium co-doped BiVO<sub>4</sub> synthesized by sol-gel method for photodegradation of methyl orange. *Journal of Hazardous Materials*, 262, 447-455.
- Wang, P., Huang, B., Zhang, Q., Zhang, X., Qin, X., Dai, Y., . . . Lou, Z. (2010). Highly efficient visible light plasmonic photocatalyst Ag@Ag (Br, I). *Chemistry – A European Journal*, 16(33), 10042-10047.
- Wang, P., Tang, Y., Dong, Z., Chen, Z. & Lim, T.-T. (2013). Ag-AgBr/TiO<sub>2</sub>/RGO nanocomposite for visible-light photocatalytic degradation of penicillin G. *Journal of Materials Chemistry A*, 1(15), 4718-4727.
- Wang, S., Yun, J.-H., Luo, B., Butburee, T., Peerakiatkhajohn, P., Thaweesak, S., . . . Wang, L. (2017). Recent progress on visible light responsive heterojunctions for photocatalytic applications. *Journal of Materials Science & Technology*, 33(1), 1-22.
- Wang, Y., Lin, H., Jin, F., Niu, J., Zhao, J., Bi, Y. & Li, Y. (2016). Electrocoagulation mechanism of perfluorooctanoate (PFOA) on a zinc anode: Influence of cathodes and anions. *Science of The Total Environment*, 557, 542-550.
- Watkins, J. D., Lawrence, R., Taylor, J. E., Bull, S. D., Nelson, G. W., Foord, J. S., . . . Gascon, S. A. (2010). Carbon nanoparticle surface functionalisation: converting negatively charged sulfonate to positively charged sulfonamide. *Physical Chemistry Chemical Physics*, 12(18), 4872-4878.
- Wei, Z., Liang, F., Liu, Y., Luo, W., Wang, J., Yao, W. & Zhu, Y. (2017). Photoelectrocatalytic degradation of phenol-containing wastewater by TiO<sub>2</sub>/gC<sub>3</sub>N<sub>4</sub> hybrid heterostructure thin film. *Applied Catalysis B: Environmental*, 201, 600-606.
- Weng, B., Wu, J., Zhang, N. & Xu, Y.-J. (2014). Observing the role of graphene in boosting the two-electron reduction of oxygen in graphene-WO<sub>3</sub> nanorod photocatalysts. *Langmuir*, 30(19), 5574-5584.
- WWF-SA. (2016). Water: Facts and Futures-Rethinking South Africa's Water Future: WWF-SA Cape Town.
- Xia, L., Bai, J., Li, J., Zeng, Q., Li, L. & Zhou, B. (2017). High-performance BiVO<sub>4</sub> photoanodes cocatalyzed with an ultrathin  $\alpha$ -Fe<sub>2</sub>O<sub>3</sub> layer for photoelectrochemical application. *Applied Catalysis B: Environmental*, 204, 127-133.
- Xia, L., Bai, J., Li, J., Zeng, Q., Li, X. & Zhou, B. (2016). A highly efficient BiVO<sub>4</sub>/WO<sub>3</sub>/W heterojunction photoanode for visible-light responsive dual photoelectrode photocatalytic fuel cell. *Applied Catalysis B: Environmental*, 183, 224-230.
- Yan, J., Chen, Z., Ji, H., Liu, Z., Wang, X., Xu, Y., . . . Xu, H. (2016). Construction of a 2D Graphene-Like MoS<sub>2</sub>/C<sub>3</sub>N<sub>4</sub> Heterojunction with Enhanced Visible-Light Photocatalytic Activity and Photoelectrochemical Activity. *Chemistry – A European Journal*, 22(14), 4764-4773.
- Yang, J.-S. & Wu, J.-J. (2017). Low-potential driven fully-depleted BiVO<sub>4</sub>/ZnO heterojunction nanodendrite array photoanodes for photoelectrochemical water splitting. *Nano Energy*, 32, 232-240.
- Yang, N., Zhai, J., Wang, D., Chen, Y. & Jiang, L. (2010). Two-dimensional graphene bridges enhanced photoinduced charge transport in dye-sensitized solar cells. *ACS nano*, 4(2), 887-894.
- Yao, S., Qu, F., Wang, G. & Wu, X. (2017). Facile hydrothermal synthesis of WO<sub>3</sub> nanorods for photocatalysts and supercapacitors. *Journal of Alloys and Compounds*, 724, 695-702.
- Yu, X., Zhang, Y. & Cheng, X. (2014). Preparation and photoelectrochemical performance of expanded graphite/TiO<sub>2</sub> composite. *Electrochimica Acta*, 137, 668-675.
- Yuan, Y.-J., Wang, F., Hu, B., Lu, H.-W., Yu, Z.-T. & Zou, Z.-G. (2015). Significant enhancement in photocatalytic hydrogen evolution from water using a MoS<sub>2</sub> nanosheet-coated ZnO heterostructure photocatalyst. *Dalton Transactions*, 44(24), 10997-11003.
- Zhang, J., Li, M., Feng, Z., Chen, J. & Li, C. (2006). UV Raman spectroscopic study on TiO<sub>2</sub>. I. Phase transformation at the surface and in the bulk. *The Journal of Physical Chemistry B*, 110(2), 927-935.
- Zhang, J., Ma, Y., Du, Y., Jiang, H., Zhou, D. & Dong, S. (2017). Carbon nanodots/WO<sub>3</sub> nanorods Z-scheme composites: Remarkably enhanced photocatalytic performance under broad spectrum. *Applied Catalysis B: Environmental*, 209, 253-264.
- Zhang, J., Yang, H., Shen, G., Cheng, P., Zhang, J. & Guo, S. (2010). Reduction of graphene oxide via L-ascorbic acid. *Chemical Communications*, 46(7), 1112-1114.
- Zhang, L., Du, L., Yu, X., Tan, S., Cai, X., Yang, P., . . . Mai, W. (2014). Significantly enhanced photocatalytic activities and charge separation mechanism of Pd-decorated ZnO-graphene oxide nanocomposites. *ACS applied materials & interfaces*, 6(5), 3623-3629.

- Zhang, L. & Jaroniec, M. (2018). Toward designing semiconductor-semiconductor heterojunctions for photocatalytic applications. *Applied Surface Science*, 430, 2-17.
- Zhang, T., Su, J. & Guo, L. (2016). Morphology engineering of WO<sub>3</sub>/BiVO<sub>4</sub> heterojunctions for efficient photocatalytic water oxidation. *CrystEngComm*, 18(46), 8961-8970.
- Zhang, X., Yang, Y., Ding, S., Que, W., Zheng, Z. & Du, Y. (2017). Construction of High-Quality SnO<sub>2</sub>@ MoS<sub>2</sub> Nanohybrids for Promising Photoelectrocatalytic Applications. *Inorganic Chemistry*, 56(6), 3386-3393.
- Zhao, Q., Cheng, X., Wu, J. & Yu, X. (2014). Sulfur-free exfoliated graphite with large exfoliated volume: Preparation, characterization and its adsorption performance. *Journal of Industrial and Engineering Chemistry*, 20(6), 4028-4032.
- Zhao, W., Liu, Y., Wei, Z., Yang, S., He, H. & Sun, C. (2016). Fabrication of a novel p-n heterojunction photocatalyst n-BiVO<sub>4</sub>@ p-MoS<sub>2</sub> with core-shell structure and its excellent visible-light photocatalytic reduction and oxidation activities. *Applied Catalysis B: Environmental*, 185, 242-252.
- Zhi, J.-F., Wang, H.-B., Nakashima, T., Rao, T. N. & Fujishima, A. (2003). Electrochemical incineration of organic pollutants on boron-doped diamond electrode. Evidence for direct electrochemical oxidation pathway. *The Journal of Physical Chemistry B*, 107(48), 13389-13395.
- Zhou, J., Zhao, F., Wang, Y., Zhang, Y. & Yang, L. (2007). Size-controlled synthesis of ZnO nanoparticles and their photoluminescence properties. *Journal of luminescence*, 122, 195-197.
- Zhou, M., Dai, Q., Lei, L., Ma, C. a. & Wang, D. (2005). Long life modified lead dioxide anode for organic wastewater treatment: electrochemical characteristics and degradation mechanism. *Environmental science & technology*, 39(1), 363-370.
- Zhou, Y., Zhang, L., Lin, L., Wygant, B. R., Liu, Y., Zhu, Y., . . . Zhang, X. (2017). Highly efficient photoelectrochemical water splitting from hierarchical WO<sub>3</sub>/BiVO<sub>4</sub> nanoporous sphere arrays. *Nano Letters*, 17(12), 8012-8017.
- Zhu, A., Zhao, Q., Li, X. & Shi, Y. (2013). BiFeO<sub>3</sub>/TiO<sub>2</sub> nanotube arrays composite electrode: construction, characterization, and enhanced photoelectrochemical properties. *ACS applied materials & interfaces*, 6(1), 671-679.
- Zhu, W., Sun, F., Goei, R. & Zhou, Y. (2017). Facile fabrication of RGO-WO<sub>3</sub> composites for effective visible light photocatalytic degradation of sulfamethoxazole. *Applied Catalysis B: Environmental*, 207, 93-102.